JOURNAL OF THE AERONAUTICAL SCIENCES

VOLUME 13 NOVEMBER, 1946 NUMBER 11

Aircraft Ejector Performance

FRANK A. McCLINTOCK* AND J. HALL HOOD†

United Aircraft Corporation and Consolidated Vultee Aircraft Corporation

SUMMARY

This paper presents the results of work on the ejector problem carried out by the Research Department, United Aircraft Corporation, over the past few years. Equations are developed which, with the aid of empirical coefficients, enable one to estimate the performance of steady flow ejectors pumping a fluid across a small pressure rise or drop. Experimental data are presented which support the theory and provide information on some variables not covered by the theoretical treatment. An analogy between steady and intermittent flow is presented which makes it possible to estimate the performance of ejectors used in cooling aircraft engines. A method of applying the results to the design of ejectors is suggested.

The principal uses for an ejector in aircraft engine installations appear to be in those cases in which cooling would otherwise have to be obtained by the use of a fan or stalled cowl flaps, or in which the exhaust thrust could not otherwise be used because of flame, noise, or temperature. The results indicate that little gain in thrust can be obtained in an installation in which there is a pressure drop through the ejector so that pumping is not necessary.

INTRODUCTION

AN EJECTOR IS A DEVICE in which the kinetic energy of one fluid is used to pump a second fluid. It consists essentially of a duct through which is discharged a high velocity jet. The secondary fluid is drawn from a region of low pressure, mixes with the high velocity jet in the duct, and is discharged to a region of higher pressure. The ejector may, of course, be operated with no pressure rise or a pressure drop through it. In this case, the ejector may still increase the net thrust of the installation but it will not act as a jet pump.

For airplane installations in which the propeller or flight-induced cooling is inadequate (such as in helicopters or airplanes climbing at slow speeds), some form of pump must be used to maintain the required cooling airflow through the engine. Cowl flaps may be employed as a pumping device. In this case, however, the pressure rise is maintained by stalling the cowl flaps, which results in an increase in form drag. The two alternatives at present are fans and ejectors. Although an ejector is a far less efficient pump than a fan, it need not take power from the engine and it has the advantage that the propulsive efficiency of the exhaust jet may actually be improved by mixing it with the large mass of slow-moving cooling air.

Presented at the National Aircraft Propulsion Meeting, I.A.S., Cleveland, March 21, 1946.

* Assistant Project Engineer, Pratt & Whitney Aircraft Division.

† Research Engineer.

THEORETICAL TREATMENT

The object of this analysis is to develop equations for the pressure rise of the secondary stream and for the momentum from the ejector system in terms of the quantity and state of the primary and secondary streams and the dimensions of the ejector. The effects of mixing and velocity distribution are accounted for by empirical coefficients. Incompressible flow is assumed in order to reduce the number of variables required in presenting an overall picture of ejector performance and to give equations that can be solved explicitly for given dimensions. The effects of compressible flow are discussed qualitatively in a later section.

This analysis differs from that of Flugel[1] and Gosline and O'Brien[2] in that the increase in exhaust momentum is calculated and the effect on performance of nonuniform velocity distribution at a section is considered.

When the velocity distribution at any given section of a fluid stream is not uniform, the mean velocities for the continuity equation, the momentum equation, and the energy equation are all different, because one is an arithmetic mean, the second a root mean square, and the third a root mean cube velocity. The empirical coefficients C_M and C_H are used to relate the mean velocities for momentum and velocity head to that for flow,

V. Thus, the equations for flow, momentum, and velocity head at a given section are:

$$\text{Flow} = W = \rho g A V \quad (1)$$

$$\text{Momentum} = F = W(VC_M)/g \quad (2)$$

$$\text{Velocity head} = \rho(VC_H)^2/2 \quad (3)$$

where

W = weight flow
ρ = mass density
g = gravitational constant
V = velocity
A = cross-sectional area
F = momentum at a section

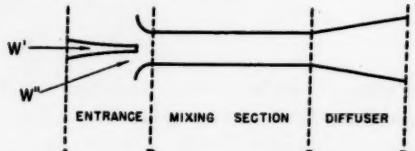

FIG. 1. Schematic diagram of ejector.

Fig. 1 is a schematic diagram of an ejector, indicating the sections considered in this analysis. The following notation is used:

NOTATION

Superscripts:

$'$ refers to primary jet
$''$ refers to secondary fluid
Terms without superscripts refer to both streams or the mixed stream

Subscripts:

A refers to conditions at zero velocity before the ejector
B refers to conditions before mixing in the throat of the ejector
C refers to conditions at end of mixing section
D refers to conditions at exit of diffuser

The pressure changes in the entrance section and the diffuser sections are found from Bernoulli's equation and the definition of efficiency:

$$P_A'' - P_B = \frac{\rho''(V_B''C_{HB}'')^2}{2\eta_{AB}''} \quad (4)$$

$$P_D - P_C = \eta_{CD}\left[\frac{\rho(V_CC_{HC})^2}{2} - \frac{\rho(V_DC_{HD})^2}{2}\right] \quad (5)$$

where

P = pressure

η_{AB}'' = ideal pressure drop / actual pressure drop of secondary air in entrance section for a given change in velocity

η_{CD} = actual pressure rise / ideal pressure rise in the diffuser for a given change in velocity

The pressure rise in the mixing section is found from the momentum equation and the pressure drop due to friction. The friction pressure drop is based arbitrarily on the secondary velocity at section B.

$$P_C - P_B = \frac{1}{A_C}\left(\frac{W'V_B'C_{MB}'}{g} + \frac{W''V_B''C_{MB}''}{g} - \frac{WV_CC_{MC}}{g}\right) - \frac{f\rho''(V_B''C_{HB}'')^2}{2}\frac{L}{D} \quad (6)$$

where the friction factor, f, is defined by the equation

$$\text{Friction pressure drop} = (f\rho V^2/2)(L/D)$$

L = length of mixing section wall
D = diameter of mixing section

In order to reduce the number of variables, the following dimensionless ratios are introduced:

$$\alpha = \frac{\text{Area of diffuser exit}}{\text{Area of mixing section}}$$

$$\lambda = \frac{\text{Area of mixing section}}{\text{Effective area of primary jet}}$$

$$\mu = \frac{\text{Secondary flow}}{\text{Primary flow}}$$

$$\sigma = \frac{\text{Secondary density}}{\text{Primary density}}$$

For incompressible fluids or for the same gas at different temperatures in the primary and secondary streams, the density of the mixed stream is found from the following relation:

$$\rho = \frac{W' + W''}{(W'/\rho') + (W''/\rho'')}; \quad \frac{\rho}{\rho'} = \frac{1+\mu}{1+(\mu/\sigma)} \quad (7)$$

Introducing the dimensionless ratios, and combining Eqs. (1), (4), (5), (6), and (7), the following relationships for the pressure rise from the various sections to the discharge pressure are obtained:

$$\frac{P_D - P_C}{F'/A'} = \frac{\eta_{CD}C_{HC}^2(1+\mu)[1+(\mu/\sigma)]}{2\lambda^2}\left[1 - \left(\frac{C_{HD}}{\alpha C_{HC}}\right)^2\right] \quad (8)$$

From the ejector throat:

$$\frac{P_D - P_B}{F'/A'} = \frac{C_{MB}'}{\lambda} + \frac{\mu^2 C_{MB}''}{\sigma\lambda(\lambda-1)} - \frac{\mu^2(C_{HB}'')^2}{2\sigma(\lambda-1)^2}f\frac{L}{D} - \frac{(1+\mu)(1+\mu/\sigma)}{\lambda^2}\left\{C_{MC} - \frac{C_{HC}^2\eta_{CD}}{2}\left[1 - \left(\frac{C_{HD}}{\alpha C_{HC}}\right)^2\right]\right\} \quad (9)$$

From the initial secondary pressure:

$$\frac{P_D - P_A''}{F'/A'} = \frac{C_{MB}'}{\lambda} + \frac{\mu^2 C_{MB}''}{\sigma\lambda(\lambda-1)} - \frac{\mu^2(C_{HB}'')^2}{2\sigma(\lambda-1)^2} \times \left(\frac{1}{\eta_{AB}''} + f\frac{L}{D}\right) - \frac{(1+\mu)(1+\mu/\sigma)}{\lambda^2} \times \left\{C_{MC} - \frac{C_{HC}^2\eta_{CD}}{2}\left[1 - \left(\frac{C_{HD}}{\alpha C_{HC}}\right)^2\right]\right\} \quad (10)$$

The momentum of the combined stream at the ejector exit is found from Eq. (2),

$$F = WV_D C_{MD}/g \tag{11}$$

The ratio of this momentum to the momentum of the primary jet is found from Eqs. 1, 2, 7, and 11:

$$F/F' = \frac{(1+\mu)(1+\mu/\sigma)C_{MD}}{\alpha\lambda C_{MB}'} \tag{12}$$

Not all of the coefficients in Eqs. (10) and (12) are worth considering; in fact, a fair correlation between test results and theory can be found by assuming the coefficients η_{AB}'', C_{MB}', C_{MB}'', C_{HB}', and C_{HB}'' equal to unity, neglecting the skin friction, and considering C_{MD} and the group $C_{MC} - \frac{C_{HC}^2\eta_{CD}}{2}\left[1 - \left(\frac{C_{HD}}{\alpha C_{HC}}\right)^2\right]$ (hereafter called K) to be functions of the diffuser area ratio only. Eqs. (10) and (12) then become

$$\frac{P_D - P_A''}{F'/A'} = \frac{1}{\lambda} + \frac{\mu^2}{\sigma\lambda(\lambda-1)} - \frac{(1+\mu)(1+\mu/\sigma)K}{\lambda^2} - \frac{\mu^2}{2\sigma(\lambda-1)^2} \tag{13}$$

$$F/F' = \frac{(1+\mu)(1+\mu/\sigma)C_{MD}}{\alpha\lambda} \tag{14}$$

The experimental flow and thrust coefficients (K) and (C_{MD}) have been calculated from data on compressed air tests of single nozzle ejectors having a cylindrical mixing section five diameters in length and having 8° (included angle) conical diffusers. Fig. 2 gives the average values of these coefficients as a function of the diffuser area ratio, α. Fig. 3 shows a comparison of the theoretical curves based on the coefficients given in Fig. 2, and cross-plots of the actual experimental data. These curves give the pressure rise ratio for the secondary stream and the thrust ratio as a function of the mixing section area ratio, λ, for a constant flow ratio, μ, of 2. Substantially the same degree of correlation was found for other flow ratios. This appears to justify the direct use of the theoretical equations in predicting the performance of this type of ejector. While better values of the empirical thrust and flow coefficients, C_{MD} and K, were observed in some tests, these are probably as good as could be expected in an actual installation, so that their use for preliminary estimates seems justified.

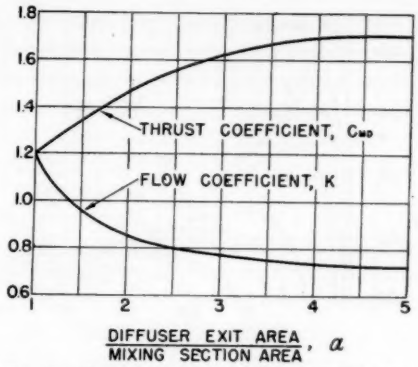

FIG. 2. Empirical thrust and flow coefficients.

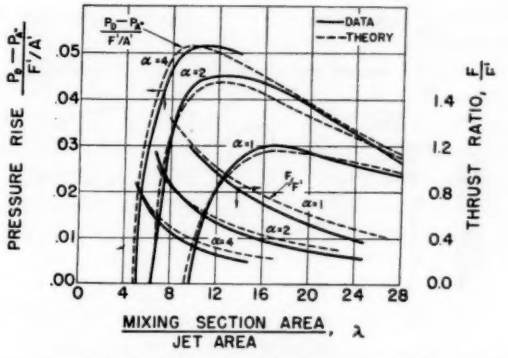

FIG. 3. Comparison of data with theory. Flow ratio, $\mu = 2$; density ratio, $\sigma = 0.92$; α = diffuser area ratio.

EFFECT OF PRIMARY VARIABLES ON EJECTOR PERFORMANCE

For a given primary jet, ejectors can be designed which pump either a little air across a high pressure rise or more air across a small pressure rise with an increase in momentum. The effect of varying the primary jet in a given ejector is more difficult to visualize, because a change in the primary jet affects several of the dimensionless groups of Eqs. (13) and (14) simultaneously. Nor can the effect of changes in the density ratio be seen at a glance; its effect on the flow or thrust must be found by solving the equations for the particular case at hand.

For the purpose of illustrating the design parameters and showing the characteristic performance of steady flow ejectors, a series of curves has been calculated based on the experimental coefficients given in Fig. 2 for a density ratio of 3.5, this being representative of an ejector using steady flow engine exhaust gas as the actuating jet. Since the flow and the pressure rise are usually specified in ejector design, plots of pressure rise vs. mixing-section area ratio are presented for flow ratios of 2, 6, and 10 as shown in Fig. 4. For a typical engine, a pressure rise of 10 in. of water corresponds to a pressure rise parameter of 0.03. As would be expected, the curves show that in order to get more pressure rise for the same flow and mixing section area, more diffuser must be used. The effectiveness of adding a diffuser falls off as more and more is used. It should also be noted from these curves that for any given flow ratio and diffuser area ratio, there is a mixing section area that gives the greatest possible rise. If the maximum pressure rise is not required, then a range of mixing sections can be used. The use of a

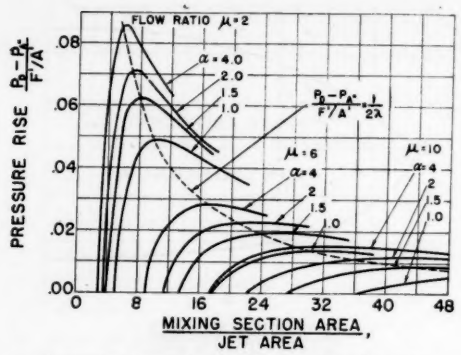

FIG. 4. Theoretical pumping capacity. Density ratio, $\sigma = 3.5$; α = diffuser area ratio.

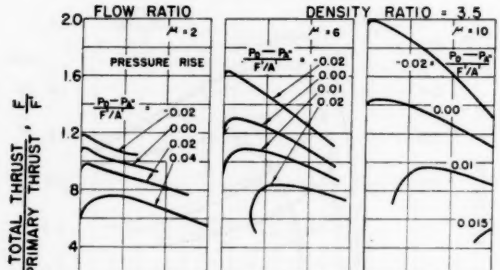

FIG. 5. Theoretical thrust ratio.

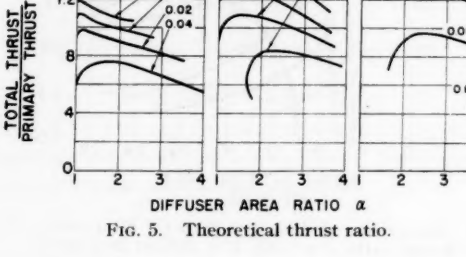

FIG. 6. Theoretical maximum thrust ratio. Flow ratio, $\mu = 6$; density ratio, $\sigma = 3.5$.

smaller mixing section would give more thrust and result in a smaller ejector, but, on the other hand, the mixing section area ratio is less critical if the larger mixing section is used, so that it is easier to meet the design point in that region.

The points of maximum pressure rise for a given flow and diffuser area ratio can be found analytically by differentiating the flow equation, Eq. (13), with respect to the mixing section area ratio, λ, equating to zero, and eliminating the flow coefficient, K, by Eq. (13). The result is:

$$\frac{P_D - P_A''}{F'/A'} = \frac{1}{2\lambda} + \frac{\mu^2}{2\sigma\lambda(\lambda - 1)^3} \tag{15}$$

The second term is negligible. The simplified equation determines the locus of the points of maximum pressure rise for a given flow and diffuser area ratio, or the points of minimum diffuser area for a given flow and pressure rise, as shown in Fig. 4. The use of this equation will be described in the design section.

For most aircraft installations the momentum of the ejector stream is of interest. Reference to Eq. (14) shows that the smaller the diffuser and mixing section area ratios, the greater the momentum for a given flow. But since these area ratios must be adjusted to maintain the required pressure rise, there is an optimum diffuser area ratio for a given flow and pressure rise. Fig. 5 shows the ratio of total to primary thrust vs. diffuser area ratio at different pressure rises and flow ratios of 2, 6, and 10, respectively. It will be noted from these curves that for a given flow ratio the diffuser area ratio for maximum thrust is greater at the higher pressure rises. The thrust ratio is greatest with high flows and a pressure drop across the ejector. Fig. 6 is a cross-plot of the maximum thrust points for a flow ratio of 6, showing the increase in thrust as the pressure rise decreases and finally becomes a pressure drop. The usefulness of an ejector as a thrust-augmenting device can only be judged by comparing it with other systems. The dotted lines on the right-hand side of Fig. 6 show the drag that might be associated with pumping the cooling air out by means of cowl flaps or the loss in propeller thrust that would result from using a cooling fan. The exhaust thrust less this drag is the net thrust of the alternate system and is less than the total thrust of the ejector, shown by the solid line, so that in this region the ejector will give better performance than other systems. When there is a pressure drop through the ejector, however, the net thrust of the alternate system is that of the exhaust thrust plus the momentum that the cooling air would have if discharged separately. This momentum, neglecting losses, would be:

$$F'' = W'' V_D''/g \tag{16}$$

The velocity may be found from the available pressure drop of the secondary stream; hence, the momentum is:

$$F'' = (W''/g)\sqrt{2(P_A'' - P_D)/\rho''} \tag{17}$$

Expressed in terms of the properties of the primary jet, this momentum is:

$$\frac{F''}{F'} = \mu\sqrt{\frac{2}{\sigma}}\sqrt{\frac{(P_A'' - P_D)}{F'/A'}} \tag{18}$$

Fig. 6 shows that with an increasing pressure drop through the ejector, the sum of the exhaust thrust and this secondary momentum soon equals the ejector thrust.

For a typical engine exhaust and a flow ratio of 6, the ejector yields no gain in thrust when the pressure drop through the ejector is greater than about 5 in. of water. This characteristic of ejectors limits their usefulness as thrust augmenters to a small range. They are nonetheless useful in reducing the drag associated with pumping the cooling air, if that is necessary.

Effect of Compressibility

The experimental coefficients in the steady flow theory were derived from compressed air tests in which the primary jet velocity was approximately 700 or 800 ft. per sec. Steady flow tests with superheated steam as the primary fluid were, however, run with primary velocities from 1,200 to 2,800 ft. per sec. The latter tests showed that the design of an ejector is not affected by the primary jet velocity. For supersonic velocities of the primary jet the performance of the ejector was not appreciably affected by removing the divergent section of the nozzle. In designing an ejector, however, the area of the fully expanded stream, rather than the area of the nozzle, must be used. The temperature of the primary jet should also be calculated assuming complete expansion of the jet to the pressure in the ejector throat.

The high-velocity steam tests showed that the performance of an ejector fell off sharply when the flow mean velocity of the mixed streams reached a Mach Number around 0.6. After this velocity was reached, practically no increase in secondary airflow or total ejector thrust could be obtained by further increasing the primary flow and primary velocity. It is, therefore, necessary to check the velocity in the mixing section when designing an ejector for a given condition. If the calculated velocity yields a greater Mach Number than 0.6, the ejector should be redesigned with a larger mixing section area. The theoretical curves presented in this report were based on experimental data in which the Mach Number of the mixed streams was not over 0.3.

The effect of compressibility was also checked analytically by assuming a primary jet Mach Number of unity, zero pressure rise, and a mixing section area ratio of 20. The thrust for a given flow ratio was about 2 per cent less for compressible flow, and the flow ratio for a given diffuser area ratio was about 5 per cent greater for compressible flow. The agreement was even better for ejectors without diffusers, so that the assumption of incompressible flow seems reasonable.

Effect of Altitude

Data obtained from sea-level tests of ejectors cannot be applied in designing an ejector to cool an engine at altitude without considering the effect of the change in densities. A decrease in the density ratio by itself results in a loss in ejector performance. For a given primary flow, however, the jet thrust increases with altitude because of the reduced back pressure on the nozzle. The increase in jet thrust has a greater effect upon the performance than has the change in density ratio. Therefore, if the velocity of the steady flow primary jet is subsonic, the overall performance will improve with an increase in altitude.

If this jet velocity is sonic at any given altitude, a further increase in altitude may be accompanied by a decrease in performance in spite of the increased jet thrust. The reason for this is that the jet expands to a greater area after leaving the nozzle, giving in effect a smaller mixing section area ratio.

The quantitative effect of altitude on the performance of an ejector will depend upon the design conditions and the particular ejector chosen for these conditions. Fig. 7 shows the calculated effect of altitude on the performance of a steady flow ejector designed for an arbitrary set of conditions. The variation in flow and thrust ratio with altitude is calculated for a constant actual pressure rise. The flow and thrust ratio in this case increase with altitude until the jet velocity becomes sonic. The thrust remains constant and the flow decreases with further increase in altitude.

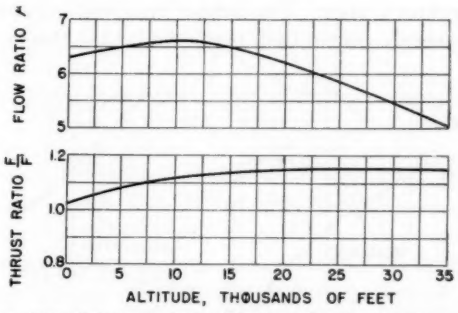

Fig. 7. Calculated effect of altitude. Constant pressure rise.

Divergent Mixing Sections

The ejector with a straight mixing section is not only the easiest to calculate but it also appears to be theoretically the best in the absence of losses. No cases have been observed, either in theory or in experiment, in which a divergent or convergent mixing section led to more thrust or a smaller ejector than a straight mixing section. One exception might be in the case of high Mach Numbers of the secondary stream. In any case, once mixing is complete, the addition of a diffuser section has advantages that have already been discussed.

Intermittent Flow Ejectors

If the exhaust from all cylinders of an engine were collected in a manifold and then discharged through a nozzle, the flow would be steady enough to use the steady flow theory. However, this system would not utilize the impulses of kinetic energy from each cylinder,

so that other arrangements are generally used which involve intermittent flow, and ejectors must be designed to operate with intermittent flow jets.

An analogy can be made between steady flow and intermittent flow by assuming the flow is steady in the latter case and using the primary area that would give the same average primary flow and momentum as the engine exhaust. The effective primary area can then be found from the continuity equation:

$$A' = W'/\rho' g V' \tag{19}$$

and the mean velocity calculated from the primary thrust, which is measured by a balance or a thrust target:

$$F' = W'V'/g \tag{20}$$

Combining these,

$$A' = (W')^2/\rho' g^2 F' \tag{21}$$

The principal objection to making this analogy is that it disregards the effect of the geometrical relationship between the area of the ejector and the primary nozzle. During the period of the cycle when the primary nozzle is actually exhausting the area ratio is smaller than that assumed in using the calculated steady flow primary area. The actual pumping capacity is consequently poorer than predicted by the theory.

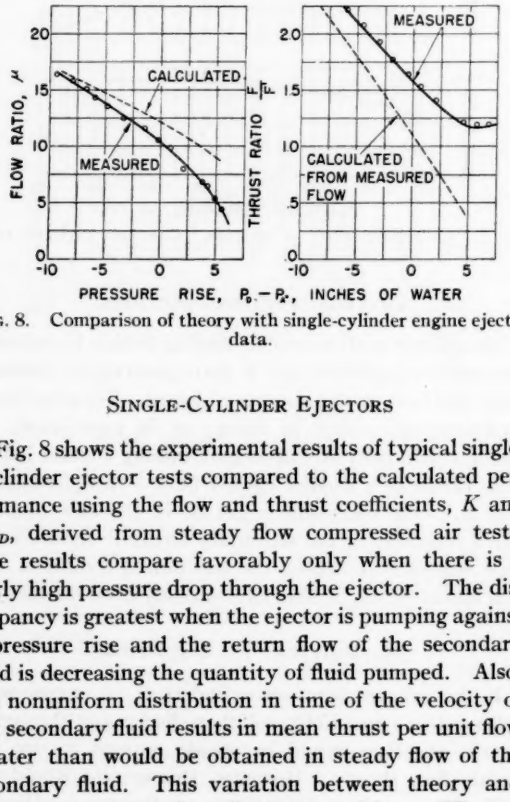

FIG. 8. Comparison of theory with single-cylinder engine ejector data.

SINGLE-CYLINDER EJECTORS

Fig. 8 shows the experimental results of typical single-cyclinder ejector tests compared to the calculated performance using the flow and thrust coefficients, K and C_{MD}, derived from steady flow compressed air tests. The results compare favorably only when there is a fairly high pressure drop through the ejector. The discrepancy is greatest when the ejector is pumping against a pressure rise and the return flow of the secondary fluid is decreasing the quantity of fluid pumped. Also, the nonuniform distribution in time of the velocity of the secondary fluid results in mean thrust per unit flow greater than would be obtained in steady flow of the secondary fluid. This variation between theory and test was consistent for all ejectors without diffusers.

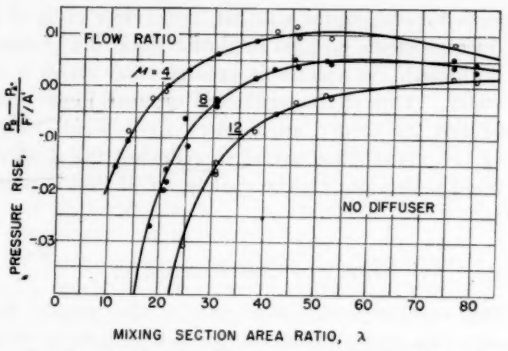

FIG. 9. Correlation of flow data—single-cylinder ejector.

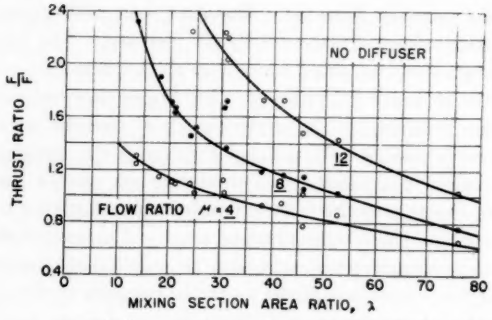

FIG. 10. Correlation of thrust data—single-cylinder ejector.

The variation was more erratic for ejectors with diffusers, but the difference between theory and test in no case appears to be greater for ejectors with diffusers than for ejectors without diffusers. It is evident that the empirical coefficients determined for steady flow ejectors cannot be used to predict the performance of intermittent flow ejectors, so that other means for handling the data must be found.

Figs. 9 and 10 show a correlation of data obtained from tests of ejectors without diffusers actuated by a single cylinder. These plots seem to correlate fairly well data taken over a wide range of engine powers, speeds, fuel-air ratios, and exhaust stack restriction. Fig. 9 gives the pressure rise parameter as a function of the calculated area ratio for various flow ratios. The density ratio is not constant for these tests (varying from 3.5 to 4.5), which accounts for some of the scatter in the data.

Fig. 10 is a plot of the ratio of the total to primary momentum vs. the effective area ratio for various values of the flow ratio. The scatter due to variation in density ratio may be as much as 7 per cent for these data, but there are some isolated points that fall as much as 20 per cent off the average curve. These variations are presumably due to changes in the time distribution of the secondary velocity, which was not accounted for in any way by the analogy.

These plots should not be used in designing ejectors in which "Siamesed stacks" are employed. An ejec-

tor actuated by the exhaust from a number of cylinders having nonoverlapping exhaust periods will pump a considerably greater flow for a given mixing section area ratio than indicated in Fig. 9. The ejector thrust in this case cannot be compared with that given in Fig. 10 because the mixing area required to maintain a given flow is not the same as that for a single-cylinder ejector.

There are insufficient data to plot curves similar to those in Figs. 9 and 10 for ejectors with diffusers. Moreover, these curves do not show the effect of changes in density ratio and cannot, therefore, be used in estimating performance at altitude.

Even if the theory were developed to completely account for all the variables in intermittent flow, it would be of little value at present since the additional data which would be required are not available. It is, therefore, absolutely necessary at present to employ an analogy such as given above in spite of its shortcomings.

Ejectors with Siamesed Stacks

In most engine installations it will be found advantageous to discharge the exhaust from several cylinders into one ejector. The greatest thrust is obtained by having a separate stack for each cylinder, but the piping can be reduced at a small loss in thrust by Siamesing into a single outlet two or three stacks from cylinders whose exhaust periods do not overlap. The outlet area should be the same as that for one individual stack. In this case the primary flow will be more continuous and should approximate more closely that calculated from steady flow theory. However, there are available no experimental data from engine ejectors with Siamesed stacks which are complete enough to check the theory.

Figs. 11 and 12 show a comparison of the theory with results of intermittent flow compressed air tests. Three intermittent flow nozzles were used. The nozzles discharged for one-third of the cycle with a velocity variation representative of that in the exhaust flow from an engine cyclinder. In the first case, three separate ejectors were used so that intermittent flow was obtained through each. The pumping performance of these ejectors was markedly lower and the thrust higher than that given by theory. This is in agreement with the comparison made between the theory and the results of single-cylinder engine tests. In the second case, the nozzles were Siamesed into a single nozzle and used in a single ejector having an area equal to the combined area of the three intermittent flow ejectors. The performance in this case was in good agreement with the theoretical calculated performance. The use of three individual stacks instead of the Siamesed stacks in a single ejector gave the same performance in the compressed air tests, but slightly better performance when tried on a six-cylinder Franklin engine.

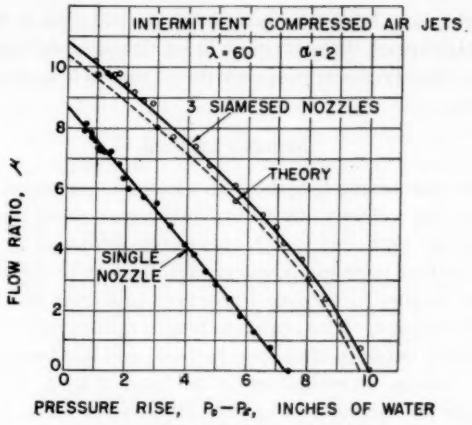

Fig. 11. Effect of Siamesed stacks.

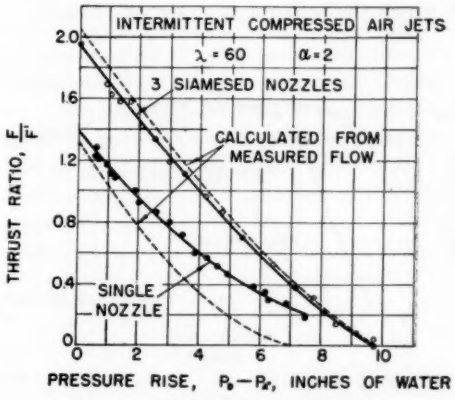

Fig. 12. Effect of Siamesed stacks.

These intermittent flow compressed air tests provide a good enough qualitative check to warrant the use of the theory when Siamesed stacks or a number of individual stacks from nonoverlapping cylinders are used in an ejector so that reasonably continuous flow is maintained. Even if this condition is fulfilled, the results calculated using the empirical thrust and flow coefficients given in Fig. 2 should be considered somewhat optimistic with respect to the flow and conservative with respect to the thrust. Coefficients based on engine tests of the type of ejector being designed should be used whenever the data become available.

Restricted Exhausts

The exhaust momentum in any type of system can be increased by restricting the exit area of the exhaust pipe. The amount of restriction that can be made without a decrease in engine power depends on the type of exhaust system and the exhaust port design of the engine. When individual stacks are used, a loss in engine power will result if the stack area is made less than the area of the exhaust valve passage at the maximum opening of the valve. A restriction in the exhaust

stacks may, however, result in an overall gain in thrust at high speed, if the increase in jet thrust more than offsets the decrease in propeller thrust due to loss of engine power.

Mixing Length

As the mixing length of an ejector is increased from zero, the velocity distribution becomes more uniform and the performance of an ejector improves at first. On further increase, however, wall friction in the mixing duct begins to become important and cuts down the performance. The optimum length results from a compromise between these two factors, and has been found by various investigators to be from 4 to 8 L/D for single-jet ejectors. Fig. 13, from tests on a seven-nozzle ejector, shows the interaction of these two factors and indicates that there is a critical mixing length below which the performance falls off abruptly.

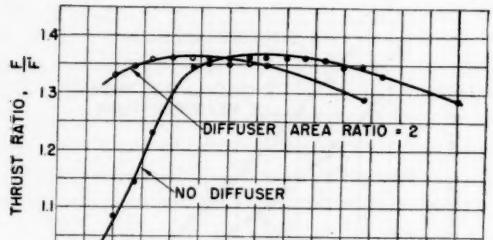

Fig. 13. Effect of mixing length. Seven nozzles. No pressure rise.

For ejectors with several jets, the critical mixing length can be approximated by assuming that the region of mixed stream forms a cone of fixed angle whose apex is at the primary jet. This leads to the rule that the critical mixing section length will vary directly with the mean radial spread of the mixed region to the wall or to another jet, provided that the nozzles are distributed uniformly over the mixing section area. Fig. 14 shows results of compressed air tests which support this rule for various shapes of mixing sections as well as various numbers of nozzles. The diameters of non-circular shapes are taken to be the diameters of circles with equal area. The mean radial spread of the mixed region for multiple-nozzle ejectors is assumed to be the same as that for a circular single-nozzle ejector whose area is equal to that of the whole ejector divided by the number of nozzles. Preliminary tests showed that annular nozzles will also shorten the mixing section if secondary air is allowed to flow through the annulus. All these data were obtained with zero pressure rise across the ejector. It should be emphasized, however, that no advantage will be obtained from distributing the nozzles in the ejector area unless there is essentially a continuous flow from each nozzle. The pressure rise also affects the optimum mixing length. Fig. 15 shows

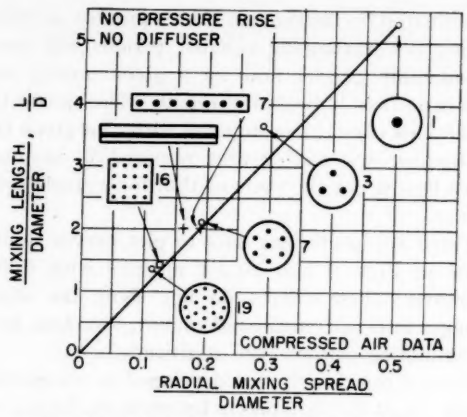

Fig. 14. Critical length of mixing section.

that for the same primary jet, the pressure rise in the mixing section takes place in a much shorter distance when less rise is required, as indicated by the leveling of the curves. Fig. 13 shows that the critical mixing length actually is less with a diffuser, for which less pressure rise occurs in the mixing section even with the same pressure change across the entire ejector.

The performance of an ejector without a diffuser is not appreciably affected by breaking up the primary jet into several scattered jets, provided that the mixing section is above the critical length. The improvement in performance due to the smaller friction loss of the shorter mixing section used is relatively small. However, the improved velocity distribution that results does increase the efficiency of the diffuser, thereby considerably improving the performance of ejectors with diffusers. Fig. 16 shows the comparison between single- and multiple-nozzle ejectors with diffusers of varying area ratio.

Entrance Configuration

Tests have indicated that the entrance radius of the mixing section can be as low as one-sixth of the diameter without affecting the performance. The nozzle should be flush with the entrance or slightly outside the entrance. With steady flow nozzles no appreciable loss

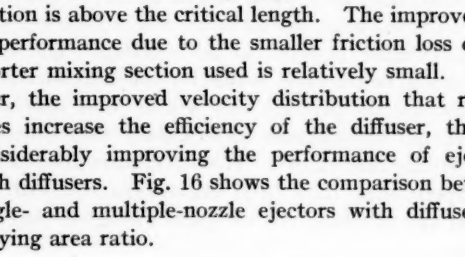

Fig. 15. Static pressure distribution; zero pressure rise; 8° diffuser; seven nozzles in 3-in. mixing section.

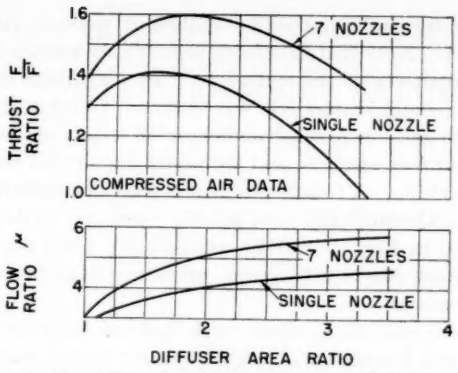

FIG. 16. Effect of multiple nozzles on diffusers.

in performance will be incurred by having the nozzle extend into the duct, other than that which may result from reduction of the effective mixing length. Since the distance from the exhaust stacks to the ejector exit is usually critical in ejector installations, there is no point in withdrawing the nozzles far out of the duct.

In general, the same considerations hold for intermittent flow ejectors as for steady flow ejectors. It is important that the exhaust be correctly distributed in the ejector area. Care should be taken that the stacks exhaust straight in the ducts and do not strike the duct walls. It is extremely important that the stacks do not extend into the duct unless three nonoverlapping cylinder exhausts are Siamesed together for each nozzle. Otherwise, during any given period of the cycle the mixing area is reduced by the blocking effect of the stacks that are not firing.

DIFFUSER ANGLE

The experimental coefficients used in the theoretical calculations were based on ejectors having 8° conical diffusers. The efficiency of such a diffuser is not constant for different diameters and different area ratios. However, in lieu of a more thorough analysis of diffusers and adequate experimental data, it is suggested that 8° conical diffusers be used or, in the case of noncircular cross sections, that diffusers with equivalent cone angle be used (i.e., maintain the same change in area for a given length that a cone with an included angle of 8° would have). Experience has shown this to be a fairly good criterion for designing a diffuser, although it is not fundamentally correct.

For a given overall length somewhat more flow can be obtained at the expense of a loss in thrust by using a greater diffuser angle. This would be practical only in a case where the overall length was limited and it was desired to obtain the maximum flow without regard to the thrust.

It has also been found that the optimum diffuser angle is greater than 8° for extremely small diffuser area ratios. The data are meager, however, and no reliable recommendations can be made for such cases.

DESIGN OF AN INSTALLATION

The foregoing equations and figures should enable the designer to make a rough check on the suitability of an ejector for his particular needs. The final design will, for the time being, have to be verified by flight tests, preferably of several configurations, which seem to be near the optimum.

In any type of installation it is first necessary to find the state of the secondary fluid, the required pressure rise, and the mean state of the primary fluid as described by the intermittent flow analogy (see Eqs. (19), (20), and (21). Strictly speaking, the state of the primary fluid should be obtained at the pressure of the ejector throat, but for most airplane installations the state at atmospheric pressure is close enough. It should be remembered, however, that in the case of a supersonic primary jet, the primary area should be calculated as if the jet had expanded through a converging diverging nozzle, rather than using the throat area as the primary area. The pressure rise of the secondary fluid is usually taken to atmospheric pressure, mainly because of lack of better knowledge of the static pressure at the ejector exit. The calculated thrust will then be roughly correct, even though the calculations may indicate a larger diffuser than will actually be needed. Having determined the states of the primary and secondary fluids, the designer can calculate the required flow ratio, density ratio, and pressure rise coefficient.

Since an adjustable diffuser is mechanically difficult to build, this will be one of the limitations in design. The overall length and the ejector area will be two other limitations imposed by the airplane designer and these must be balanced against the desired performance. If the thrust is not important but the diffuser area ratio is, then the mixing section area for the minimum diffuser can be found from Eq. 15. The required diffuser area ratio can be estimated by solving the flow equation (Eq. 13) for K and finding the area ratio from the empirical plot of flow coefficient, K, vs. diffuser area ratio, Fig. 2. If length is a more critical item than diffuser area ratio, a reduction may sometimes be made by using a slightly smaller mixing section area and a larger diffuser area ratio. The mixing length may be reduced by the use of multiple or annular nozzles.

If thrust is most important, the diffuser area ratio for maximum thrust may be estimated from Fig. 5 and the mixing section area found from Fig. 4 at the given pressure rise coefficient, flow ratio, and diffuser area ratio. If the density ratio differs much from 3.5, or if more precision is desired, the optimum diffuser must be found by assuming several values of mixing section area ratio, solving the flow equation (Eq. 13) for the flow coefficient, K, finding the corresponding diffuser area ratio, α, and then solving the thrust equation (Eq. 14) to find which assumed area ratio gave maximum thrust. For more accurate work, the state of the

primary fluid should be taken at the pressure in the ejector throat rather than at atmospheric pressure.

In the usual airplane installation, however, if an ejector is required at all it should be designed to operate with the maximum allowable diffuser in the most critical cooling condition. Then the diffuser can be closed down at high speeds to prevent overcooling and to increase the thrust. This procedure will seldom result in a diffuser at high speed that is greater than the optimum for thrust.

Outstanding Problems in Ejector Design

There are several uncertainties regarding the performance of ejectors which have not been adequately dealt with. First, there are practically no data on the effect of ejectors on low pressure areas into which they may be discharged, so that for the time being the assumption of atmospheric discharge pressure is used. In the second place, the mixing process has not been considered in detail except by the limited work of Ledgett.[3] Certainly the optimum mixing length varies with Reynold's Number, the steadiness of the flow, the pressure rise on the mixing section, and other quantities. It is still necessary, however, because of lack of better knowledge, to assume that the mixing cone spreads out at a constant angle. A third uncertainty may be observed by studying the plot of flow vs. pressure rise in Fig. 11. Note that the points are actually waving back and forth across the mean line. This waviness is not experimental scatter but was observed to some extent at high and low Mach Numbers, with steady and intermittent flow ejectors, and with both air-air and steam-air ejectors. A fourth problem is that of intermittent flow. Although the data usually correlate, as demonstrated in Figs. 9 and 10, occasionally some peculiar resonance effects will appear, upsetting all estimates of performance.

These problems, along with lack of accurate and complete knowledge of engine exhaust thrust, make it impossible to design ejectors precisely. At the present time, therefore, it seems sufficient to estimate the ejector performance roughly from the foregoing plots and equations, and then to modify the final design after flight-test data are available.

References

[1] Flugel, Gustav, *The Design of Jet Pumps*, N.A.C.A. T.M. No. 982, 1941.

[2] Gosline, James E., and O'Brien, Morrough P., *The Water Jet Pump*, University of California Publications in Engineering, Vol. 3, No. 3, p. 67, 1934.

[3] Ledgett, Lowell A., *The Mixing Fluid Streams*, Preprinted paper, Aero. Hydraulics Meeting, A.S.M.E., Berkeley, Calif., 1934.

Changes of Address

To facilitate the prompt receipt of copies of the JOURNAL OF THE AERONAUTICAL SCIENCES, members and subscribers are requested to give the Institute 30 days' notice of any change of address.

Notices should be sent directly to:

Institute of the Aeronautical Sciences, Inc.
2 East 64th Street, New York 21, New York

Determination and Presentation of Compressive Stress-Strain Data for Thin Sheet Metal

WALTER RAMBERG* AND JAMES A. MILLER†
National Bureau of Standards

ABSTRACT

Various methods of obtaining the compressive stress-strain curve of thin sheet metal are described, and their advantages and limitations are briefly discussed. The presentation of stress-strain data in dimensionless form is outlined, and the advantages of such a presentation in correcting for the effect of variations in yield strength and in Young's modulus are brought out. Attention is called to a classification of stress-strain curves by shape factors following a three-parameter formula proposed by Osgood.

INTRODUCTION

THE CURRENT INTEREST in methods of obtaining and presenting stress-strain curves of thin sheet metal in compression dates from the introduction of stressed skin structures in aircraft 10 or 15 years ago. The first stressed-skin structures were relatively inefficient because buckling in compression could be expected well inside the elastic range and, therefore, there was little need to know compressive properties beyond the elastic range. As the structures became more efficient, it became of increasing importance to know not only Young's modulus, which describes the stress-strain curve inside the elastic range, but also the stress-strain curve beyond the elastic range. In the beginning the materials testing engineers were able to pacify the designers who were asking for this information by making tensile tests preferably in a transverse direction and telling them that the stress-strain curve in longitudinal compression would be approximated by the tensile stress-strain curve in a transverse direction. This was good enough for some commonly used aluminum alloys, such as 17S-T and 24S-T,[1] but it soon proved entirely inadequate for other alloys, particularly stainless steels[1] and magnesium alloys.[2] In the case of these alloys no simple and reliable method has been found for determining longitudinal compressive properties from any tensile properties. In the end the materials engineers had to give in and make compressive tests of these alloys to determine their compressive properties. Several methods of testing have been developed and used. All of them have their limitations and none of them is in sufficiently general use to have earned for itself inclusion in the A.S.T.M. Standards.

A brief survey of the various known methods seems advisable at this time for the benefit of structural test engineers who are faced with the problem of making compressive tests without having had the time to look into the various methods.

The National Bureau of Standards is favorably situated for assembling such a survey, since it has been concerned with developing methods of compressive testing of thin sheet metal for the Bureau of Aeronautics, Navy Department, and for the National Advisory Committee for Aeronautics since 1933. The N.B.S. has also been concerned with methods of presenting these data in a rational form which would reduce the testing of specimens of similar materials to a minimum.

In reviewing the various methods for making compressive tests of thin sheet metal one must admit from the outset that the experience of the National Bureau of Standards is limited insofar as it does not cover all of the ingenious methods that have been developed. In several cases, therefore, the authors had to base their review on articles in the technical literature rather than on their own experience.

METHODS OF DETERMINING THE COMPRESSIVE STRESS-STRAIN CURVES OF THIN SHEET METAL

All methods of making compressive tests of thin sheet metal have one problem in common—namely, the problem of overcoming the tendency of the specimen to become increasingly misaligned with increasing load and finally to fail by instability. An ideal solution of the problem requires the provision of simple and easily applied supports that prevent buckling without introducing friction between supports and specimen and without introducing restraint to lateral expansion of the specimen as the axial load is increased.

It will be noted in this connection that the tensile test is favored relative to the compressive test insofar as alignment and stability improve with increasing load instead of becoming worse. The testing machine may add to the difficulties of the compressive test by becoming unstable[3] or otherwise permitting a lateral displacement or a rotation of one head relative to the other. In order to obtain suitable loading conditions, various

Presented at the Structures Session, Fourteenth Annual Meeting, I.A.S., New York, January 29–31, 1946. Revised and received August 27, 1946.

* Physicist.

† Materials Engineer.

auxiliary devices have been used such as backlash eliminators, means for guiding one of the heads to restrict lateral movement relative to the other head of the machine, or a subpress. Fig. 1 shows a subpress developed for this purpose at the National Bureau of Standards.[4]

The various methods of making compressive tests differ principally in the means of support against premature buckling and in provision for attaching strain gages. The methods are discussed below in roughly chronological order. They are illustrated by sketches in Fig. 2 for convenient identification by the reader.

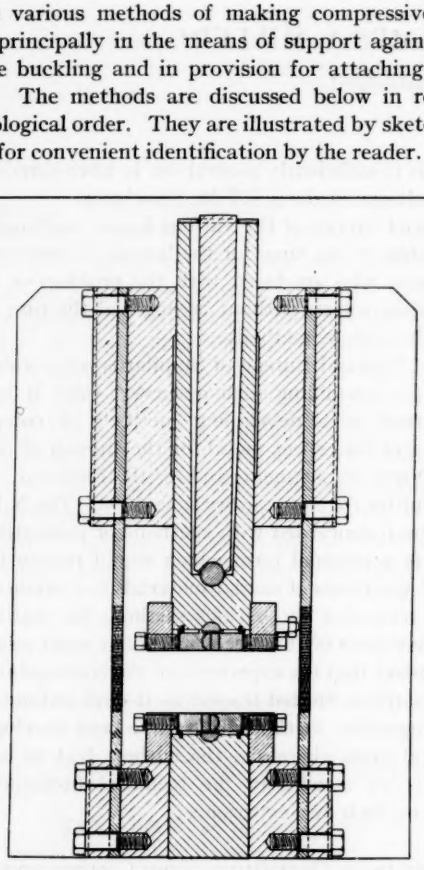

FIG. 1. N.B.S. subpress 50,000-lb. capacity.

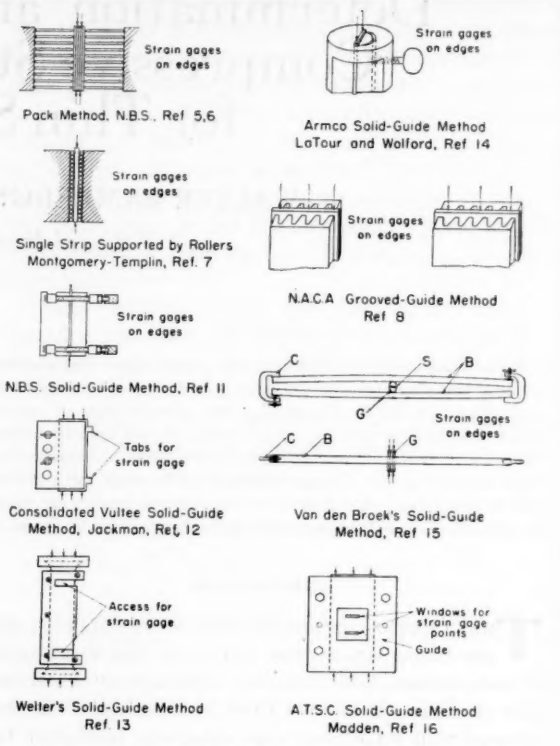

FIG. 2. Methods for compressive tests of sheet metal.

Pack Method

The earliest successful method for testing thin sheet in compression of which the authors have any knowledge is the pack method developed by Aitchison and Tuckerman of the National Bureau of Standards.[5] In the pack method the leaf to which the gages are attached is supported on each side by an equal number of leaves from the same sheet which are identical with the middle leaf except for being slightly narrower to ensure that the strain gages are attached only to the middle leaf. The ends of the "pack" consisting of the middle leaf and the supporting leaves are ground flat and parallel, and the pack is then tested as a single stocky compressive specimen (Fig. 3). Lateral buckling of the outer leaves of the pack is prevented by three rows of steel pins on each side, $1/4$ in. between centers, which are supported by a rigid frame connected to the lower platen of the testing machine. The pack is loaded through

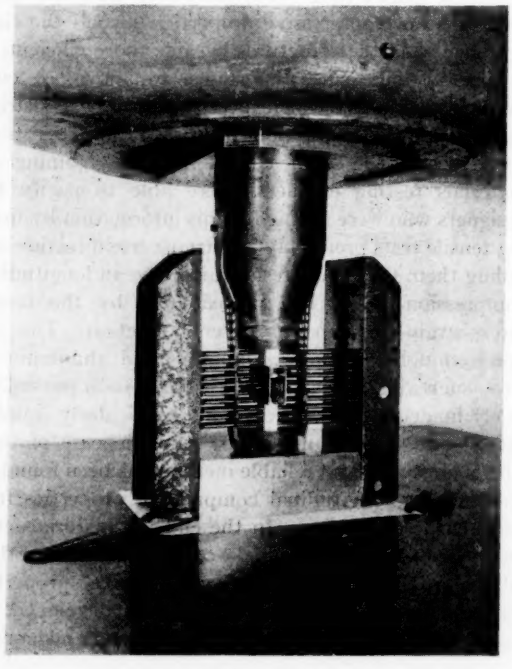

FIG. 3. Pack ready for test.

hardened and ground steel bearing blocks with an intermediate shim of plaster of Paris which is allowed to harden under an initial load of about 500 lbs. Strains

are measured by a pair of strain gages attached to the middle leaf of the pack.

A number of modifications of the pack method have been made to simplify it and to extend its use to thinner sheet or stronger materials. Among these are the use of clamps, which are placed near the ends of the pack before machining the ends and which are left on during the test, and the use of a spherically seated bearing block at one end of the specimen. Various sizes of specimens have been used. In general, the length is at least twice the width plus the gage length. The Aluminum Research Laboratories have found it unnecessary to make the middle leaf of the pack wider than the supporting leaves. Aitchison[6] found that thinner material could be tested when the leaves were bonded together by shellac applied in liquid solution at room temperature, dried, and then baked in a clamp at a temperature of about 65°C. Using this last technique Aitchison was able to determine compressive stress-strain curves beyond the yield strength on packs of 0.020-in. sheet material with a yield strength of more than 215,000 lbs. per sq.in.

Comparative tests[5] showed that the yield strength of a material determined by the pack method was very nearly the same as that determined by a test on a solid specimen.

Single Strip Supported by Rollers

Several schemes were soon tried to improve on the pack test by reducing the time required for machining the specimen, the sample of material required, and the maximum load required of the testing machine. One of the most successful of these tests is the test of a single leaf or strip supported by rollers, which was suggested by W. P. Montgomery and developed further by R. L. Templin and his associates of the Aluminum Research Laboratories.[7]

The fixture is shown in Fig. 4. The specimen consists of a piece $^5/_8$ by $2^5/_8$ in. cut from the sheet metal. It is slipped between two sets of hardened steel rollers 0.093 in. in diameter and spaced 0.1 in. between centers. The rollers are clamped against the specimen by tightening the screws. A portion of the specimen, usually about 0.03 in. long, projects above the fixture to provide clearance between the upper bearing block and the fixture at the maximum strain. Strain is usually measured by a pair of gages attached to the edges of the specimen. Sometimes an autographic gage is attached to one of the edges of the specimen.

Successful compressive tests, with results in close agreement with those obtained by the pack method and by tests on solid specimens, have been made with the Montgomery-Templin fixture on specimens of 24S-T aluminum alloy down to 0.020 in. in thickness.[7] For thicknesses below 0.020 in., difficulties have been experienced because of buckling at the top. This sometimes causes damage to the roller supports. The difficulty has sometimes been overcome by cementing together a number of leaves as in the "modified pack method."[6] Kotanchik, Woods, and Weinberger[8] state that the roller supports must be constructed with precision, and they report that unreliable test results were obtained because of an inaccurately constructed support. Indentation of specimens by the rollers has also been observed. Modifications in the method include the use of a specimen $^1/_2$ by $2^1/_2$ in., a cylindrical seat for one of the steel blocks, and a single screw working against an equalizing bar for adjustment.

The time saved in preparation of the specimen as compared to the pack test is considerable. The saving is greater the thinner the material, since a greater number of single strips can be machined at one time. Some time can also be saved in setting up the specimen for test.

N.B.S. Solid-Guide Method

The work with solid guides at the National Bureau of Standards was started by C. S. Aitchison in 1939; in 1942 he substituted lubricated brass plates for the rollers of a Montgomery-Templin fixture.[9] Further development of the method resulted in the design of the fixture with tool steel guides, Fig. 5, which is described briefly in reference 10 and more fully in reference 11.

The lubricated faces of the steel guides have a length of 2.20 in. and a width of 0.46 in. The specimen is made about 0.04 in. wider, but in no case is it more than

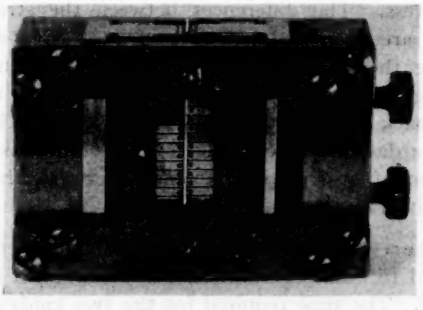

Fig. 4. Specimen in Montgomery-Templin fixture.

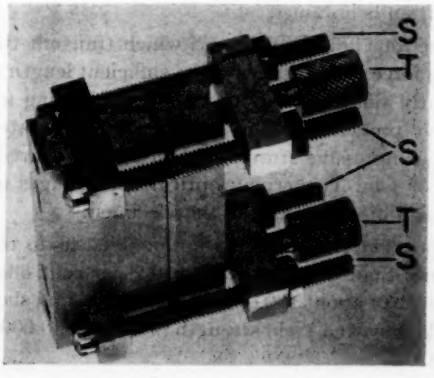

FIG. 5. Specimen between N.B.S. lubricated steel guides.

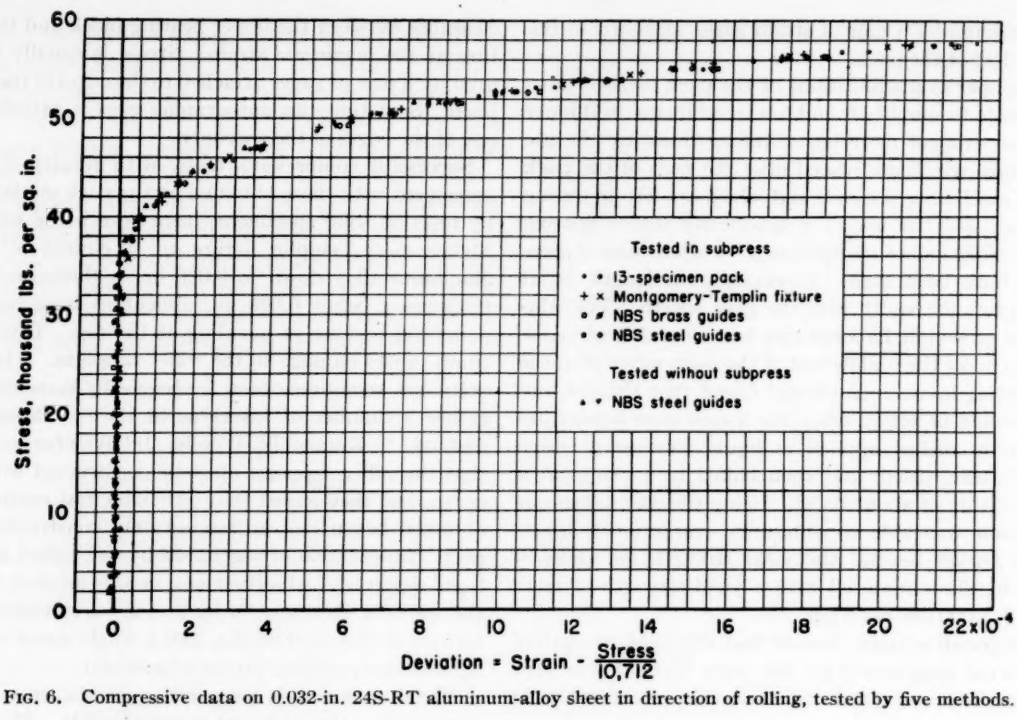

FIG. 6. Compressive data on 0.032-in. 24S-RT aluminum-alloy sheet in direction of rolling, tested by five methods.

four thicknesses wider than the guides. The initial unsupported length is made sufficiently small to prevent buckling at the ends before the yield strength is reached; it is made sufficiently large to provide clearance between the upper bearing block and the guides at the maximum strain. The initial unsupported length for specimens thicker than 0.02 in. is about 0.05 in.; for specimens from 0.01 to 0.02 in. it is about 0.03 in. A thin film of heavy-duty lubricant for automobile wheel bearings* is spread on the specimen and the specimen is placed between the two guides. The adjusting screws T are tightened and retightened with intervening sliding of the specimen until the guides will not slide down under their own weight but will slide smoothly under an additional weight of 1 lb. or less. After a little practice it is possible to tell by feel when the desired condition is obtained.

The four holding screws S which transmit the tightening force to the guides are of sufficient length and sufficiently small section to prevent the setting up of excessive pressures as the specimen expands laterally at high compressive strain. Strains are measured with a pair of 1-in. Tuckerman optical strain gages mounted on the projecting edges of the specimen.

The solid-guide method has enabled us to test sheet thinner than 0.006 in., with a 0.2 per cent offset yield strength of about 160,000 lbs. per sq.in., and sheet 0.020 in. thick with a yield strength of about 240,000 lbs. per sq.in.

* Texaco Marfak No. 3 was the only grease of this type tried.

Tests on specimens with thicknesses of from 0.01 to 0.128 in. have been made by inexperienced personnel following routine procedure, with results that closely agreed with those obtained by experienced personnel. For thinner specimens more care is required, particularly with regard to the thickness of the lubricant film.

Tests made with solid guides, with the Montgomery-Templin fixture, and by the pack method on various sheet metals were reported in reference 11. The results obtained by the various methods were in close agreement. For example, Fig. 6 shows compressive stress-strain data for longitudinal specimens from a sheet of 0.032-in. 24S-RT aluminum alloy which were obtained by five methods at the National Bureau of Standards. The tests were made by the pack method, with the Montgomery-Templin fixture, with lubricated brass guides, with lubricated steel guides, all with the subpress, and with lubricated steel guides without the subpress. The differences between the stress-strain data are magnified by plotting as a stress-deviation curve, the abscissa being the deviation from an average straight line through the points in the elastic range for the pack and Montgomery-Templin tests. The stress-strain data are in close agreement. There is no indication of systematic differences between the results obtained by the various methods.

The results obtained with the solid-guide method were found to be as consistent as those obtained in tensile tests. The time required for the two kinds of test is about the same.

Consolidated Vultee Solid-Guide Method

One of the earliest published methods for obtaining the compressive stress-strain curve of thin sheet metal from tests of single specimens between lubricated solid guides is due to K. R. Jackman of Consolidated Vultee Aircraft Corporation.[12]

In this method the specimen consists of a piece 1 by $3^1/_8$ in. with two tabs on one side (Fig. 2), punched from the sheet. The ends are finished by milling or grinding. The tabs serve as points of attachment for a 2-in. extensometer, which may be of any type with a 2-in. gage length. The specimen is guided between greased plates of either metal or wood. Reference 12 contains no data on the minimum thickness of specimen that can be tested successfully or on the accuracy of the test. However, it is emphasized that the method has an advantage for industrial use in saving time. It is stated that an experienced testing-machine operator can carry through a test on a specimen in from 8 to 10 min. if he uses a Southwark-Templin autographic strain recorder to record the stress-strain curve.

The Consolidated Vultee method has not been used at the National Bureau of Standards where precision is more important than the saving of time, because errors may be introduced by reading strains on tabs on one edge of the specimen and errors may be caused by changing the properties of the material along the edges in the punching operation.

Welter's Solid-Guide Method

Professor Georges Welter of the École Polytechnique de Montreal used lubricated guides to support compressive specimens of 0.032-in. 17S-T aluminum-alloy sheet.[13] Few details of the method are given. Three different devices are shown with cutouts to permit the attachment of gages to the sides of the specimen. The compressive load is introduced into the specimen through blocks that are fixed to the specimen either mechanically or with Wood's metal (Fig. 2). The specimens are $^3/_4$ in. wide at the ends and $^1/_2$ in. wide in the reduced section.

No data obtained by other methods on the same sheet are given from which the reader may judge the accuracy of the method. However, autographic curves obtained with a nonaveraging 2-in. extensometer are not nearly so smooth as those shown for the tensile tests.

An adequate study of the method seems necessary to ascertain that the results are not in error because of nonuniformity in strain distribution, frictional forces between guides and specimen, and buckling in the unsupported portions of the specimen. It would be desirable to make additional tests to determine the applicability of the method to sheet stronger and also thinner than that tested.

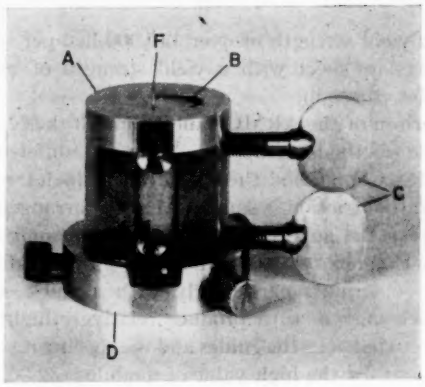

FIG. 7. ARMCO single-strip compression jig.

ARMCO Solid-Guide Method

LaTour and Wolford of the American Rolling Mill Company Research Laboratories have developed a particularly compact fixture for testing single strips between lubricated steel guides. The procedure is described in detail in reference 14. Fig. 7 shows the specimen *F* clamped in the fixture between the movable guide *B* and the flat guiding surface on the rigid frame *A*. A light coat of graphite grease or oil is applied to the specimen as lubricant. The guides are clamped on the specimen by tightening thumb screws *C* with moderate pressure. A positioning ring, *D*, is used to center the fixture midway between the bearing blocks.

Strain gages with a 1-in. gage length are attached to both edges of the specimen, where the guides are cut away, to measure strain under load. An approximately uniform load distribution is obtained by loading the specimen in a testing machine between bearing blocks resting on wet blotting paper. A preload of 25 to 100 lbs. is applied and the thickness of the blotting paper is adjusted by rubbing away at the appropriate side until the strain gages indicate approximately the same strain on the two edges of the specimen. The fixture is also used in conjunction with an autographic compressometer that measures the change in distance between the bearing blocks. A correction for "foundation effect" is given.

Compressive tests were made with the fixture on specimens 0.035, 0.054, and 0.100 in. thick, cut from a bar of SAE 4330 steel. The values of initial modulus of elasticity and of yield strength from data obtained with gages at the edges of the specimen were all within 2 per cent of the values obtained on a solid cylinder of the material, with the exception of the modulus of the 0.100-in. specimen. As is to be expected, the data obtained with the autographic recorder were not so consistent. The yield strength, offset = 0.2 per cent, has been obtained by this method on sheet as thin as 0.01

in. with a yield strength of over 140,000 lbs. per sq.in. and on 0.02-in. sheet with a yield strength of about 180,000 lbs. per sq.in.

Comparison of the ARMCO method with the N.B.S. solid-guide method shows two principal differences. In the ARMCO method there is no check to determine that the initial friction is small. Also, the arrangement for clamping the guides is more rigid. This may lead to the development of excessive lateral pressure at high compressive strains, particularly with a thick specimen, which may in turn produce relatively high frictional forces between the guides and the specimen. This may account for the high value of modulus (32,000,000 lbs. per sq.in.) for the 0.100-in. specimen that is reported in Table I of reference 14. It may also account for the relatively low strains for a given stress above 70,000 lbs. per sq.in. that are reported for single strips in Fig. 7 of reference 14 as compared to the strains measured on an unsupported solid cylinder from the same material.

Two further differences between the two methods are the use of a positioning ring and of a shim of wet blotting paper in the ARMCO method. Our experience with the N.B.S. solid-guide method indicates that good results can be obtained without these expedients.

N.A.C.A. Grooved-Guide Method

Kotanchik, Woods, and Weinberger of the N.A.C.A. made a study[8] of compressive tests in which the specimen was guided between lubricated brass plates with opposite and with offset vertical grooves, Fig. 2. The brass plates were held in a modified Montgomery-Templin fixture. For comparison they also made tests on specimens guided between rollers and between flat brass guides, as in reference 9, and between flat wooden plates.

Tests made on 0.064-in. aluminum-alloy sheets showed good agreement between the results obtained with the various types of support as long as the initial lateral pressure between the guides and the specimen did not exceed 45 lbs.

In the tests with the offset-grooved guides the values of Young's modulus were in close agreement with those obtained in the test with rollers for the whole range of initial lateral pressure (22 to 380 lbs.). However, the indicated yield strengths increased with pressure above 45 lbs. This indicates that an appreciable fraction of the load was by-passed as a frictional force between the guides and the specimen. Such a frictional force may be expected to arise in a relatively rigid retaining clamp, such as the Montgomery-Templin fixture, since the specimen tries to expand laterally at high compressive strains. This brings out again the advisability of introducing a certain amount of flexibility in the clamps to prevent the building up of excessive lateral pressures at high compressive strains.

Van den Broek's Solid-Guide Method

Van den Broek has recently described a method of testing single strips of thin sheet in compression between solid guides in which a simple and ingenious means is employed to keep the lateral pressure nearly independent of the load on the specimen.[15]

A sketch of Van den Broek's fixture is reproduced in Fig. 2. The specimen, *S*, is clamped between the 3- by 1-in. flat surfaces of two cast-iron guides, *G*. No lubricant is used between the guides and the specimen. The clamping pressure is applied through a pair of 1-in. square bars, *B*, which are 40 in. long and which are held together at the ends by C-clamps, *C*. The C-clamps are tightened by trial and error to develop the minimum clamping pressure that will prevent buckling of the specimen before the yield strength is reached. The bars, *B*, are of sufficient flexibility so that the variation in clamping pressure with increasing compressive strain is negligible during a given test.

In the absence of lubricant between guides and specimen an appreciable portion of the load applied by the testing machine may be by-passed through the guides by friction. A correction to each stress-strain curve is made by assuming that the frictional error develops very fast during the early stages of the test and then remains constant during the test. From the illustration given it would seem that such a correction could not be made accurately for Alclad and other sheet where the stress-strain graph begins to curve at low stresses. It is not clear from reference 15 what steps are taken to prevent stressing of the specimen by the weight of the fixture, which is estimated to be about 25 lbs.

No comparisons are given with stress-strain curves obtained by other methods. The method in its present state of development does not seem well adapted to routine testing.

Van den Broek's method has not been tried at the National Bureau of Standards. If it should be tried, an attempt would probably be made to reduce the friction between the guides and the specimen with a lubricant as in the N.B.S. fixture.

A.T.S.C. Solid-Guide Method

Major B. C. Madden of the Air Technical Service Command at Wright Field has developed a method of testing single-sheet specimens in compression between lubricated steel guides, which is described in reference 16.

In the A.T.S.C. method the specimen, *S*, Fig. 8, is 1.800 ± 0.010 in. wide and usually 5.500 ± 0.005 in. long. It is supported against buckling by being clamped between the ground faces of two guide plates, which are spaced by shims to leave a total clearance of 0.0005 to 0.005 in. between the specimen and the plates. This clearance is filled with lead soap base grease. Each plate has two 0.12- by 0.80-in. apertures to provide ac-

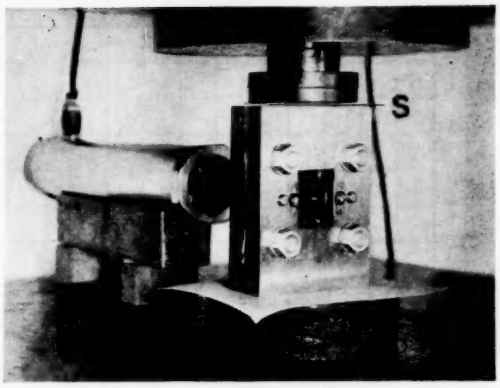

FIG. 8. A.T.S.C. fixture.

cess for 1-in. gages to the center of both faces of the specimen. The dimensions of these windows are made small to prevent buckling of the specimen before the yield strength has been attained. Strain is usually measured with a pair of 1-in. Tuckerman strain gages. The load is applied through a spherically seated bearing block acting on the top end of the specimen through a 0.040- by 1- by 2-in. piece of relatively soft metal. The amount of friction between guiding plates and specimen is limited by requiring that the specimen should slide under a load of 5 lbs. at the beginning of the test. With this precaution it appears from tests reported in reference 16 that friction at the maximum load is less than 8 lbs.

Reference 16 shows close agreement between stress-strain curves obtained by the A.A.F. method and by the pack method on hard-rolled 0.035-in. manganese steel.

The minimum thickness of specimen that can be tested to its yield strength is limited by the tendency to develop a buckle at the apertures for the strain gages. It is estimated in reference 16 that the minimum thickness is about 0.02 in.

Since the specimen is much wider than the specimens of other methods, relative tilting of the heads causing differences in strain at the two edges would cause greater inequalities of strain, for the same tilt, than for other methods. No measurements of this inequality can be made with gages at the center of the width. Difficulties in obtaining proper contact which are encountered for thin specimens might be avoided by the use of a cylindrically seated bearing block in place of the spherically seated block.

PRESENTATION OF STRESS-STRAIN CURVES

Compressive stress-strain curves must usually be known with greater accuracy than tensile stress-strain curves because of the dependence of buckling loads at high stresses on the shape of the knee of the stress-strain curve. In estimating buckling loads it is important to know the tangent modulus vs. stress curve—i.e., the slope of the stress-strain curve rather than the stress-strain curve itself.

A rough approximation to the stress-strain curve can sometimes be constructed from a knowledge of Young's modulus and yield strength by drawing a modulus line to the yield strength and continuing with a horizontal line. More is certainly needed for even the roughest approximation to the tangent modulus vs. stress curve. With new materials especially it will be necessary to obtain a complete stress-strain curve and tangent modu-

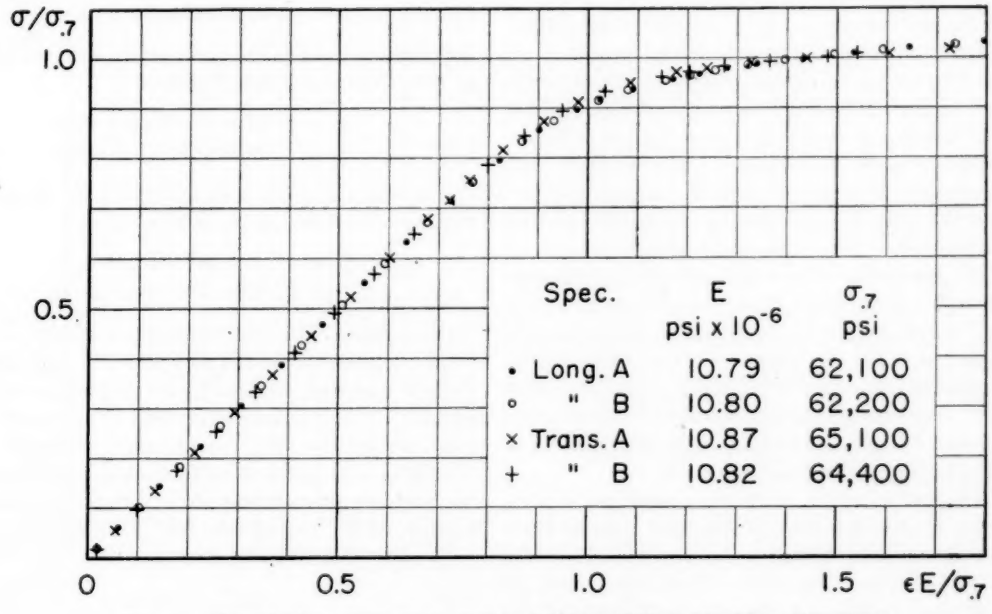

FIG. 9. Dimensionless stress-strain graphs, 0.064-in. R301-T aluminum-alloy sheet.

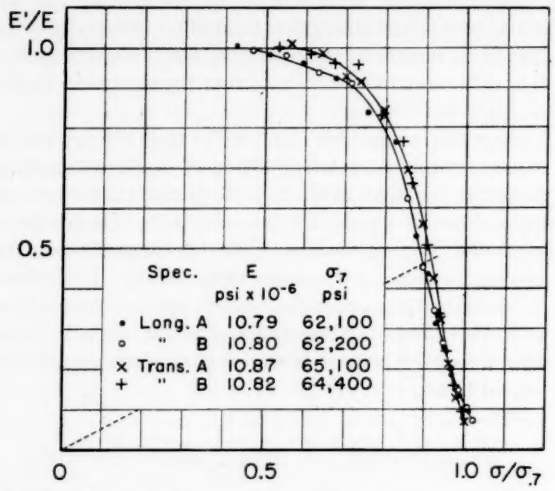

FIG. 10. Dimensionless tangent modulus versus stress graphs, 0.064-in. R301-T aluminum-alloy sheet.

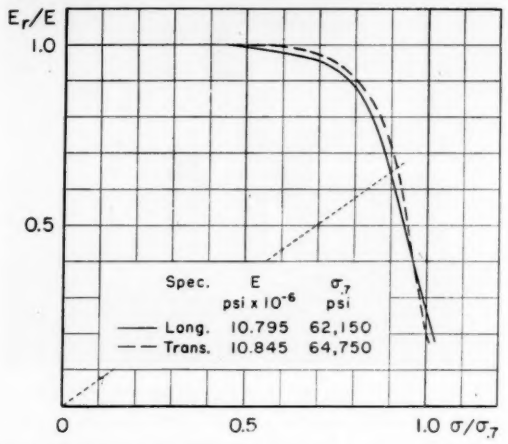

FIG. 11. Dimensionless reduced modulus versus stress graphs, 0.064-in. R301-T aluminum-alloy sheet.

lus vs. stress curve by an accurate method. However, it would be unfortunate if such complete stress-strain curves were to be required for each new batch of a given material.

Fortunately, it turns out[17] that the stress-strain curves of many materials, particularly materials of the same nominal composition and treatment, are affine. This means that the stress-strain curves can be brought into coincidence by multiplying the stresses by a suitable factor and the strains by another suitable factor. These factors are preferably chosen to reduce the ordinary stress-strain curve to a dimensionless stress-strain curve in which the effects of variations in Young's modulus and in yield strength are eliminated.

Fig. 9 shows the dimensionless stress-strain graphs for two longitudinal and two transverse specimens of 0.064-in. R301-T aluminum-alloy sheet. The coordinates σ, ϵ of the stress-strain curve have been replaced by the dimensionless coordinates $\sigma/\sigma_{0.7}$, $\epsilon E/\sigma_{0.7}$, where E is Young's modulus and where $\sigma_{0.7}$ denotes the secant yield strength defined as the ordinate of the intersection with the stress-strain curve of a line through the origin with a slope $0.7E$. The conventional 0.2 per cent offset yield strength could not be used for the reduction since it will not reduce affinely related stress-strain curves to a common curve. The secant yield strength for a slope of $0.7E$ was chosen because examination of the stress-strain curves of reference 1 indicated that the secant yield strength for this slope comes near to the conventional 0.2 per cent offset yield strength for a number of high-strength sheet materials.

A dimensionless curve of tangent modulus, E', vs. stress may be derived directly from the dimensionless stress-strain curve by plotting the slope, E'/E, of the curve against $\sigma/\sigma_{0.7}$ (Fig. 10). From this curve, in turn, one may compute a dimensionless curve of the reduced modulus for a rectangular section:

$$E_r/E = 4E'/E(1+\sqrt{E'/E})^2 \qquad (1)$$

This is shown in Fig. 11.

Example for Use of Dimensionless Tangent-Modulus and Reduced-Modulus Curves

An example will be given to illustrate the application of these dimensionless tangent-modulus and reduced-modulus curves to estimate the effect of variations in Young's modulus and in yield strength for materials with affinely related stress-strain curves.

A structure fabricated from 0.064-in. R301-T aluminum-alloy sheet buckles under compressive loads acting in the longitudinal direction at a stress of

$$\sigma = 55{,}000 \text{ lbs. per sq.in.}$$

Compressive tests of the sheet give the following properties for the longitudinal direction

$$E = 10.8 \times 10^6 \text{ lbs. per sq.in.}$$
$$\sigma_{0.7} = 62{,}000 \text{ lbs. per sq.in.}$$

The buckling stress is to be estimated for similar material having "minimum properties" of

$$E = 10.4 \times 10^6 \text{ lbs. per sq.in.}$$
$$\sigma_{0.7} = 57{,}000 \text{ lbs. per sq.in.}$$

It is assumed that the stress-strain curves in longitudinal compression of the test material and the hypothetical material with minimum properties are affinely related. The buckling stress will be computed under two assumptions (see, for instance, reference 18, pp. 384–390). For the first computation it is assumed that the buckling stress is proportional to the tangent modulus and, for the second case, that it is proportional to the reduced modulus. In the first case then

$$\sigma/E' = \text{const.}$$

and in the second case

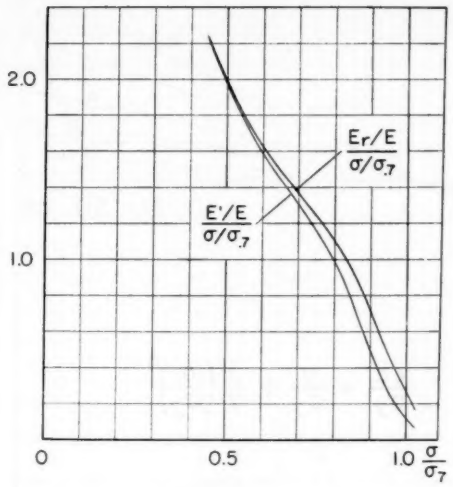

FIG. 12. Auxiliary curves for estimating changes in buckling stress with changes in $\sigma/\sigma_{0.7}$, 0.064-in. R301-T aluminum-alloy sheet in longitudinal compression.

$$\sigma/E_r = \text{const.}$$

The test material will be denoted without an asterisk and the hypothetical material with minimum properties by an asterisk.

For the test material

$$\sigma/\sigma_{0.7} = 55{,}000/62{,}000 = 0.89$$

Carrying through the computation for the first case, one obtains from the dimensionless curve of tangent modulus in longitudinal compression, Fig. 10,

$$E'/E = 0.48$$

Hence, the tangent modulus for the test material is

$$E' = 0.48 \times 10.8 \times 10^6 = 5.18 \times 10^6 \text{ lbs. per sq.in.}$$

and the fixed ratio

$$\sigma/E' = \sigma^*/E'^* = 55{,}000/5.18 \times 10^6 = 0.01062$$

For the hypothetical material

$$\sigma_{0.7}{}^*/E^* = 57{,}000/10.4 \times 10^6 = 0.00548$$

Combining this ratio with the previous ratio gives the following equation for σ^*:

$$\frac{\sigma_{0.7}{}^*/E^*}{\sigma^*/E'^*} = \frac{E'^*/E^*}{\sigma^*/\sigma_{0.7}{}^*} = \frac{0.00548}{0.01062} = 0.516$$

This equation may be solved for $\sigma^*/\sigma_{0.7}{}^*$ by drawing a line (shown dotted) through the origin of Fig. 10 with a slope of 0.516 and determining the abscissa of intersection with the modulus curve for longitudinal compression. Or it may be solved very simply with the auxiliary curve for $(E'/E)/(\sigma/\sigma_{0.7})$ in Fig. 12.

The following value is obtained

$$\sigma^*/\sigma_{0.7}{}^* = 0.895$$

The estimated buckling stress is therefore

$$\sigma^* = 57{,}000 \times 0.895 = 51{,}000 \text{ lbs. per sq.in.}$$

For the second case, one obtains analogously from Figs. 11 and 12

$$E_r/E = 0.67$$

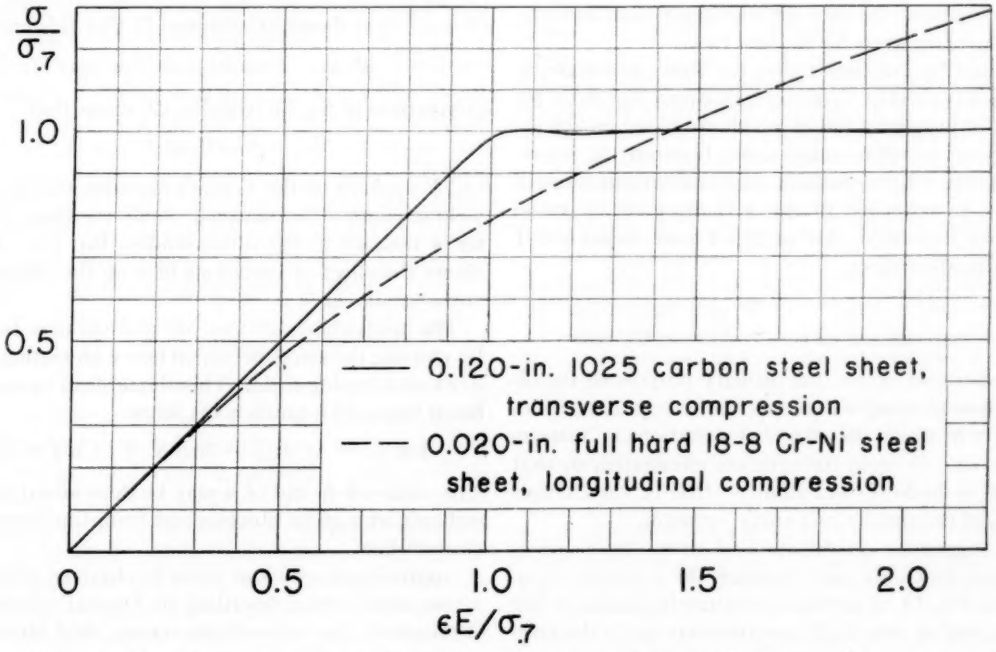

FIG. 13. Dimensionless compressive stress-strain curves having markedly different shapes.

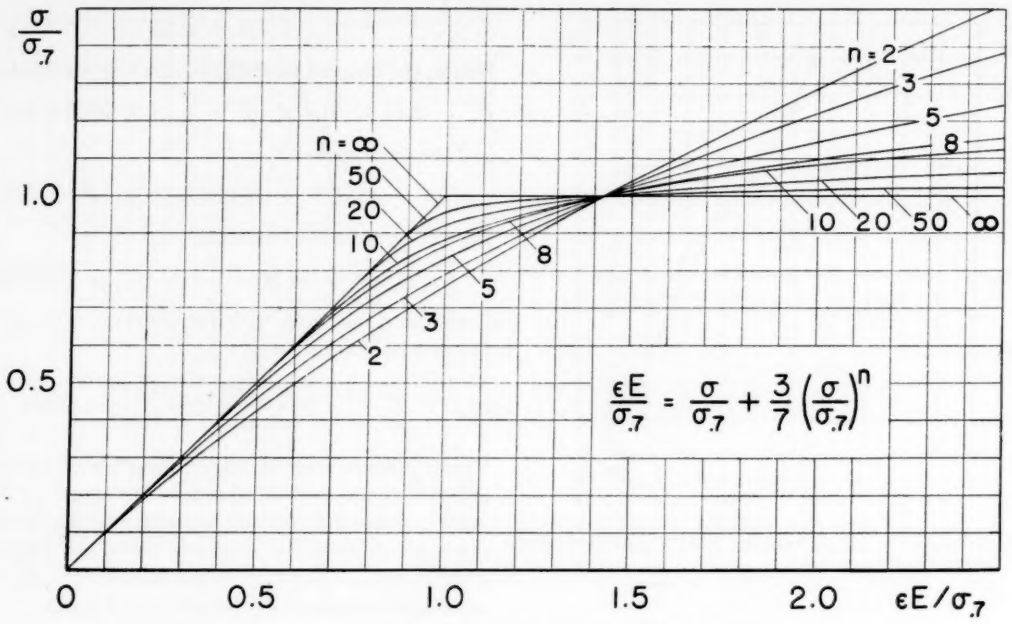

FIG. 14. Dimensionless stress-strain curves described by Eq. (3).

$$E_r = 0.67 \times 10.8 \times 10^6 = 7.24 \times 10^6 \text{ lbs. per sq.in.}$$

$$\sigma/E_r = \sigma^*/E_r^* = 55{,}000/7.24 \times 10^6 = 0.00760$$

$$\sigma_{0.7}{}^*/E^* = 57{,}000/10.4 \times 10^6 = 0.00548$$

$$\frac{\sigma_{0.7}{}^*/E^*}{\sigma^*/E_r^*} = \frac{E_r{}^*/E^*}{\sigma^*/\sigma_{0.7}{}^*} = \frac{0.00548}{0.00760} = 0.721$$

$$\sigma^*/\sigma_{0.7}{}^* = 0.898$$

$$\sigma^* = 57{,}000 \times 0.898 = 51{,}200 \text{ lbs. per sq.in.}$$

which happens to be only slightly larger than the estimated buckling stress for the first case.

It should be mentioned that the above procedure is just one of several ways of correcting buckling stress for changes in properties, all of which are based on the assumption of an affine relationship between the stress-strain curves. Karol outlines a convenient procedure of this type in reference 19 and actually gives charts of correction factors for Alclad 24S-T and Alclad 75S-T aluminum-alloy sheet.

Classification of Stress-Strain Curves

As mentioned above, the primary purpose of the dimensionless plotting is to reduce the stress-strain curves to a form in which the effects of variations in Young's modulus and in yield strength are eliminated, so that only the deviations from affinity—that is, the changes in shape of the stress-strain curve—remain.

This suggests a classification of stress-strain curves by shapes that may vary between the extremes, illustrated in Fig. 13, of gradual curvature beginning at low stresses, and of practically no curvature up to the yield strength. An examination of stress-strain curves of aluminum-alloy and of alloy-steel sheets with widely different shapes, given in reference 1, shows that most of them can be described by Osgood's formula:[17]

$$\epsilon = (\sigma/E) + K(\sigma/E)^n \qquad (2)$$

in which K and n are constants that are adjusted to give an optimum fit to the stress-strain curve. The meaning of these constants is made clear by writing Eq. (2) in terms of the dimensionless variables $\sigma/\sigma_{0.7}$, $\epsilon E/\sigma_{0.7}$. It is shown in reference 17 that this leads to

$$\epsilon E/\sigma_{0.7} = (\sigma/\sigma_{0.7}) + {}^3/_7(\sigma/\sigma_{0.7})^n \qquad (3)$$

Comparison of Eq. (3) with Eq. (2) shows that

$$K = {}^3/_7\,(E/\sigma_{0.7})^{n-1}$$

i.e., K depends on the Young's modulus and the secant yield strength of the material. Only the shape parameter n remains in the dimensionless Eq. (3). Fig. 14 shows the effect of variations in n on the shape of the stress-strain curve.

The applicability of Eqs. (2) and (3) may be tested by plotting the stress-deviation curve (deviation $= \epsilon - \sigma/E$) on a log-log scale. This should lead to a straight line if Osgood's formula holds, since

$$\log [\epsilon - (\sigma/E)] = \log K + n \log \sigma/E \qquad (4)$$

The values of K and of n may be determined from the ordinate at a given abscissa and from the slope of this straight line.

Approximate values of n can be obtained quickly, for stress-strain curves described by Osgood's formula, by determining the ratio of two secant yield strengths as explained in reference 17. Fig. 15 shows the relation

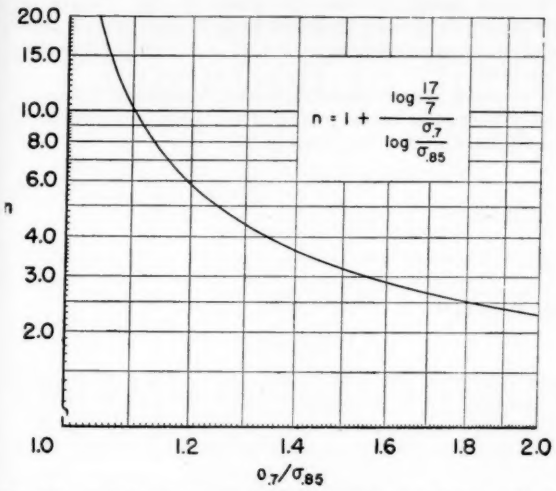

FIG. 15. Relation between shape parameter n and the ratio of secant yield strengths, $\sigma_{0.7}/\sigma_{0.85}$.

between n and $\sigma_{0.7}/\sigma_{0.85}$, where $\sigma_{0.85}$ denotes the secant yield strength for a line with slope $0.85E$.

A comparison of measured stress-strain and tangent-modulus curves with curves obtained from Osgood's formula[17] shows that the formula gives an adequate and simple description for many stress-strain curves. It follows that n is a convenient parameter for classifying such stress-strain curves.

Osgood's formula is used in reference 20 to derive a nomogram for estimating the effect of changes in Young's modulus and in yield strength on the buckling load of a structure. This provides a particularly rapid solution for materials with affinely related stress-strain curves described by Osgood's formula.

It should be pointed out that the formula will not be adequate for clad materials for which the stress-strain curves show a change in slope when the cladding yields at low stress, followed by a linear portion up to the region in which the core begins to yield. In such cases a useful analytical description of the stress-strain curve can sometimes be obtained by dividing the stress-strain curve into two portions and describing each portion independently by Eq. (2).

CONCLUSIONS

Accurate values of the compressive stress-strain curve up to stresses of 60,000 lbs. per sq.in. may be obtained on sheet with a thickness not less than 0.02 in. by any one of the following methods: pack method, Montgomery-Templin method, N.B.S. solid-guide method, N.A.C.A. grooved-guide method, ARMCO solid-guide method, and A.T.S.C. solid-guide method.

The stress-strain curves for much stronger materials and for thinner gages may be obtained by several of these methods if proper attention is given to the preparation of the specimen and to details of the testing procedure.

The effects of small variations in Young's modulus and in yield strength on the stress-strain curve and on the buckling stress in the plastic range can be estimated frequently from dimensionless curves of stress vs. strain and of tangent modulus and reduced modulus vs. stress.

A large class of stress-strain curves, which, however, does not include all clad aluminum alloys, can be described by a simple formula proposed by Osgood which requires a knowledge of only one parameter in addition to Young's modulus and a secant yield strength. A convenient set of three such parameters is Young's modulus and the secant yield strengths corresponding to slopes of $0.7E$ and $0.85E$.

REFERENCES

[1] Aitchison, C. S., and Miller, James A., *Tensile and Pack Compressive Tests of Some Sheets of Aluminum Alloy, 1025 Carbon Steel, and Chromium-Nickel Steel*, N.A.C.A. T.N. No. 840, 1942.

[2] Aitchison, C. S., and Miller, James A., *Tensile and Compressive Tests of Magnesium Alloy J-1 Sheet*, N.A.C.A. T.N. No. 913, 1943.

[3] Lundquist, Eugene E., and Schwartz, Edward B., *The Critical Compression Load for a Universal Testing Machine When the Specimen is Loaded Through Knife Edges*, N.A.C.A. T.N. No. 860, 1942.

[4] Aitchison, C. S., and Miller, James A., *A Subpress for Compressive Tests*, N.A.C.A. T.N. No. 912, 1943.

[5] Aitchison, C. S., and Tuckerman, L. B., *The "Pack" Method for Compressive Tests of Thin Specimens of Materials Used in Thin-Wall Structures*, N.A.C.A. Report No. 649, 1939.

[6] Aitchison, C. S., *Extension of Pack Method for Compressive Tests, N.A.C.A. T.N.* No. 789, 1940.

[7] Paul, D. A., Howell, F. M., and Grieshaber, H. E., *Comparison of Stress-Strain Curves Obtained by Single-Thickness and Pack Methods*, N.A.C.A. T.N. No. 819, 1941.

[8] Kotanchik, Joseph N., Woods, Walter, and Weinberger, Robert A., *Investigation of Methods of Supporting Single-Thickness Specimens in a Fixture for Determination of Compressive Stress-Strain Curves*, N.A.C.A. RB No. L5E15, 1945.

[9] *Compressive Tests of Sheet Metal with Solid Guides for Lateral Support*, Bureau of Aeronautics, Navy Department, Structures Memorandum No. 10, November 10, 1942.

[10] Miller, James A., *Discussion of Paper by Georges Welter*, entitled "Micro-Deformation Under Tension and Compression Loads of Thin Aluminum Alloy Sheets for Aircraft Construction," Proceedings, A.S.T.M., Vol. 44, pp. 683–685, 1944.

[11] Miller, James A., *A Fixture for Compressive Tests of Thin Sheet Metal Between Lubricated Steel Guides*, N.A.C.A. T.N. No. 1022, 1946.

[12] Jackman, K. R., *Improved Methods for Determining the Compression Properties of Sheet Metal*, Automotive & Aviation Industries, Vol. 90, No. 11, pp. 36–38, 82, June 1, 1944.

[13] Welter, Georges, *Micro-Deformation Under Tension and Compression Loads of Thin Aluminum Alloy Sheets for Aircraft Construction*, Proceedings, A.S.T.M., Vol. 44, pp. 665–681, 1944.

[14] LaTour, Harry, and Wolford, Don S., *Single-Strip Compression Test for Sheet Materials*, Proceedings, A.S.T.M., Vol. 45, pp. 671–688, 1945.

[15] Van den Broek, J. A., *Evaluation of Aeroplane Metals*, The Engineering Journal, Canada, July, 1945.

(*Continued on next page*)

[16] Madden, Baxter C., Jr., *A Method of Testing Thin Sheet Material in Compression*, Army Air Forces Technical Report No. 5311, October 22, 1945.

[17] Ramberg, Walter, and Osgood, William R., *Description of Stress-Strain Curves by Three Parameters*, N.A.C.A. T.N. No. 902, 1943.

[18] Timoshenko, S., *Theory of Elastic Stability*, 1st Ed., pp. 384–390; McGraw-Hill Book Company, Inc., New York, 1936.

[19] Karol, Jacob, *Correction of Aluminum-Alloy Compressive Test Results for Material Properties Using Reduced Moduli*, Journal of the Aeronautical Sciences, Vol. 12, No. 3, pp. 305–310, 328, July, 1945.

[20] Ramberg, Walter, and Levy, Samuel, *Instability of Extrusions Under Compressive Loads*, Journal of the Aeronautical Sciences, Vol. 12, No. 4, pp. 485–498, October, 1945.

Letter to the Editor

Dear Sir:

The following is with reference to Alexander Flax's letter of July 8, 1946, appearing in the October, 1946, JOURNAL and commenting on my paper, "Notes on the Design of Pressurized Aircraft" (June, 1946, issue of the JOURNAL).

(1) Mr. Flax's comments on the assumptions concerning the altitude variation of load factor do not agree with some of the basic philosophy underlying aircraft design criteria—namely:

(a) The maximum speed at which aircraft are flown is legally limited by placard and not by the terminal velocity that the airplane may attain in a dive. Such placards are used to limit maximum horizontal speed, as well as diving speed; hence, aerodynamics and engine performance do not form the complete basis for load factor determination. It should also be realized that discussions of load factors cannot be conducted purely on an academic basis, since in the case of the maneuver factors for commercial aircraft the load factor attained depends mainly on the discretion of the pilot. There is probably no transport aircraft in existence today which cannot be torn apart in the air in the hands of a reckless pilot.

(b) The maneuver factor prescribed by Civil Air Regulations for large aircraft is generally smaller than the gust factor and, consequently, is secondary for design purposes. In this regard the arbitrary load factor reduction formula suggested by the writer is conservative, since it applies only a density correction on the gust factor and does not include the effects of the actual reduction of effective gust velocity (see discussion in paper on gust loads).

(2) Mr. Flax's comments on hoop tension are interesting, but from a purely academic point of view. He has conveniently ignored the writer's comments (page 303 of June, 1946, JOURNAL) on skin continuity. Perhaps Mr. Flax's comments would be legitimate for the design of a pressurized tail cone without cutouts and without skin seams. Further, his statements based on equation 4.16 of von Kármán and Biot's book seem to be an extrapolation on the von Kármán and Biot conclusion which is: "Therefore, to reduce the stress in a *long* pipe materially by a series of stiffener rings the spacing must be of the order of magnitude of $2l = 2\sqrt{rt}/\sqrt[4]{3}$."

(3) In reply to Mr. Flax's comment No. 3, "Table 1 and Fig. 2 of the paper for the stress coefficients of a rectangular membrane appear to be in error," the footnote on page 303 of the writer's paper, as well as Fig. 1, shows that the dimensions (*a*) and (*b*) are twice those used by Timoshenko. A simple numerical computation will show that the coefficients that he has listed are altered considerably by the fact that Timoshenko's a is $1/2$ that used by the writer*—Mr. Flax has also omitted any statements regarding the value of Poisson's ratio used in his computations.

(4) Regarding comment No. 4, the writer is well aware of the literature on the effects of internal pressure on buckling of skin under shear and compressive loads. It is pointed out, however, that most of the literature is "restricted" and therefore should not be quoted.

(5) Mr. Flax's comment Nos. 5 and 6 seem to have little bearing on the illustrative example presented in the writer's paper, since Mr. Flax has not seen fit to present a comparative set of figures demonstrating how the "critical structural altitude" is altered by the assumptions he proposes. It is agreed, however, that a great deal of additional work can and should be done to determine effects of pressurization on such items as stringer loads introduced by tension field and similar buckling formations. The writer's paper was written as an introduction to the problem and was not intended to be a comprehensive treatise.

D. O. DOMMASCH
Bell Aircraft Corporation

* For comparison purposes Mr. Flax should have multiplied his coefficients by $2^{2/3} = 1.588$.

Additional Developments of Greene's Equation to the Study of Compressible Airflow

GEORGE L. SHUE*

Consolidated Vultee Aircraft Corporation

SUMMARY

Extension of Greene's "Attenuation Method for Compressible Flow Systems" to include the supercritical region leads to an empirical interpretation of supercritical conditions. The correction that is then applied to the airfoil incompressible pressure coefficient predicts supercritical flow conditions on the downstream side of the peak negative incompressible pressure coefficient. The calculated position of the shock that accompanies the return to subsonic conditions is shown to progress downstream with increasing Mach Number. With a suitable choice of a polytropic flow process the calculated chordwise pressure distribution checks with high-speed test data and this automatically brings the lift and pitching moment values into agreement with test results. The energy loss in the shock yields a reasonable means for calculating the increase in drag at high speeds. Each surface of the airfoil and each item in the airplane configuration are treated separately in estimating the drag.

INTRODUCTION

THE PROBLEM of accurately predicting the behavior of an airfoil at high speeds is one of the serious problems confronting the aerodynamics engineer today. Since the density of air is variable with the temperature and pressure, it invalidates incompressible theory at present-day speeds. The effects of compressibility on the forces produced by airfoils at high speeds must be known if accurate predictions of performance are to be made. The moments of these forces are important factors in stability and control problems. The total air load and its distribution are extremely important to the structures engineer.

In the light of our present knowledge, the most practical way of accounting for compressibility is to express the relationship of the pressure coefficients for compressible and incompressible flow systems in some rational manner. The wealth of incompressible pressure distribution data and theory are then useful. The corrections that are applied to pressure coefficients reflect in forces and moments upon integration of the corrected pressure distributions. If it be remembered that the fundamental corrections are applied to pressure, then more reliable corrections, when they become available, will be applied to all aerodynamic entities.

Presented at the Aerodynamics Session, Fourteenth Annual Meeting, I.A.S., New York, January 29–31, 1946.

* Aerodynamics Engineer, San Diego Division. Now Chief, Aerodynamics Subdivision, Naval Ordnance Laboratory.

NOTATION

a_0 = slope of lift curve for section (low Mach Number)
a = speed of sound
A = aspect ratio
A_1 = $(\sqrt{1 - C_{P0}} - 1)/(1 - C_{P0})$
b = span
B^2 = $M^2 + [2/(n-1)](1 - F^{n-1})$
c = chord
C_D = drag coefficient
C_L = lift coefficient
C_M = pitching moment coefficient
C_p = pressure coefficient $\Delta p/q$
F = $(1 + {}^1/_2 nM^2 C_{PM})^{1/n}$ = density ratio
K = $C_{D\,cr.}/C_{D0}$
M = Mach Number
$M_{cr.}$ = critical free stream Mach Number
m = mass of air affected per sec.
n = polytropic index
KE = kinetic energy per sec.
r = radius
S = wing area
ρ = density
η = $m/\rho a MS$

Subscripts

0 = incompressible
M = compressible
1 = limiting local conditions
2 = local conditions just before shock
3 = local conditions just after shock
4 = local conditions
none = free stream conditions

GLAUERT CORRECTION

The commonly used correction for compressibility is that of Glauert $\sqrt{1 - M^2}$ (reference 1). It was developed for application to two-dimensional pressure data. However, it is found that the same factor appears in the forces and moments. For this reason and also because it is easy to use, the Glauert factor is often applied in places where it is not sufficiently accurate or where it does not apply. For example, the slope of the lift curve for both the airfoil section and for a complete wing are almost always corrected by Glauert's factor. If the wing lift curve slope is properly corrected by application of the factor to section data the resulting slope is given by

$$\frac{dC_L}{d\alpha} = \frac{a_0}{\sqrt{1 - M^2} + (a_0/\pi A)}$$

Kármán-Tsien Correction

The Kármán-Tsien correction[2] is becoming more widely used and gives better agreement with experiment than does the Glauert correction. It applies to pressure distribution for the section and care should be exercised when it is applied to wings of finite aspect ratio. To obtain the corrected force coefficients one must integrate the corrected pressure distribution at each Mach Number selected. It gives excellent agreement with experiment at subcritical Mach Numbers.

$$C_{pM} = C_{p0} \Big/ \left[\sqrt{1 - M^2} \left(\frac{M^2}{1 + \sqrt{1 - M^2}} \right) \frac{C_{p0}}{2} \right]$$

Greene's Attenuation Method

The attenuation method of Greene[3] is superior to either of the previously mentioned corrections. The author's reasons for believing that Greene's equation is the best available are:

(1) It is sufficiently accurate for most engineering purposes.

(2) It permits the use of any desired polytropic process including a variable index.

(3) It is easily adapted to the correction of pressure distribution for bodies of revolution.

(4) It gives an empirical interpretation for pressure distribution at supercritical Mach Numbers.

(5) By judicious choice of the polytropic index it can be made to agree with experiment.

The author's interpretation of the attenuation method and its practical applications are the principal subject matter of this paper. Agreement with test data in the supercritical region is the prime consideration.

Interpretation

The word "critical" is used with several possible meanings. The author suggests that "critical" be retained as a generally descriptive term and that "sonic" be used to describe conditions in which the local speed of sound is reached. Similarly, "limiting" is used to describe conditions at which shock losses begin to appear, and "absolute" describes the minimum possible static pressure (theoretically zero) conditions. Then sonic Mach Number would mean the free stream Mach Number at which the speed of sound is reached locally, and limiting Mach Number would designate the Mach Number above which shock losses occur. In the consideration of drag, critical usually indicates the Mach Number at which the rise in drag begins.

The equation for Greene's attenuation method may be written

$$dC_{p0}/dC_{pM} = M(FB - M)/A_1 FB^2 \qquad (1)$$

The local Mach Number is given by

$$M_4 = B/F^{(n-1)/2} \qquad (2)$$

When $M_4 = 0$ is solved for C_{pM} it yields the well-known equation for the pressure coefficient at the stagnation point

$$C_{pM} = \frac{2}{nM^2} \left\{ \left[1 + (n - 1)/2)M^2 \right]^{n/(n-1)} - 1 \right\} \qquad (3)$$

When the local speed is equal to the free stream speed it is found that C_{pM} is zero by definition. When the local Mach Number is unity, Eq. (2) yields

$$C_{pM}(\text{sonic}) = \frac{2}{nM^2} \left\{ \left[\frac{2 + (n-1)M^2}{n+1} \right]^{n/(n-1)} - 1 \right\} \qquad (4)$$

The limiting conditions without shock losses are defined by $FB = M$. It can be shown that the local stream tube cross section is the same as in the free stream.

The values for C_{pM} for this case at selected Mach Numbers are found in the process of integration (see Fig. 4a, reference 3) or by Eq. (25) of reference 3. When the density ratio is zero the absolute conditions are indicated and

$$C_{pM}(\text{abs.}) = -2/nM^2 \qquad (5)$$

Numerical integration of Eq. (1) with a variable polytropic flow process is accomplished easily by the difference table method.[4] The author's interpretation requires that the curves be plotted with C_{p0} and C_{pM} as axes. Fig. 1 illustrates typical curves. The poly

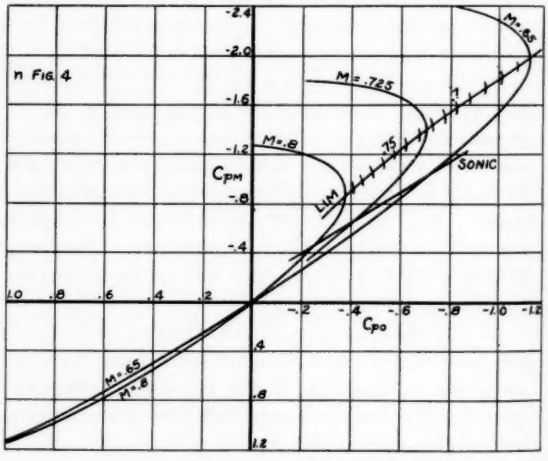

FIG. 1. C_{pm} vs. C_{p0}. Attenuation method.

tropic index that brings the theory into agreement with experiment varies with the type of airfoil. The NACA 4412 airfoil appears to check when $n = 1.7 - 0.3\ C_{pM}$. Low-drag sections appear to require a variation of n similar to that illustrated in Fig. 4. It is probable that the relative humidity of the wind tunnel is an important factor in the type of polytropic process required. Condensation shocks cause a reduction in the peak negative C_{pM} observed as compared to theory.

Numerical Applications

The curves in Figs. 2a and 2b are typical results from high-speed wind-tunnel data. It is significant that the curves deviate from the origin by increasing amounts as the Mach Number increases, and that following the shock the curve passes close to the origin. The local speed equal to the free stream speed occurs at different chordwise stations as the Mach Number is changed.

The author is aware of the observation that in the supersonic region the airfoil shape is of fundamental importance and that C_{pM} in this region is not necessarily a function of C_{p0}. However, C_{p0} is a function of the airfoil shape.

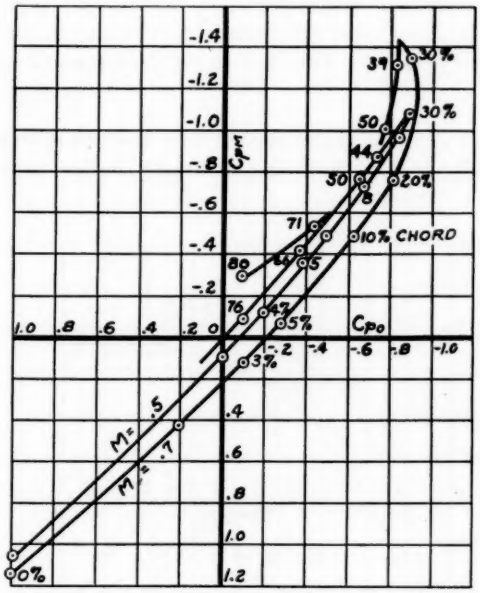

FIG. 2a. C_{pm} vs. C_{p0}. Test data.

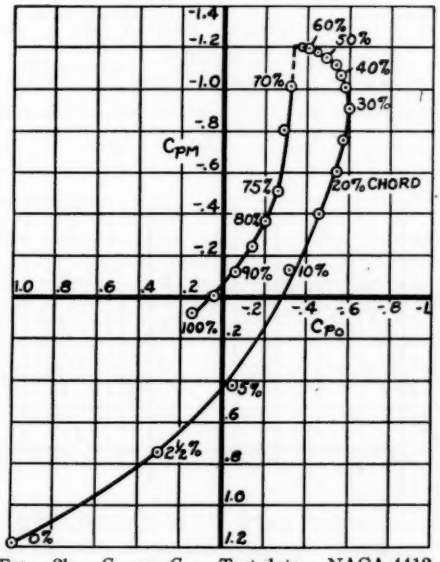

FIG. 2b. C_{pm} vs. C_{p0}. Test data. NACA 4412. $\alpha = 0$; $M = 0.756$; reference 5, Fig. 3.

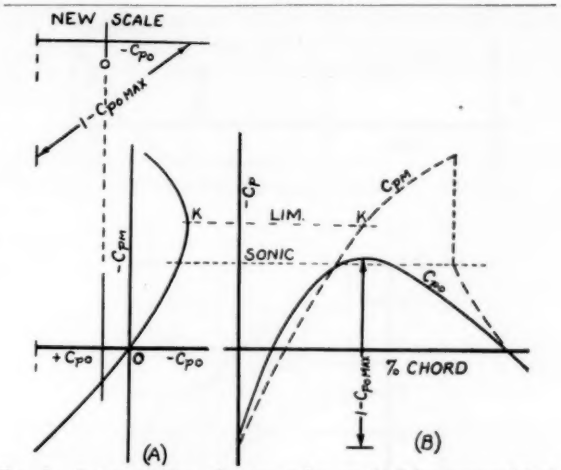

FIG. 3. Interpretation of attenuation method for supercritical conditions.

The author's empirical interpretation for supercritical conditions is illustrated in Fig. 3. The curve on the left (A) C_{pM} vs. C_{p0} is obtained by integration of Eq. (1). The solid curve on the right (B) is the given incompressible pressure distribution. A new scale for C_{p0} is made for the curve on the left so that the required maximum negative C_{p0} matches the limiting conditions. This scale is illustrated above the curve. Near the trailing edge the values of C_{pM} which correspond to each C_{p0} are found for the subsonic region using the regular C_{p0} scale. Beginning at the stagnation point the chordwise flow is followed, finding the values of C_{pM} for each C_{p0} on the new scale. When C_{p0} passes the peak negative point the larger negative value of C_{pM} is used. The shock is drawn at the chordwise station so that it terminates on the local sonic speed.

If the shock is severe, the energy losses raise the temperature of the air and reduce the effective free stream Mach Number. In cases where severe shocks are encountered the region following the shock is revised, using a reduction of approximately 0.03 in the free stream Mach Number. This moves the shock forward slightly to the new C_{pM} (sonic) position.

Adiabatic vs. Polytropic Flow

An adiabatic flow process gives unsatisfactory agreement with experience. This is true for both the subcritical and supercritical cases. Since the Kármán-Tsien correction gives excellent agreement with test data in the subsonic region, a value of -1 is selected for n to apply where the flow is subsonic. (When -1 is used for n, Greene's equation is substantially equivalent to Kármán-Tsien.) In the region close to the stagnation point an adiabatic ($n = 1.4$) process is indicated since there is no way to change the entropy.

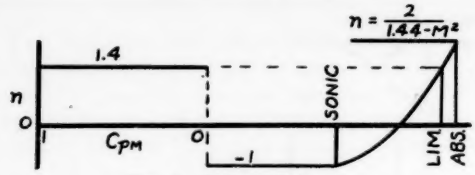

FIG. 4. Polytropic index.

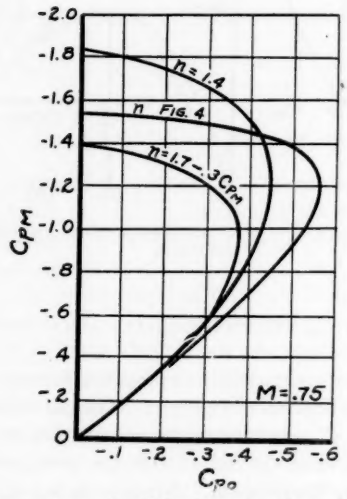

FIG. 5. Comparison of adiabatic and polytropic processes.

By checking the peak negative C_{pM} from all available data, the envelope was assumed to represent the practical values of C_{pM} (abs.). The corresponding values for n at test Mach Numbers fell on a smooth curve which could be represented by

$$n = -\frac{2}{M^2 C_{pM}(\text{abs.})} = \frac{2}{1.44 - M^2} \qquad (6)$$

Fig. 4 illustrates the currently recommended values of n for low-drag sections. A value of 1.4 is always used for n at the limiting conditions. A comparison of the adiabatic and variable polytropic curves is shown in Fig. 5.

Comparsion with Test Results

The curves in Fig. 6 show a comparison of the predicted pressure distribution for a 4412 section and the measured pressure distribution from reference 5. Fig. 7 illustrates the comparison of the calculated lift and pitching moment with experiment at high speed. When the pressure peak is near the leading edge the estimated pressure distribution for supercritical flow conditions does not agree with test data. It appears probable that local separation caused by centrifugal force is the explanation. The conditions at which the normal pressure gradient just balances the centrifugal force are expressed by

$$dC_p/dr = 2\rho_4 V_4^2/r\rho V^2 \qquad (7)$$

Correction of Pressure on Three-Dimensional Bodies

Greene (reference 3, Eq. 27) has adapted his equation to bodies of revolution. Unfortunately, this adaptation requires a new integration for each fineness ratio. In most engineering work the accuracy required and the time available do not indicate such refinements. Frequently, the bodies used are more nearly ellipsoids than bodies of revolution. An approximate correction can be obtained by using an appropriate fraction of the two-dimensional correction

$$C_{pM} = \frac{b}{a+b} C_{p0} + \frac{a}{a+b} C_{pM}\ (2\text{-}dim.) \qquad (8)$$

where a and b are appropriate major and minor diameters. If a body of revolution is corrected in this manner

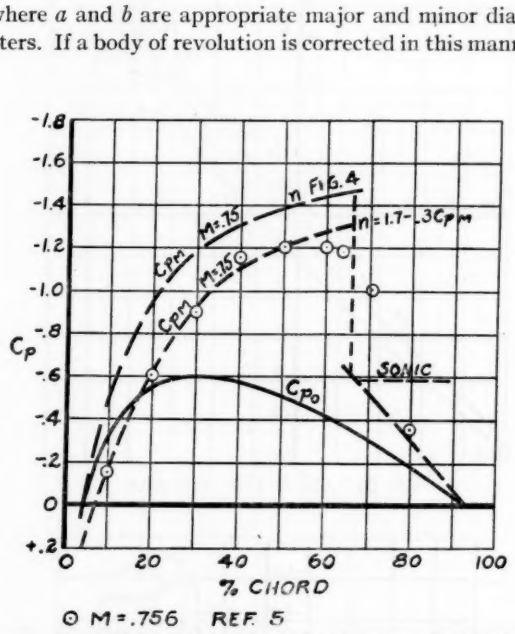

FIG. 6. Comparison of test and calculated pressure distribution. NACA 4412. $\alpha = -2^\circ$.

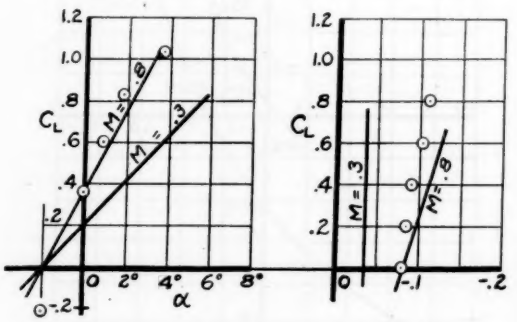

FIG. 7. Calculated and measured airfoil characteristics at high speed.

it amounts to using one-half of the two-dimensional correction.

Estimation of Drag

The drag that is added because of the shock can be estimated by the method presented below. For drag estimates each of the two surfaces of the airfoil should be separately calculated, using the appropriate critical Mach Numbers. In this case "critical" refers to "limiting Mach Number" or the Mach Number at which the drag begins to rise sharply. The drag coefficient for a complete airplane can be found by use of the same formula by calculating the contribution of each component of the airplane separately. Since each item of the airplane configuration is separately calculated, it is easy to estimate the effect of any particular item on high-speed performance.

Formula for Drag

The kinetic energy change in the shock is assumed to be represented by the increase in drag. Then

$$V\Delta D = KE_2 - KE_3 = \Delta C_D S {}^1/_2\rho a^3 M^3 = {}^1/_2 m(a_2^2M_2^2 - a_3^2M_3^2) \quad (9)$$

$$\Delta C_D = \frac{KE_2 - KE_3}{S {}^1/_2\rho a^3 M^3} = \frac{{}^1/_2 m(a_2^2M_2^2 - a_3^2M_3^2)}{S {}^1/_2\rho a^2 M^2 aM} = \frac{m}{\rho aMS}\frac{a_2^2M_2^2 - a_3^2M_3^2}{a^2M^2} \quad (10)$$

Borrowing an idea from Glauert, it is assumed that the square of the limiting velocity is equal to the product of the velocities immediately before and after the shock.

$$a_1^2M_1^2 = a_2M_2a_3M_3 \quad (11)$$

In order to have symmetry in the equation, let

$$a_2M_2 = (M/M_{cr.})a_1M_1 \quad (12)$$

$$a_3M_3 = (M_{cr.}/M)a_1M_1 \quad (13)$$

Then the increase in drag coefficient becomes

$$\Delta C_D = \frac{m}{\rho aMS}\frac{a_1^2M_1^2}{a^2M^2}\left[\left(\frac{M}{M_{cr.}}\right)^2 - \left(\frac{M_{cr.}}{M}\right)^2\right] \quad (14)$$

Now $m/\rho aM$ is the cross-section area of stream tubes (in the free stream) which pass through the shock zone. For a wing, this area is some fraction, f, of the product of the chord and the span, or

$$m/\rho aMS = fcb/\rho aMcb = \eta \quad (15)$$

The drag coefficient at Mach Number then may be expressed in terms of the low-speed drag coefficient.

$$C_{DM} = C_{D0}K\left[1 + \eta\frac{a_1^2M_1^2}{a^2M^2}\left(\frac{M^2}{M_{cr.}^2} - \frac{M_{cr.}^2}{M^2}\right)\right] = C_{D0}K\left[1 + \eta\frac{2 + (n-1)M^2}{2 + (n-1)M_1^2}\frac{M_1^2}{M^2}\times\left(\frac{M^2}{M_{cr.}^2} - \frac{M_{cr.}^2}{M^2}\right)\right] \quad (16)$$

The values of K and η are found from high-speed tests and are approximately

$$K = 1.20$$

$$\eta = 1.0M^2/M_{cr.}^2$$

Substitution of these values in Eq. (16) gives:

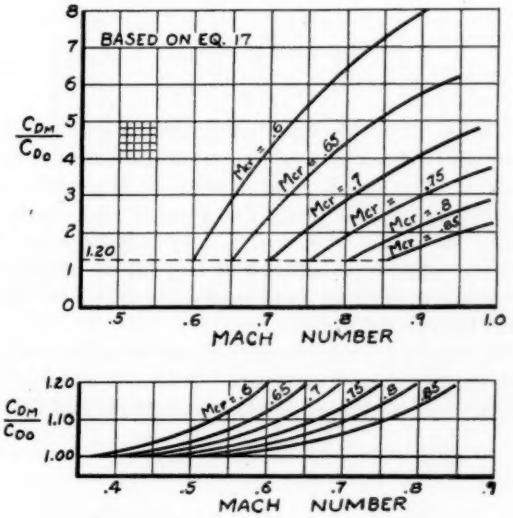

Fig. 8. Drag correction—high speed.

Table 1
Drag of Assumed Airplane

Part	$M_{cr.}$	C_D $M = 0$	$M = 0.6$	$M = 0.65$	$M = 0.7$	$M = 0.75$	$M = 0.8$	$M = 0.85$	$M = 0.9$
Wing U.S. (inner)	0.65	0.0025	0.0028	0.0030	0.0061	0.0088	0.0110	0.0128	0.0144
Wing U.S. (outer)	0.68	0.0020	0.0022	0.0023	0.0032	0.0051	0.0066	0.0081	0.0091
Wing L.S. (inner)	0.70	0.0025	0.0027	0.0028	0.0030	0.0053	0.0072	0.0088	0.0103
Wing L.S. (outer)	0.70	0.0020	0.0022	0.0023	0.0024	0.0043	0.0058	0.0070	0.0082
Fuselage	0.75	0.0045	0.0047	0.0049	0.0051	0.0054	0.0085	0.0112	0.0135
Tail	0.70	0.0022	0.0024	0.0025	0.0026	0.0047	0.0064	0.0077	0.0090
Power Plant	0.65	0.0015	0.0017	0.0018	0.0037	0.0053	0.0066	0.0077	0.0087
Misc.	0.60	0.0010	0.0012	0.0028	0.0043	0.0054	0.0064	0.0072	0.0079
Total	...	0.0182	0.0199	0.0224	0.0304	0.0443	0.0585	0.0765	0.0811

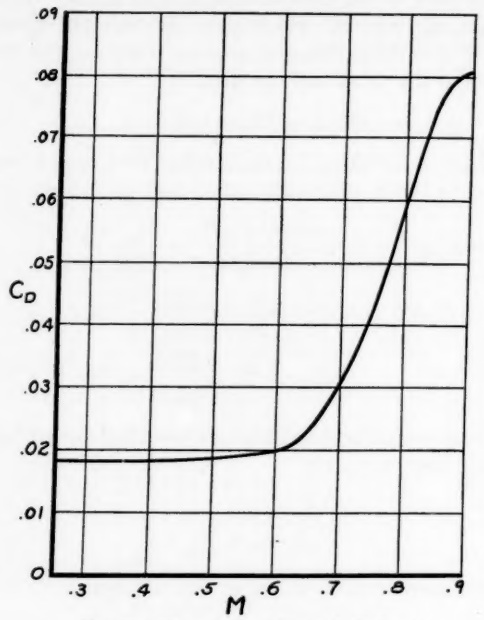

FIG. 9. C_D vs. M. Assumed airplane.

$$\frac{C_{DM}}{C_{D0}} = 1.20\left[1 + \frac{5 + M^2}{5 + M_1^2}\frac{M_1^2}{M_{cr.}^2}\left(\frac{M^2}{M_{cr.}^2} - \frac{M_{cr.}^2}{M^2}\right)\right] \quad (17)$$

Eq. (17) is valid only when the critical Mach Number is exceeded. It is observed that no drag increase occurs below $M/M_{cr.} = 0.6$. Fig. 8 contains the results of Eq. (17) in a usable form. For more accurate evaluation of the values of K and η, a systematic series of tests on symmetrical sections at zero lift are required. The critical speed for both upper and lower surfaces would then be the same.

The drag of a complete airplane can be estimated by applying Eq. (17) to each part. Table 1 illustrates an example for an assumed airplane at zero lift and Fig. 9 represents the final result. The critical Mach Number for each surface of the wing is required at each lift coefficient. The induced drag is assumed to be given by $C_L^2/\pi A$ at all Mach Numbers.

Conclusions

(1) In the absence of high-speed wind-tunnel tests Greene's attenuation method may be used to estimate pressure distribution at supercritical Mach Numbers.

(2) By checking out the polytropic index selected against test data for similar sections, the attenuation method is made extremely useful for obtaining details not included in the test data.

(3) Reasonably accurate preliminary estimates of performance, air loads, and weights for new designs can be made from data, including corrections for compressibility, by the attenuation method.

(4) The calculation of the drag for each item separately is useful for estimating the effects of changes in airplane configuration on the high-speed performance.

References

[1] Glauert, H., *The Effect of Compressibility on the Lift of an Aerofoil*, Royal Soc., Vol. 118, p. 113, 1927.

[2] von Kármán, Th., *Compressibility Effects on Aerodynamics*, Journal of the Aeronautical Sciences, Vol. 8, No. 9, pp. 337–356, July, 1941.

[3] Greene, Leonard Michael, *The Attenuation Method for Compressible Flow Systems*, Journal of the Aeronautical Sciences, Vol. 12, No. 3, pp. 329–338, July, 1945.

[4] Shue, George L., *Simplified Numerical Integration for Design Engineers*, Aviation, p. 149, Jan.-Feb., 1945.

[5] Stack, John, Lindsey, W. F., and Littell, Robert E., *The Compressibility Burble and the Effect of Compressibility on Pressures and Forces Acting on an Airfoil*, N.A.C.A. T.R. No. 646, 1938.

[6] Shue, George L., *On Compressibility*, Report No. ZA-096, Consolidated Vultee Aircraft Corporation, San Diego, Calif., Jan. 1, 1944, Addendum 1, March 1, 1944.

Tests on Elbows of a Special Design

JOHN J. HARPER*

Georgia School of Technology

SUMMARY

This paper presents the results of a series of tests on rectangular elbows of the type proposed by Szczeniowski.[1] Six elbows were tested, including one conventional guide vane elbow designed in accordance with the recommendations in *R. & M. No. 1773*.[2] Four of the special elbows had an aspect ratio (A.R.) of 0.67, while the fifth had an A.R. of 1.5.

The results show that under certain design conditions the special elbows show fewer losses than do conventional elbows with guide vanes. Increasing the aspect ratio of the elbow reduces the losses.

INTRODUCTION

THROUGH THE USE of special elbows without guide vanes, a reduction of losses in many applications may be possible. This type elbow might be used to advantage on the carburetor air intake of airplane engines, as there would be no guide vanes to ice up. The manufacture of these special elbows should be relatively easy. It is also possible that elbows of this type could be extended to wind tunnels, where elimination of corner guide vanes would mean a saving in power required.

In view of these possibilities, a test program was instituted consisting of velocity surveys on five of the rectangular two-dimensional elbows and one conventional elbow with guide vanes. All of the above were 90° bends.

THEORY

The mathematical equations for the streamlines of these elbows were developed by Szczeniowski[1] from perfect fluid theory as follows. The elbows are shaped in such a way as to fulfill the equation of continuity in a two-dimensional flow:

$$\partial^2\psi/\partial x^2 + (\partial^2\psi/\partial y^2) = 0$$

where ψ = constant and is the stream function and where x and y are rectangular coordinates.

For the 90° rectangular elbows considered, Szczeniowski[1] gives the following complex potential fulfilling the equation of continuity:

$$e^{(i+1)(z/a)} = e^{(i+1)(w/au)} + e^{(i-1)(w/au)} \qquad (1)$$

where $z = x + iy$, $i = \sqrt{-1}$, $w = \phi + i\psi$. The symbol ϕ designates the velocity potential; ψ, the stream function; a, any linear parameter; and u, any constant freestream velocity.

It is desired that the total velocity, V, at any point, should not exceed the freestream or boundary value u, or $V \leq u$. Likewise no stream line should have singular points. Solution of Eq. (1) gives

$$\frac{x}{a} = \frac{1}{2}\tan^{-1}\left[\frac{\cot\frac{\psi}{au} + \cot\frac{\phi}{au}\tanh\frac{\phi}{au}}{\cot\frac{\phi}{au}\cot\frac{\psi}{au} - \tanh\frac{\phi}{au}}\right] + \frac{1}{2}\left[-\frac{\psi}{au} + LN\sqrt{2\left(\cosh 2\frac{\phi}{au} + \cos 2\frac{\psi}{au}\right)}\right] \qquad (2)$$

$$\frac{y}{a} = \frac{1}{2}\tan^{-1}\left[\frac{\cot\frac{\psi}{au} + \cot\frac{\phi}{au}\tanh\frac{\phi}{au}}{\cot\frac{\phi}{au}\cot\frac{au}{\psi} - \tanh\frac{\phi}{au}}\right] - \frac{1}{2}\left[-\frac{\psi}{au} + LN\sqrt{2\left(\cosh 2\frac{\phi}{au} + \cos 2\frac{\psi}{au}\right)}\right] \qquad (3)$$

$$\frac{v}{u} = \sqrt{\frac{\cosh 2(\phi/au) + \cos 2(\psi/au)}{\cosh 2(\phi/au) + \sin 2(\psi/au)}} \qquad (4)$$

In the above, ϕ is a variable parameter for an arbitrary streamline ψ, which is a constant. By selecting values of ψ/au and assuming values of ϕ/au, the streamlines can be plotted. The following streamlines composed the walls of the elbows tested (Fig. 1): $\psi/au = 5\pi/12$ and $-\pi/8$, $\psi/au = 5\pi/12$ and $\pi/12$, $\psi/au =$

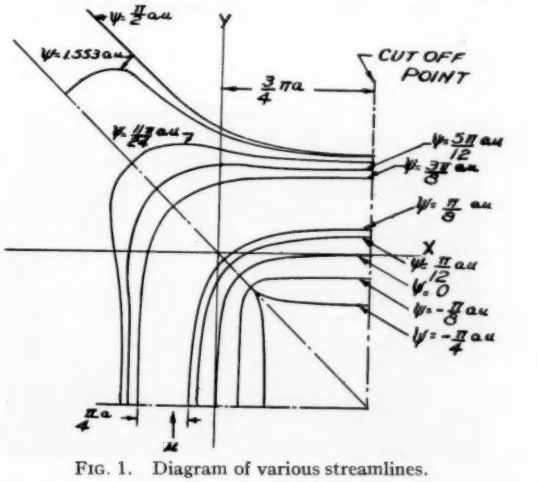

FIG. 1. Diagram of various streamlines.

Received April 22, 1946.

* Instructor, Daniel Guggenheim School of Aeronautics, and Research Faculty Associate, State Engineering Experiment Station.

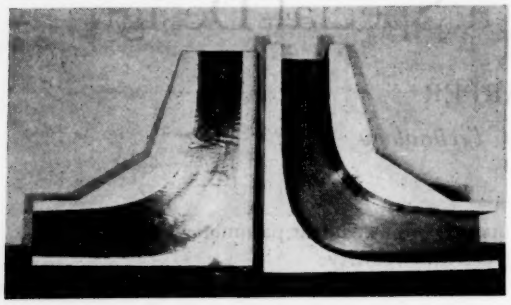

FIG. 2. Photograph of elbow with side removed. (Streamlines 3 /8 and /8; A.R. = 1.5.)

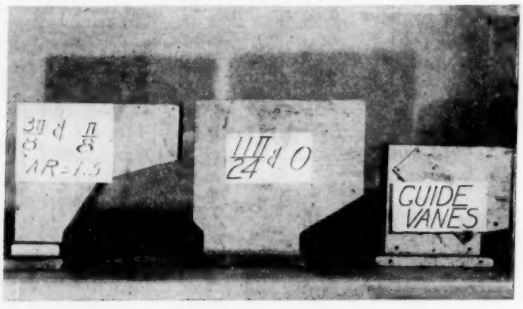

FIG. 3. Photograph of three of elbows tested.

FIG. 4. Photograph of three of elbows tested.

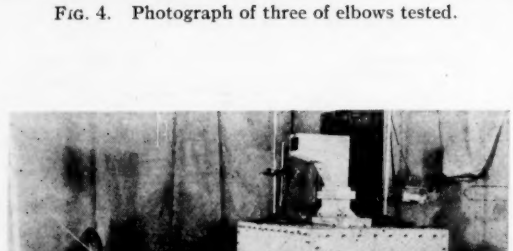

FIG. 5. Photograph of test equipment.

$11\pi/24$ and 0, and $\psi/au = 3\pi/8$ and $\pi/8$. These streamlines were plotted by means of Eqs. (2) and (3). From Eq. (4), the following maximum velocities were found to be: $\psi/au = -\pi/4$, $V_{max.} = \infty$; $\psi/au = -\pi/8$, $V_{max.} = 2.415u$; $\psi/au = 0$, $V_{max.} = 1.414u$; $\psi/au = \pi/12$, $V_{max.} = 1.15u$; and $\psi/au = \pi/8$, $V_{max.} = u$.

Some of the properties of these streamlines as given by Szczeniowski are as follows:

(1) In cutting off the elbows at $^3/_4\pi a$ from the origin (Fig. 1), the error made in the channel width is less than 1 per cent of the width at infinity.

(2) The streamline $\psi/au = \pi/2$ (Fig. 1) is the outermost boundary of the field since it does not carry around the bend before reaching infinity.

(3) The streamline $\psi/au = 3\pi/8$ is the outermost streamline without an inflexion point.

(4) The streamline $\psi/au = \pi/8$ is the innermost streamline along whose length the velocity never exceeds the entrance velocity u.

(5) The streamline $-\pi/4$ is the innermost boundary of the field as the velocity becomes infinite at the 45° point on the streamline.

Apparatus and Tests

Fig. 1 shows the possible streamlines, for all the special elbows, which were plotted from Eqs. (2) and (3). White pine was used to construct the elbows, which had sides of $^1/_4$-in. plywood. The interiors were given two coats of wood filler, rubbed down with steel wool, and finally given four coats of automobile lacquer. Each coat of lacquer was carefully rubbed down with steel wool. Fig. 2 is a photograph of one of the special elbows with one of the sides removed.

All elbows had entrance and exit dimensions of 4.5 by 3 in. Of the five special elbows, four had an A.R. of 0.67, and the fifth had an A.R. of 1.5. The aspect ratio may be defined as the depth of the stream divided by the width of the stream channel (width being the distance between boundary streamlines)—i.e., A.R. = 3/4.5 = 0.67. For the fifth elbow, the reverse is true, or A.R. = 4.5/3 = 1.5. It should be understood that in order to keep the entrance and exit areas of all elbows constant it was necessary to use a different length for each elbow. This means that the value of the linear parameter a, which appears in Eqs. (2) and (3), must be different for each elbow. From Fig. 1 it is seen that the distance between a pair of streamlines is $(\pi/4)a$ and the cutoff point measured from the Y axis is $^3/_4\pi a$. Thus any pair of streamlines used has a certain value of a which is necessarily different from that of any other pair.

The conventional elbow had five aluminum-alloy guide vanes and was designed according to the method recommended by Patterson.[2] Figs. 3 and 4 show the set of six elbows labeled with their corresponding streamlines.

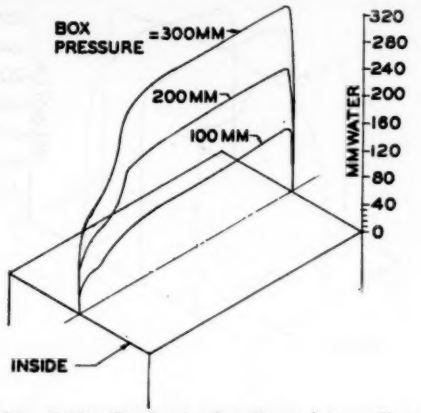

FIG. 6. Lengthwise distribution for elbow of streamlines $11\pi/24$ and 0 at different box pressures.

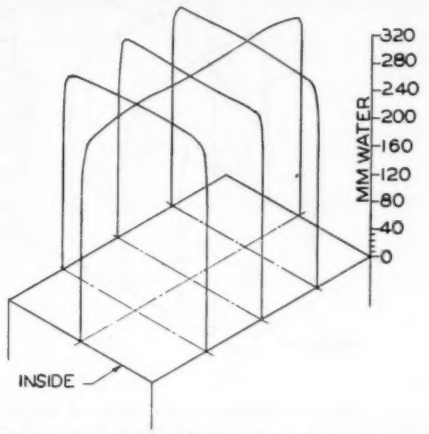

FIG. 7. Velocity distribution for nozzle at box pressure of 300 mm.

The test equipment consisted of a 4 by 4 ft. plywood pressure box fitted with a convergent nozzle having exit dimensions of 4.5 by 3 in. Air was supplied by a 5 hp. centrifugal blower equipped with a throttle valve. A standard pitot tube was used in conjunction with water-filled, reservoir-type manometers. Fig. 5 is a photograph of the test equipment.

In order to ensure good distribution at the elbow entrance, preliminary velocity surveys were made on the nozzle in the plane of exit. One survey was made lengthwise down the centerline of the exit, and others were taken at three equal intervals across the short dimension (3 in.) of the nozzle. These velocity surveys were made at three different box pressures (100, 200, 300 mm. water) to determine the effect of change in velocity on the nozzle distribution. The velocity distributions obtained were all geometrically similar; therefore, the nozzle was considered satisfactory for testing the elbows. The same procedure was followed for one of the elbows, but there was no apparent change in the similarity of the distribution at different box pressures (Fig. 6).

The final pitot surveys were identical for each elbow tested. Static pressure in the box was maintained at 300 mm. water. A total of four surveys on each elbow was made: one down the centerline in the exit plane and three crosswise surveys at equal intervals across the short dimension (3 in.) of the exit.

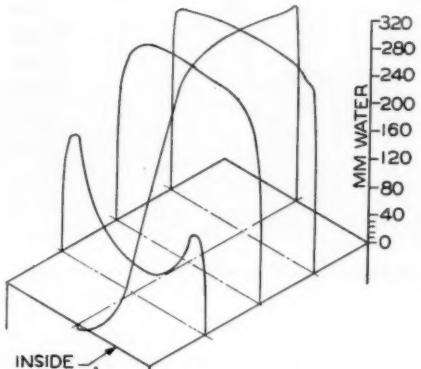

FIG. 8. Velocity distribution for elbow of streamlines $5\pi/12$ and $-\pi/8$.

RESULTS AND DISCUSSION

Figs. 7 through 14 show the velocity distributions obtained with various streamline combinations. These distributions were plotted isometrically, and the inside of the bend was marked in each case.

Since all surveys on the nozzle were made with no bend in place, it cannot be assumed that the nozzle losses or velocity remain unchanged with an elbow on, since the flow resistance is increased and the velocity through the nozzle decreases. Consequently, to get

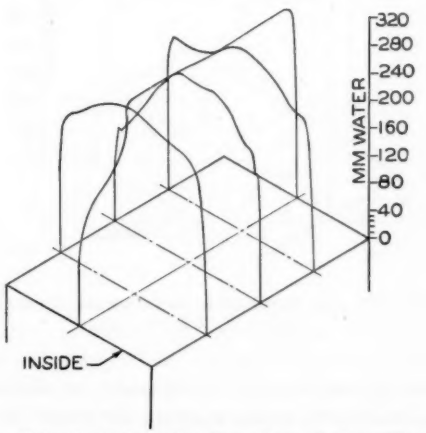

FIG. 9. Velocity distribution for elbow of streamlines $11\pi/24$ and 0.

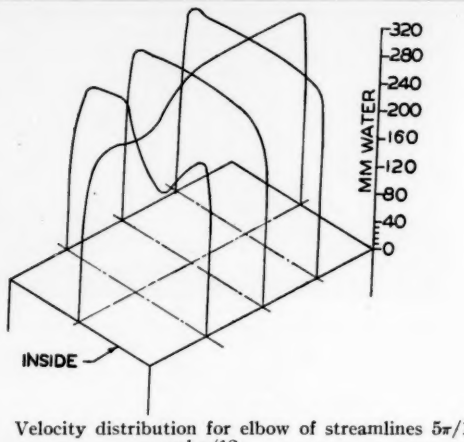

FIG. 10. Velocity distribution for elbow of streamlines $5\pi/12$ and $\pi/12$.

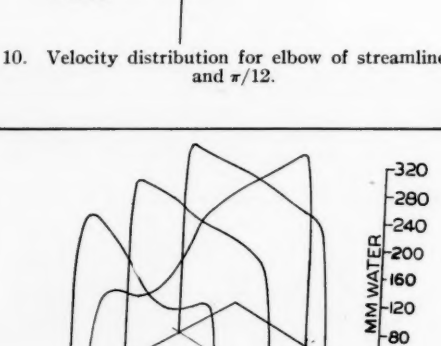

FIG. 11. Velocity distribution for elbow of streamlines $3\pi/8$ and $\pi/8$.

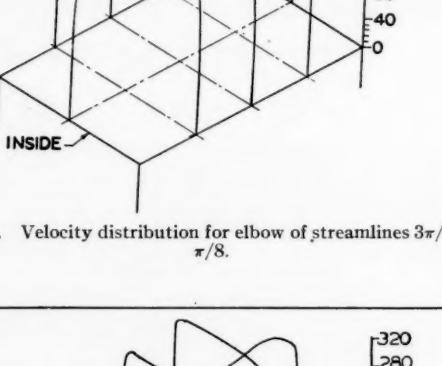

FIG. 12. Velocity distribution for elbow of streamlines $3\pi/8$ and $\pi/8$; A.R. = 1.5.

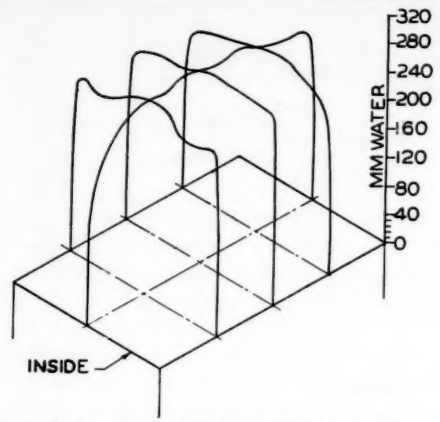

FIG. 13. Velocity distribution for conventional elbow with five guide vanes.

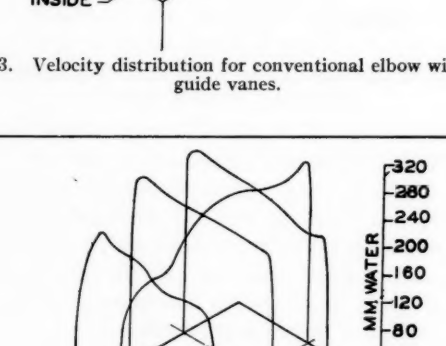

FIG. 14. Velocity distribution for elbow of streamlines $5\pi/12$ and $-\pi/8$ with two guide vanes.

the true elbow losses, it is necessary to eliminate the losses chargeable to the nozzle. All results have been expressed as a per cent of the total velocity head available at the elbow entrance. From the three nozzle surveys made at 100, 200, and 300 mm. water box pressure, a curve of pressure loss was obtained for the nozzle versus quantity, cu.ft. per sec.; this log plot is shown in Fig. 17. The surveys made at the elbow exits include the nozzle losses, and the total pressure loss may be expressed as

$$\Delta P_{\text{total}} = H_S - {}^1/_2\rho V^2$$

where H_S = box static pressure and ${}^1/_2\rho V^2$ = dynamic head measured at elbow exit. Therefore, for a given quantity of flow through the nozzle-elbow combination, the pressure loss, ΔP, for the nozzle is obtained from the graph (Fig. 17). Then

$$\Delta P_{\text{elbow}} = \Delta P_{\text{total}} - \Delta P_{\text{nozzle}}$$

and the per cent loss expressed in terms of the available head at the elbow entrance becomes

$$\text{loss} = \frac{\Delta P_{\text{elbow}} \text{ mm. } H_2O \times 100}{\text{mean dynamic head for nozzle (mm. } H_2O)}$$

TABLE 1

Elbow	(1) Mean Dynamic Head, q, at Exit Mm. H_2O	(2) Velocity, Ft. per Sec.	(3) Quantity, Cu.Ft. per Sec.	(4) ΔP Total Pressure Drop Through Elbow + Nozzle	(5) ΔPN −Loss Through Nozzle	(6) ΔP Elbow Loss Through Elbow Alone	(7) Total Head Available at Elbow Entrance	(8) Per Cent Loss
$\frac{5\pi}{12}, -\frac{\pi}{8}$	202.80	195.4	18.3	97.20	4.25	92.95	295.75	31.45
$\frac{11\pi}{24}, 0$	242.52	213.5	19.9	57.48	4.70	52.78	295.3	17.90
$\frac{5\pi}{12}, \frac{\pi}{12}$	247.80	216	20.15	52.20	4.80	47.40	295.2	16.06
$\frac{3\pi}{8}, \frac{\pi}{8}$	251.00	217.2	20.35	49.00	4.90	44.10	295.1	14.94
Conventional—5 guide vanes	252.28	218	20.45	47.72	4.95	42.77	295.05	14.5
$\frac{3\pi}{8}, \frac{\pi}{8}$, A.R. = 1.5	264.00	223	20.85	36.00	5.00	31.00	295	10.5
$\frac{5\pi}{12}, -\frac{\pi}{8}$—2 guide vanes	235.60	210.5	19.7	64.40	4.65	59.75	295.35	20.15
Conventional bend—no vanes	167.00	177.2	16.6	133.00	3.80	129.20	297.20	43.5

(1) From velocity surveys
(2) $V = 13.7\sqrt{q}$ mm. H_2O
(3) $Q = AV = 0.0936 \times$ (2)
(4) 300 − (1)
(5) From Fig. 17
(6) (4) − (5)
(7) 300 − (6)
(8) (6)/(7) × 100

Thus the losses chargeable to the nozzle itself are eliminated in the final results.

Szczeniowski has pointed out that an elbow composed of the stream lines $3\pi/8$ and $\pi/8$ is probably the most reasonable one, since the use of these streamlines tends to suppress any vortex formation in the throat of the elbow. As can be seen from the isometric plot, all the "shorter" elbows exhibit a marked separation of flow at the inner wall. Since the elbow of $3\pi/8$ and $\pi/8$ is the "longest" one of the group, it should have better flow characteristics; the isometric plot and the results confirm this.

The effect of aspect ratio was studied to a limited extent, in that the bend of streamlines $3\pi/8$ and $\pi/8$ had its aspect ratio increased from 0.67 to 1.5. Increasing the aspect ratio reduces the losses. The tests on the conventional bend were included for comparison (Fig. 13). Likewise Fig. 14 is included; this is the plot of velocity distribution for the "shortest" special elbow with two guide vanes installed. These vanes were calculated as two streamlines so placed as to give equal theoretical volumes of fluid flowing between them. These vanes did decrease the losses but not as much as expected. As shown in Fig. 15, there is some divergence between the inner wall and the first vane. This may account for the comparatively poor results; however, lengthening the vanes on the exit side would probably prove helpful, since the vanes were cut off short. Fig. 16 is included for comparison, since it is a plot of the velocity distribution for the conventional bend with guide vanes removed.

Table 1 lists the results obtained for the various elbows. From these results, a few suggestions for future study can be made. It is quite probable that bends with guide vanes and still higher aspect ratios would have lower losses than the elbows tested, since the special elbows were calcualted from two-dimensional flow and any skin friction on the walls will be detrimental to the realization of the calculated flow. Also, there are an infinite number of possible streamline combinations which will form the walls of the elbows, and it is likely that combinations other than those tested would give better results. One other possibility is the use of a pair of "long" streamlines (such as $3\pi/8$

FIG. 15. Photograph of elbow of streamlines of $5\pi/12$ and $-\pi/8$ showing divergence of guide vanes.

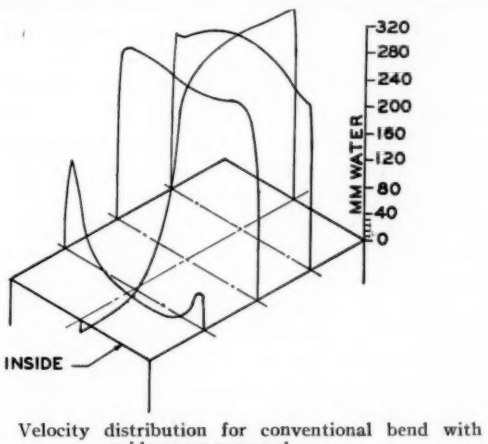

FIG. 16. Velocity distribution for conventional bend with guide vanes removed.

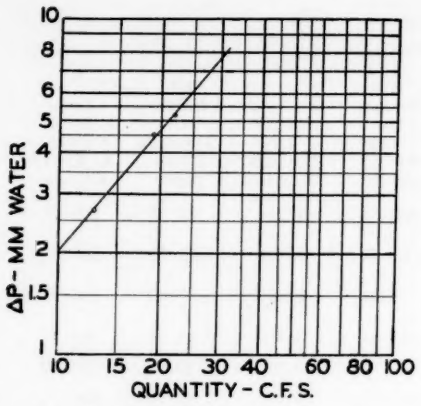

FIG. 17. Pressure drop through nozzle.

and $\pi/8$), cut off at points nearer the origin. Tests on bends of angles other than 90° would be desirable. As stated previously, the "longer" bends give better results ($\pi/8$ and $3\pi/8$ being the "longest"), and elbows which fulfill the conditions of no inflection points; that is, $V_{max.} \leq u$, have proved to give the best results.

The results show conclusively that the very "short" special elbows have poor flow characteristics, as evidenced by Figs. 8 and 9.

In the case of the "shortest" elbow tested, the air at the inner wall experiences a reversal of flow which, with the accompanying turbulence, greatly increases the losses. With the "longer" elbows, where the air is turned more gradually, lower losses would be expected, and, as stated before, this was found to be true.

A complete test program should include all the variations mentioned in the foregoing discussion and, in addition, tests at low velocities would be desirable.

Conclusions

Based solely on the results of these tests, the following conclusions can be made:

(1) The "short" elbows of special design have higher losses than conventional bends of the same size.

(2) Lower losses are obtained with "longer" special elbows having carefully selected streamlines.

(3) Increasing the aspect ratio of a bend from 0.67 to 1.5 reduces the losses.

(4) Addition of guide vanes to the "short" elbows, as done in these tests, does not appear to be worth while.

(5) Still lower losses are indicated by proper combination of point of cut off of streamlines and aspect ratio.

(6) Further investigation of bends having greater and lesser angles than 90° with various streamlines would appear to be in order.

References

[1] Szczeniowski, Boleslaw, *Design of Elbows in Potential Motion*, Journal of the Aeronautical Sciences, Vol. 11, No. 1, page 73, January, 1944.

[2] Patterson, G. N., *Notes on the Design of Corners in Duct Systems*, Aeronautical Research Committee, R. & M. No. 1773, 1936.

The Effect of Radius of Curvature and Preliminary Artificial Eccentricities on Buckling Loads of Curved Thin Aluminum-Alloy Sheets for Monocoque Constructions

GEORGES WELTER*

École Polytechnique de Montréal

ABSTRACT

In two previous papers,[1, 2] the results of tests on thin curved aluminum-alloy sheets in compression were presented. The present paper, whose publication was restricted during the war, shows that sheets of aluminum alloy tested under special conditions offer highly increased buckling and ultimate strengths under compression loads By decreasing the radius of cold-rolled curved sheets 40 to 50 per cent, a much greater ultimate buckling load can be obtained if these panels are tested under the usual radius of curvature (24 in.). Buckling and ultimate loads are distinctly higher, the usual buckling loads being exceeded by about 100 per cent.

Local eccentricities of the curved panels, generally assumed to be exceedingly detrimental to the bearing capacity in compression, did not decrease the buckling load of the panels. Even holes produced by shooting bullets through the panels did not weaken materially their normal buckling strength or their ultimate resistance.

INTRODUCTION

IN A PREVIOUS INVESTIGATION,[1, 2] it was observed that if the radius of curvature of curved thin aluminum-alloy sheets is decreased from 24 in. to 10 in., and tested with a radius of 24 in. by opening the plate elastically to the greater radius, a maximum buckling load was reached. This preliminary observation was based only on an insufficient number of specimens, so that this point had to be verified and a few series of tests with panels having a radius of curvature of 6 and 8 in., respectively, increasing in steps of 2 to 4 in. up to 24 in., were made. Also, completely flat panels as well as panels with a negative curvature of minus 24 in. were loaded with a curvature of plus 24-in. radius.

TESTS

Two complete series of tests were carried out in order to obtain reliable results. The first series was conducted with 17ST sheet "KB" of 0.036-in. thickness (24-in. width and 96-in. length). Another series, comprising tests on 18 panels, was made with cold-rolled pure aluminum sheet 2S $^3/_4$H of 0.032-in. thickness, designated by "L." The width of the panels was, in all cases, 6 in. and the length between the grips was 9 in.

Some results of tests on duralumin sheets are given in Fig. 1. The radius of curvature of these sheets varied between plus 24 in. and minus 24 in. The records of this series are so conclusive that it is hardly necessary to explain in detail these results. Similar curves are given in the report of the main investigation. More information regarding the test setup, the test apparatus used, the uniformity of loading achieved, the degree of edge restraint imposed, and the precautions taken to assure uniform condition throughout the series of tests may be found in a previous article by the author.[1] Of the first two panels with a radius of 8 in. and tested with 24-in. radius, one panel buckled at 3,080 lbs. and the ultimate load was lower than the buckling load. The second panel (KB 4) showed no buckling and the stress-strain curve went up to the maximum load of 3,850 lbs. without any inflection before attaining the ultimate value. The same result was obtained with three panels of 12-in. radius (KB 2, 5, and 13): maximum loads of 3,800 to 4,090 lbs. were reached without the characteristic buckling effect at lower loads. For higher radii, however, the buckling reappeared. Thus, for instance, with panel KB 9 of 14-in. radius, the buckling took place at 3,000 lbs., while the maximum load of 3,420 lbs. was appreciably lower than with the panel of 12-in. radius. Furthermore, somewhat lower buckling loads were recorded for panels KB 16 and 21 with radii of 18 and 24 in., respectively. The buckling took place at 2,510 lbs. and 2,630 lbs., while 3,500 lbs. and 3,370 lbs. were necessary to make these panels collapse. The flat plate KB 3 (radius ∞) tested with a radius of 24 in. had a still smaller buckling load (1,650 lbs.); it showed, however, about the same maximum load (3,410 lbs.) as the preceding panels. The lowest loads under which the panels buckled were registered with panels of negative curvature (minus 24-in. radius); panel KB 6 withstood only 960 lbs. and panel KB 20 only 940 lbs. before buckling. This last panel was rolled first with a radius of minus 24 in.; then it was rolled in the opposite direction to a radius of plus 24

Received December 18, 1945.

* Professor of Applied Mechanics.

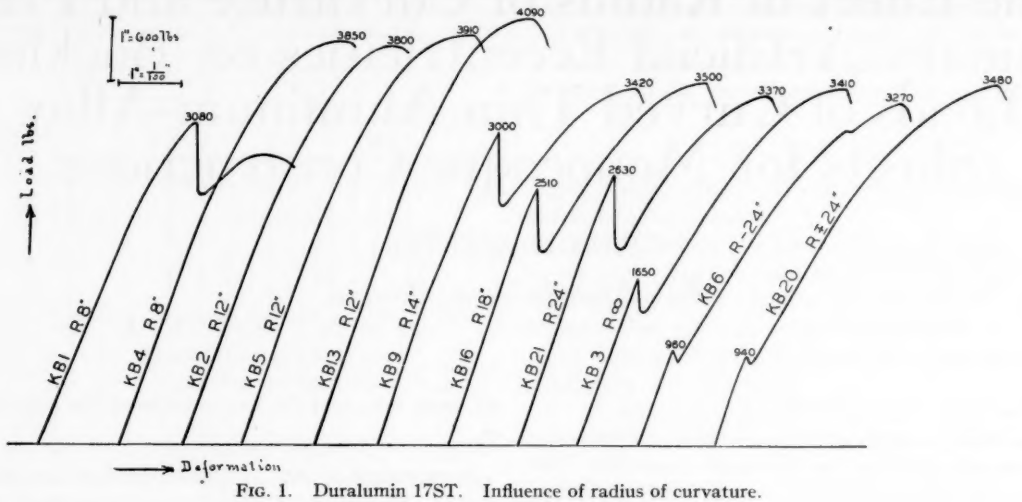

FIG. 1. Duralumin 17ST. Influence of radius of curvature.

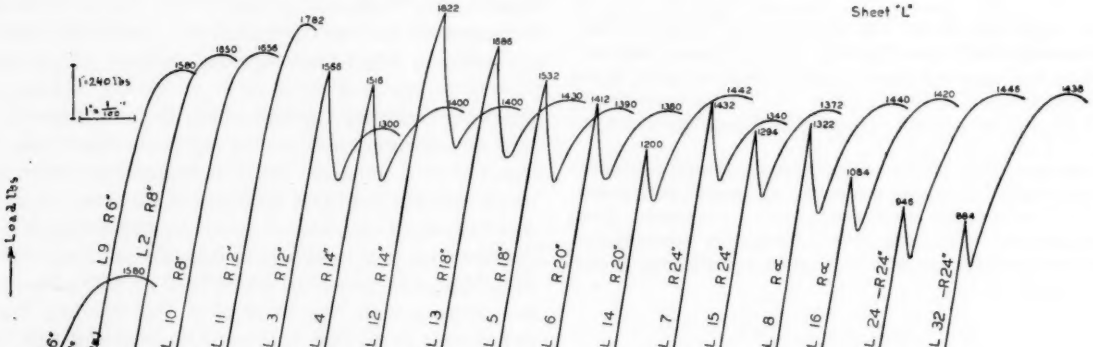

FIG. 2a. Aluminum. Influence of radius of curvature.

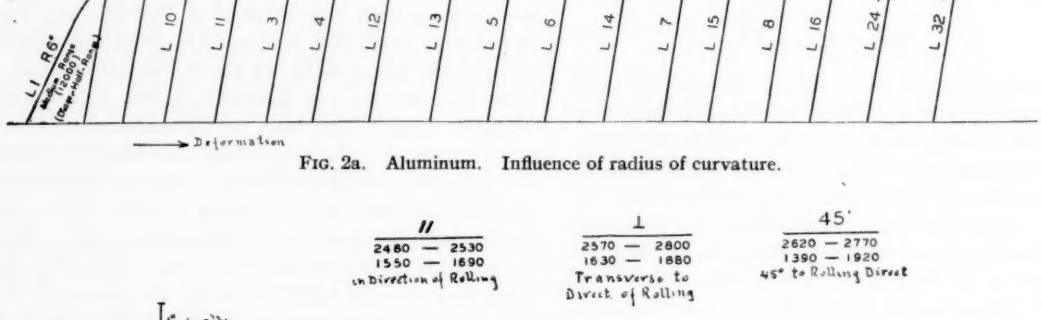

FIG. 2b. Normal buckling test results of 24ST—Sheet "I" (0.032-in. thickness).

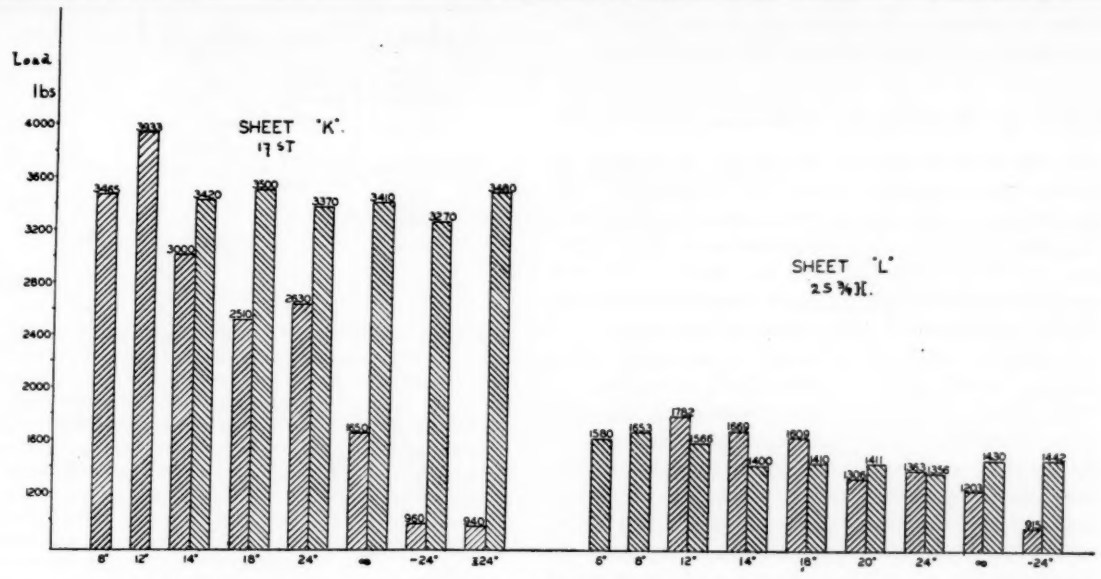

FIG. 3. Influence of radius of curvature. Buckling loads and ultimate loads of 17ST and 2S ¾H sheets (0.032-in. thickness).

in. and back again to minus 24-in. radius. The maximum load of two panels treated this way was 3,270 and 3,480 lbs.

It will be seen from these results that the radius of curvature of the panels being smaller than that of the steel grips with a radius of 24 in., has a pronounced influence on the buckling load as well as on the ultimate load of the sheets. According to these results, buckling does not take place with panels between about 8- and 14-in. radius. No buckling can be observed and the collapse load corresponding to the buckling load is about 20 per cent higher than that of panels with smaller or greater radii. These maximum loads are those experienced in the main investigation[1] (pages 368, 369 and Fig. 19, reported as "maximum special").

To confirm the observations of this interesting series, the same kind of tests was repeated with ¾ hard-rolled pure aluminum panels 2S of the same thickness (0.032 in.) and with curvatures of plus 6- to plus 24-in. radius.

As shown in Figs. 2, this series of tests is also convincing with regard to a certain increase of the maximum load for panels with smaller radii. Thus, for instance, panels with radii smaller than about 12 to 14 in. showed no buckling and collapse occurred at loads between 1,580 and 1,782 lbs. (L 1, 9, 2, 10, 11). Beginning with a radius of 12 in. the panels started buckling at loads as high as 1,566 lbs. For a radius of 14 in., the buckling in one case occurred at the high load of 1,822 lbs. (L12). From here the buckling load decreased systematically with increasing radius, reached 1,294 to 1,432 lbs. for a radius of 24 in., and was as low as 884 to 946 lbs. for a radius of minus 24 in.

It is interesting to note that, between 12- and about 20-in. radius, the ultimate load at the point of collapse is appreciably lower than the buckling load: as much as several hundred pounds. However, at radii of 24 in. or more, the stress-strain records again became normal—that is, the ultimate load is, as in the usual tests, higher than the buckling load.

In general, it may be said that these results correspond fairly well with those of the preceding series with regard to the influence of the radius of curvature on the behavior of these thin light-alloy panels. Furthermore, it is of interest to state that the buckling load for ¾ hard cold-rolled and stretched pure aluminum, with a yield point of about 35 per cent, that of 24ST alloy, has for panels with 12- and 14-in. radius a buckling load that is about as high as that of 24ST alloy. On the other hand, however, the collapse load is only about half that of 24ST, as may be seen in Fig. 2a, representing normal buckling test results with 24ST sheets of the same thickness (0.032 in.). Even for a radius of 24 in., the buckling load of 1,294 to 1,432 lbs. is not much smaller than that of 24ST sheet, especially if we take into consideration the fairly wide variations measured during the main tests. In any case, it can be seen from these investigations that something important happens with panels rolled to a radius between 8 and 14 in. and afterward opened for testing to a radius of 24 in. The average results of both these series are illustrated in Fig. 3 which shows the pronounced effect of their radius of curvature on the test results.

To investigate this region somewhat more precisely, it seems necessary to make a few more series of supplementary tests in this field. The absence of buckling for radii between 8 and 14 in. and the important in-

crease in ultimate load of these panels may be of practical interest for highly stressed skin constructions.

Effect of Preliminary Artificial Eccentricity

In the bibliography on the theory of buckling of curved aluminum-alloy sheets in compression, the opinion is generally expressed that the maximum buckling load of panels is extremely sensitive to slight differences in initial eccentricities of the sheets. The wide variations of the buckling loads for individual tests are mainly explained by these initial eccentricities.

In order to study the influence of the initial eccentricity of sheets on the buckling load, a few tests on 24ST curved panels (radius of curvature 24 in.), provided with initial local eccentricities of different values were made. Thus, several indentations with a 10-mm. steel ball were made in the upper third of the free length of a panel. The pressures were of 500, 1,000, 1,500, and 2,000 kg. and the eccentricities of the indentations varied between about one to three times the thickness (0.032 in.) of the sheet. The buckling of this panel with nine indentations of different eccentricities, as shown in Fig. 4 (H 36), placed under compression load, was not influenced at all by these artificial eccentricities. The buckling took place in the lower part of the panel, as is usual with panels free of eccentricities, and the buckling had the normal appearance of that in panels tested without eccentricities. The load-deflection diagram of this panel was also normal and the maximum buckling load of 1,530 lbs., as well as the ultimate load of 2,860 lbs., was not different from other results obtained with this material under the usual test conditions.

However, in order to determine if indentations with a steel ball of larger diameter would not give somewhat different results, this test was repeated with panel Ic 7. Two indentations with a ball of 1-in. diameter under loads of 500 kg. were made in the upper and the lower parts of the panel, while four other indentations with a load of 1,000 kg. and the same ball were made on the right and left sides in the upper and lower parts of this panel (Fig. 4). Again, the compression test showed that buckling was not at all influenced by this series of artificial eccentricities of a few times the thickness of the sheet. On the contrary, the direction in which buckling took place seems to indicate that it avoids these eccentricities. The buckling appeared right in the middle of the sheet — that is, in that part of the sheet which was free of any eccentricity. The lower edge of the buckling seems even to stop along and at some distance from the main direction of these indentations.

Therefore, it may be said that artificial eccentricities of this kind are not the cause of premature buckling, and the divergence of buckling results of thin sheets under compression loads cannot be attributed mainly to this cause. Moreover, the load deflection diagram does not show any abnormal shape and the

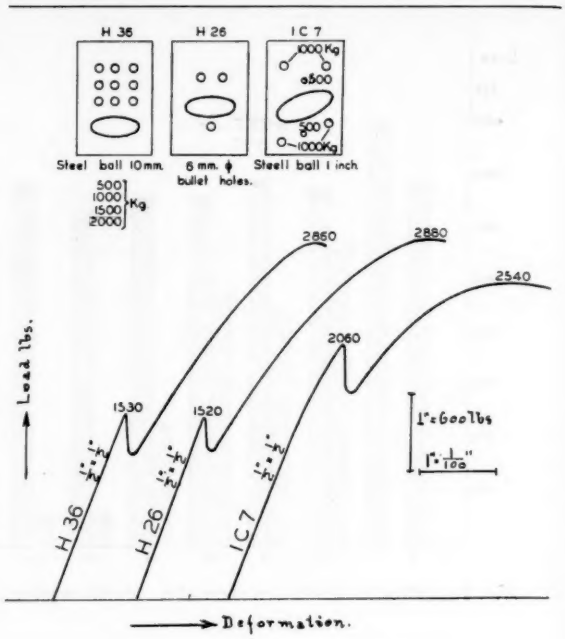

Fig. 4. Influence of eccentricity.

buckling load of 2,060 lbs. is comparatively high for this sheet (see Fig. 4).

As these tests had given the desired information about local artificial eccentricities, complementary tests with a somewhat different kind of eccentricity were executed. As shown in Fig. 5, three indentations of maximum effect were made in panel H 26. With a 0.22-in. rifle, three bullets were shot through this panel (two in the upper part and one in the lower part of the panel, Fig. 4, H 26). The edge of the holes was distinctly deformed plastically, so that part of the mass of the sheet was forced outside the plane of the panel. Despite this rather crude local deformation of the sheet, buckling did not start from or spread across these initial eccentricities. Independently of these holes produced dynamically, buckling took place in the usual manner, not in the least influenced by this kind of deformation. Consequently, the stress-strain record showed no peculiarity whatever and it can be characterized as normal for this sheet.

It may be seen from these tests that, even with a pronounced artificial eccentricity produced by ball indentations of 10-mm. and up to 1-in. diameter, which under loads of up to 1,000 kg. result in eccentricities of several times the thickness of the sheets, there could not be observed any kind of influence on the mechanism of the buckling of these thin alloy sheets. If the sensitivity of the sheets to slightest differences in initial eccentricities is as great as supposed by different investigators, it would have been proved by

(*Continued on page 604*)

Higher Modes of Vibration by a Method of Sweeping

L. BESKIN* AND R. M. ROSENBERG†

Consolidated Vultee Aircraft Corporation

SUMMARY

A method is presented whereby the frequencies and deflection curves in bending and torsional vibrations of continuous beams of variable section can be found. Emphasis is placed on the determination of modes higher than the first.

This method was developed in an effort to use the Stodola iteration process in the determination of higher modes of vibration. One of the most important advantages of the method presented here is that its application does not require unfamiliar tools of mathematics such as matrix techniques. Therefore, actual calculations may be reduced to a routine that may be entrusted to computers having a high-school background only.

This paper, containing a numerical example worked out in detail, was written in such a manner as to emphasize application rather than veil it.

In applying the method, it is necessary to determine the first $(n-1)$ modes. The nth mode is then found in the following manner:

(1) A "reasonable" estimate (as defined in the body of the paper) of the nth mode is made.

(2) The preceding $(n-1)$ modes are cleared from the estimated nth mode by a method of sweeping.

(3) The swept mode is operated on with Stodola's iteration method leading to convergence to the nth mode.

For great accuracy, alternate sweeping operations and Stodola iterations are continued leading to an indefinitely close approximation of the nth mode.

This method has been used by the authors with excellent results and presents the best compromise between simplicity, accuracy, and reduction of labor known to them.‡

INTRODUCTION

IN THE FIELDS of aeronautical and mechanical engineering the need frequently exists for computing the frequencies and deflection curves of higher modes of vibration of continuous systems. In systems of constant section, straightforward solutions to this problem exist. In systems of variable section, more or less laborious iteration methods are known which permit the calculation of approximations to these higher modes. Usually, these iteration methods rely on either of two principles: (1) The Holzer method and its variations make use of the fact that, in the absence of damping, the force in bending vibrations (or the torque in torsional vibrations) required to maintain vibrations in the principal modes, is zero. (2) Most other methods make use of the orthogonality relation between normal modes. In application, the Holzer method and its variations require an estimate of the frequency of vibrations of the mode; the methods using orthogonality restraints require an estimate of the deflection curve of the mode. It is believed that a good estimate of the deflection curve of the mode requires far less experience and can be much more easily visualized than a good guess of the frequency. In this respect, methods relying on the orthogonality principle are, therefore, more easily applied by novice and expert alike. However, those of the latter methods now in general use suffer from certain defects. Some, although theoretically sound, give numerically unsatisfactory results; others require a knowledge of matrix methods to carry out the iterations. Therefore, the present method was developed in an effort to provide a technique that would be so simple to use that a high-school graduate could apply it without learning special mathematical techniques, that would give excellent numerical results carrying only a small number of significant figures (usually five), and that would be sufficiently rapid to be no more tedious than methods now in general use.

A relatively large number of contributions[1, 2, 3] to the field of vibration analysis have recently appeared in the literature. These have, generally, provided worth-while labor saving devices or greater accuracy of results. They have, however, generally relied on the principles enumerated above for the calculation of higher modes of vibration.

In this respect the present paper is no exception. A method of "sweeping" is applied to an assumed deflection curve in order to clear from it the lower modes. Stodola's method[4] is then applied to the swept curve and results in the convergence of the Stodola process to the nth mode if the preceding $(n-1)$ modes have been swept from the function.

In applying the method discussed here to the nth mode a "reasonable" estimate of the deflection curve of the nth mode is made. A "reasonable" estimate differs from a "possible" assumption[1] in that it not only satisfies the boundary conditions, as does the latter, but it also possesses the known general character of the

Presented at the Structures Session, Fourteenth Annual Meeting, I.A.S., New York, January 29–31, 1946.

* Design Specialist, Consolidated Vultee Aircraft Corporation, Vultee Field Division, Downey, Calif.

† Design Specialist, Consolidated Vultee Aircraft Corporation, Nashville, Tenn. Now, Purdue University, School of Aeronautics.

‡ After this paper was completed it came to the attention of the authors that a similar procedure has been presented in reference 9. The work presented here was begun in 1941 and contains much material and theory not given in reference 9.

mode. Thus, a reasonable deflection curve of the nth mode of a cantilever beam in bending vibrations possesses $(n-1)$ nodes and has zero deflection and slope at the root. The components of the preceding $(n-1)$ modes (as determined by previous computations) are cleared or "swept" from the assumed curve, whereupon it is subjected to the Stodola process.

If the preceding $(n-1)$ modes were exactly known, they could be completely swept out, and, if the numerical computations were made with complete accuracy, repeated operation on the swept curve with the Stodola process would lead to continued convergence to the nth mode. This procedure is, unfortunately, not possible because all modes up to $(n-1)$st were, themselves, determined by a converging iteration process. They can, therefore, be swept from the assumed curve only within the accuracy with which they have been determined. It must be assumed, then, that residuals of the lower modes are left even after sweeping, and continued application of the Stodola process will amplify these residuals to the extent that repeated Stodola iterations, done upon the swept curve, will eventually converge to the first mode. This difficulty can be overcome if each Stodola iteration is followed by a sweeping procedure. If this is done, the method presented here will continue indefinitely to converge to the desired mode. It can be shown that the sweeping operation need not be applied in its entirety to each iteration. For instance, when calculating the fourth mode, if the preceding three modes have been determined with equal accuracy, the first mode should be swept out after each iteration; but it is sufficient to sweep out the second mode after every other iteration and the third mode after every fifth. Practice has shown that the frequency can be calculated within less than 1 per cent of that resulting from three iterations and four complete sweeping operations if the assumed curve is swept once, and the frequency is calculated from the results of a single Stodola iteration. This minimum of work is sufficient in problems involving forced vibrations and resonance. In three-dimensional flutter analysis, however, accurate knowledge of the deflection curve is required, and the location of the nodes may determine stability or instability against flutter. In these cases it is recommended that the succession of sweeping operations and Stodola iterations be continued until successive values for the deflection curve and frequency are obtained which do not change sensibly after additional iterations.

The nomenclature used here is given in Table 1.

Stodola's Iteration Method

Stodola's iteration method may be described as follows: A system of length l, having a mass per unit length dm, is assumed to deflect in a shape $\bar{y}_1^1(x)$, henceforth identified as $\bar{y}_1^1$. If the frequency of the system is $\omega = 1$, the inertia loading per unit span is $\bar{y}_1^1\,dm$. Loading the system with $\bar{y}_1^1\,dm$, a new deflection curve $\bar{y}_1^2$ is obtained. The ratio $\bar{y}_1^1/\bar{y}_1^2$ is a first approximation of the square of the frequency. This process may be repeated by loading the system with $\bar{y}_1^2\,dm$ and will converge to the first mode as shown below.*

The assumed deflection curve may be developed in the orthogonal series

$$\bar{y}_1^1 = Y_1 + a_2Y_2 + \ldots a_nY_n + \ldots \qquad (A)$$

When the frequency $\omega = 1$, the inertia loading becomes

$$\bar{y}_1^1\,dm = Y_1\,dm + a_2Y_2\,dm + \ldots a_nY_n\,dm + \ldots \qquad (B)$$

For the deflection curve of the nth mode, the inertia loading is $(\omega_n)^2Y_n\,dm$. Therefore, the loading $a_nY_n\,dm$ gives a deflection $a_nY_n/(\omega_n)^2$, so that the second deflection curve of the process becomes

$$\bar{y}_1^2 = \frac{Y_1}{(\omega_1)^2} + \frac{a_2Y_2}{(\omega_2)^2} + \ldots \frac{a_nY_n}{(\omega_n)^2} + \ldots \qquad (C)$$

This differs from the first (assumed) deflection curve in that each term is divided by the square of its frequency. The qth deflection curve obtained from the $(q-1)$st iteration is

$$\bar{y}_1^q = \frac{1}{(\omega_1)^{2q}}\left[Y_1 + \left(\frac{\omega_1}{\omega_2}\right)^{2q} a_2Y_2 + \left(\frac{\omega_1}{\omega_3}\right)^{2q} a_3Y_3 + \ldots\right] \qquad (D)$$

Since it can be proved that $\omega_1 < \omega_2$ and $\omega_1 < \omega_3$, etc., all terms higher than the first decrease with increasing q. When $q \to \infty$ all terms higher than the first disappear.

Determination of the Second Mode

Let an assumed deflection curve of the second mode be represented by the orthogonal series

$$\bar{y}_2^1 = a_1Y_1 + a_2Y_2 + \ldots a_nY_n + \ldots \qquad (1)$$

Inasmuch as the orthogonality relation

$$\int^l Y_mY_n\,dm = 0,\ m \neq n \qquad (2)$$

* This proof is given in reference 5. It is repeated here because the same proof will be shown later to apply to convergence of the described process to any mode.

Table 1

	Sequence of Procedure →					
Mode	Assumed Curve	Swept Curve	Curve After Stodola Iteration	Swept Curve		Final Curve
1	$\bar{y}_1^1$	y_1^1	$\bar{y}_1^2$	y_1^2	...	Y_1
2	$\bar{y}_2^1$	y_2^1	$\bar{y}_2^2$	y_2^2	...	Y_2
.	.	.	.	.	.	.
.	.	.	.	.	.	.
.	.	.	.	.	.	.
n	$\bar{y}_n^1$	y_n^1	$\bar{y}_n^2$	y_n^2	...	Y_n
.	.	.	.	.	.	.
.	.	.	.	.	.	.
.	.	.	.	.	.	.

holds for principal modes, it can be shown that the coefficient of the nth term is

$$a_n = \int_0^l \bar{y}_n{}^1 Y_n \, dm / \int_0^l (Y_n)^2 \, dm \qquad (3)$$

Substituting Eq. (3) for $n = 1$ into Eq. (1) results in

$$\bar{y}_2{}^1 = \frac{\int_0^l \bar{y}_2{}^1 Y_1 \, dm}{\int_0^l (Y_1)^2 \, dm} Y_1 + a_2 Y_2 + \ldots a_n Y_n + \ldots \qquad (4)$$

The first mode is now cleared from the assumed curve and the swept function becomes

$$y_2{}^1 = \bar{y}_2{}^1 - \frac{\int_0^l \bar{y}_2{}^1 Y_1 \, dm}{\int_0^l (Y_1)^2 \, dm} Y_1 = a_2 Y_2 + \ldots a_n Y_n + \ldots \qquad (5)$$

The swept curve, obtained by taking the difference as indicated in the middle portion of Eq. (5), is represented by the series of the right-hand side which contains no first mode impurities. In carrying out the sweeping process numercially, the final deflection curve, obtained by applying the conventional Stodola process to the system, is used for Y_1.

If the series in Eq. (5) is divided through by a_2, it evidently becomes similar to the series of Eq. (A). Therefore the proof of convergence to the first mode of Eq. (A) holds identically for Eq. (5), except that repeated application of Stodola's procedure to y_2 causes convergence to the second mode.

One of the numerical limitations of the process is that the accuracy with which a higher mode can be determined is a function of the errors made in the previous modes.

Let

$$Y_1 = y_1{}^q + \Delta Y_1$$

where $y_1{}^q$ is the deflection curve of the first mode obtained after $(q - 1)$ Stodola iterations. The quantity swept from the curve is then,

$$a_1 y_1{}^q = \frac{\int_0^l \bar{y}_1{}^q (Y_1 - \Delta Y_1) \, dm}{\int_0^l (Y_1 - \Delta Y_1)^2 \, dm} (Y_1 - \Delta Y_1)$$

whereas, for complete sweeping, a quantity

$$a_1 Y_1 = \left(\int_0^l \bar{y}_1{}^q Y_1 \, dm / \int_0^l (Y_1)^2 \, dm \right) Y_1$$

TABLE 2

Beam Parameters and Estimated Reasonable Deflection Curves

Station*	I†	w‡	$\bar{y}_1{}^1$	$\bar{y}_2{}^1$	$\bar{y}_3{}^1$	$\bar{y}_4{}^1$
10	0.0001	0.0020	1.000	1.000	1.000	1.000
9	0.0005	0.0235	0.780	0.485	0.262	0.300
8	0.0014	0.0385	0.591	0.100	−0.275	−0.195
7	0.0026	0.0550	0.432	−0.125	−0.475	−0.228
6	0.0044	0.0690	0.309	−0.270	−0.312	−0.066
5	0.00725	0.0843	0.202	−0.320	−0.020	0.140
4	0.0105	0.0990	0.135	−0.265	0.226	0.060
3	0.0148	0.1150	0.080	−0.165	0.275	−0.136
2	0.0225	0.1262	0.038	−0.090	0.160	−0.140
1	0.0246	0.1342	0.011	−0.030	0.050	−0.060
0	0.0246	0.1342	0	0	0	0

* $\Delta x = 3.15$ in.
† (In.)⁴.
‡ Lbs. per in.

TABLE 3

Computed Deflection Curves—First Mode

Station	$\bar{y}_1{}^1$	$\bar{y}_1{}^2$	$\bar{y}_1{}^3$	$\bar{y}_1{}^4$
10	1.00000	1.00000	1.00000	1.00000
9	0.78000	0.83895	0.84194	0.84216
8	0.59100	0.68043	0.68600	0.68642
7	0.43200	0.53199	0.53907	0.53962
6	0.30900	0.39946	0.40680	0.40737
5	0.20200	0.28594	0.29251	0.29303
4	0.13500	0.19163	0.19683	0.19724
3	0.08000	0.11693	0.12051	0.12080
2	0.03800	0.06121	0.06324	0.06341
1	0.01100	0.02155	0.02232	0.02238
0	0	0	0	0

$\omega_1{}^2 = 1{,}392$ cycles per min. $\quad \Sigma(\bar{y}_1{}^4 - \bar{y}_1{}^1)^2 = 0.048827654$
$\omega_1{}^3 = 1{,}392$ cycles per min. $\quad \Sigma(\bar{y}_1{}^4 - \bar{y}_1{}^2)^2 = 0.000269215$
$\omega_1{}^4 = 1{,}391.5$ cycles per min. $\quad \Sigma(\bar{y}_1{}^4 - \bar{y}_1{}^3)^2 = 0.000001407$

should have been eliminated. Therefore, a first mode residual

$$\epsilon_1 = \frac{\int_0^l \bar{y}_1{}^q Y_1 \, dm}{\int_0^l (Y_1)^2 \, dm} Y_1 - \frac{\int^l \bar{y}_1{}^q (Y_1 - \Delta Y_1) \, dm}{\int_0^l (Y_1 - \Delta Y_1)^2 \, dm} (Y_1 - \Delta Y_1) \qquad (6)$$

is still contained in the function $y_2{}^1$, even after sweeping. It can be shown that the major portion of the residual is

$$\epsilon_1 \cong (Y_1 \int_0^l \bar{y}_1{}^q \Delta Y_1 \, dm - \Delta Y_1 \int_0^l \bar{y}_1{}^q Y_1 \, dm) / \int_0^l (Y_1)^2 \, dm$$

Operation on y_2 with the Stodola process will amplify this residual because, as was shown in the section "Stodola's Iteration Method," the Stodola process always

TABLE 4

Computed Deflection Curves—Second Mode

Station	$\bar{y}_2{}^1$	$y_2{}^1$	$\bar{y}_2{}^2$	$y_2{}^2$	$\bar{y}_2{}^3$	$y_2{}^3$	$\bar{y}_2{}^4$	$y_2{}^4$
10	1.000	1.00000	1.00000	1.00000	1.00000	1.00000	1.00000	1.00000
9	0.485	0.53705	0.60459	0.60465	0.60974	0.60986	0.61060	0.61068
8	0.100	0.18545	0.24010	0.24022	0.24645	0.24667	0.24775	0.24790
7	−0.125	−0.02815	−0.03262	−0.03247	−0.02919	−0.02891	−0.02823	−0.02804
6	−0.270	−0.17129	−0.19123	−0.19108	−0.19162	−0.19132	−0.19151	−0.19132
5	−0.320	−0.23067	−0.24690	−0.24676	−0.25090	−0.25062	−0.25165	−0.25147
4	−0.265	−0.19764	−0.23114	−0.23103	−0.23783	−0.23761	−0.23909	−0.23894
3	−0.165	−0.12335	−0.17421	−0.17413	−0.18143	−0.18128	−0.18271	−0.18261
2	−0.090	−0.06764	−0.10405	−0.10400	−0.10939	−0.10931	−0.11031	−0.11025
1	−0.030	−0.02237	−0.04058	−0.04056	−0.04302	−0.04299	−0.04342	−0.04340
0	0	0	0	0	0	0	0	0

$\omega_2{}^2 = 4{,}940$ cycles per min. $\quad \Sigma(y_2{}^4 - y_2{}^1)^2 = 0.017630543$
$\omega_2{}^3 = 4{,}936$ cycles per min. $\quad \Sigma(y_2{}^4 - y_2{}^2)^2 = 0.0003188165$
$\omega_2{}^4 = 4{,}936$ cycles per min. $\quad \Sigma(y_2{}^4 - y_2{}^3)^2 = 0.0000082542$

TABLE 5
Computed Deflection Curves—Third Mode

Station	$\bar{y}_3^1$	y_3^1	$\bar{y}_3^2$	y_3^2	$\bar{y}_3^3$	y_3^3	$\bar{y}_3^4$	y_3^4
10	1.00000	1.00000	1.00000	1.00000	1.00000	1.00000	1.00000	1.00000
9	0.26200	0.38104	0.38181	0.38281	0.38063	0.38131	0.38042	0.38107
8	−0.27500	−0.08438	−0.10265	−0.10105	−0.10367	−0.10260	−0.10364	−0.10263
7	−0.47500	−0.28615	−0.27778	−0.27640	−0.27455	−0.27371	−0.27403	−0.27327
6	−0.31200	−0.20207	−0.18728	−0.18673	−0.18436	−0.18419	−0.18416	−0.18404
5	−0.02000	−0.00648	−0.00101	−0.00135	−0.00205	−0.00253	−0.00243	−0.00296
4	0.22600	0.16601	0.14197	0.14109	0.13847	0.13760	0.13806	0.13717
3	0.27500	0.19927	0.18329	0.18234	0.18230	0.18143	0.18244	0.18157
2	0.16000	0.11455	0.13867	0.13799	0.14128	0.14066	0.14181	0.14119
1	0.05000	0.03505	0.06252	0.06222	0.06521	0.06495	0.06563	0.06536
0	0	0	0	0	0	0	0	0

ω_3^2 = 11,170 cycles per min. $\quad \Sigma(y_3^4 - y_3^1)^2 = 0.003619254$
ω_3^3 = 11,161 cycles per min. $\quad \Sigma(y_3^4 - y_3^2)^2 = 0.000061208$
ω_3^4 = 11,161 cycles per min. $\quad \Sigma(y_3^4 - y_3^3)^2 = 0.000001113$

TABLE 6
Computed Deflection Curves—Fourth Mode

Station	$\bar{y}_4^1$	y_4^1	$\bar{y}_4^2$	y_4^2	$\bar{y}_4^3$	y_4^3	$\bar{y}_4^4$	y_4^4
10	1.00000	1.00000	1.00000	1.00000	1.00000	1.00000	1.00000	1.00000
9	0.30000	0.22292	0.18475	0.18538	0.16756	0.16841	0.16146	0.16033
8	−0.19500	−0.28717	−0.28106	−0.28027	−0.27813	−0.27707	−0.27312	−0.27486
7	−0.22800	−0.20652	−0.17033	−0.17003	−0.14676	−0.14632	−0.13365	−0.13516
6	−0.06600	0.05630	0.12258	0.12242	0.13047	0.13035	0.13202	0.13114
5	0.14000	0.32571	0.22162	0.22169	0.19094	0.19084	0.17946	0.17907
4	0.06000	0.13897	0.06748	0.06779	0.04866	0.04895	0.04204	0.04189
3	−0.13600	−0.20880	−0.12747	−0.12679	−0.11068	−0.11005	−0.10447	−0.10456
2	−0.14000	−0.22881	−0.17457	−0.17392	−0.15109	−0.15050	−0.14028	−0.14034
1	−0.06000	−0.10137	−0.10148	−0.10115	−0.08973	−0.08942	−0.08299	−0.08301
0	0	0	0	0	0	0	0	0

ω_4^2 = 19,973 cycles per min. $\quad \Sigma(y_4^4 - y_4^1)^2 = 0.064720144$
ω_4^3 = 19,749 cycles per min. $\quad \Sigma(y_4^4 - y_4^2)^2 = 0.0063868492$
ω_4^4 = 19,712 cycles per min. $\quad \Sigma(y_4^4 - y_4^3)^2 = 0.0005581705$

TABLE 7
Computed Deflection Curves—Fourth Mode, with Partial Sweeping

Station	$\bar{y}_4^1$	y_4^1	$\bar{y}_4^2$	y_4^{2*}	$\bar{y}_4^{3*}$	y_4^{3*}	$\bar{y}_4^{4*}$	y_4^4
10	1.00000	1.00000	1.00000	1.00000	1.00000	1.00000	1.00000	1.00000
9	0.30000	0.22292	0.18475	0.18522	0.17015	0.16717	0.15484	0.15613
8	−0.19500	−0.28171	−0.28106	−0.28036	−0.27442	−0.27811	−0.27995	−0.27812
7	−0.22800	−0.20652	−0.17033	−0.16982	−0.14432	−0.14558	−0.13380	−0.13253
6	−0.06600	0.05630	0.12258	0.12279	0.13071	0.13218	0.13660	0.13711
5	0.14000	0.32571	0.22161	0.22187	0.18970	0.19197	0.18231	0.18252
4	0.06000	0.13897	0.06748	0.06757	0.04705	0.04844	0.03978	0.04007
3	−0.13600	−0.20880	−0.12747	−0.12729	−0.11193	−0.11177	−0.11043	−0.10999
2	−0.14000	−0.22881	−0.17457	−0.17439	−0.15178	−0.15220	−0.14608	−0.14568
1	−0.06000	−0.10137	−0.10148	−0.10139	−0.08997	−0.09032	−0.08605	−0.08585
0	0	0	0	0	0	0	0	0

ω_4^2 = 19,973 cycles per min. $\quad \Sigma(y_4^4 - y_4^1)^2 = 0.0647201444$
ω_4^{2*} = 19,748 cycles per min. $\quad \Sigma(y_4^4 - y_4^{2*})^2 = 0.0064259824$
ω_4^{4*} = 19,709 cycles per min. $\quad \Sigma(y_4^4 - y_4^{3*})^2 = 0.0006223984$
ω_4^4 = 19,712 cycles per min. $\quad \Sigma(y_4^4 - y_4^{4*})^2 = 0.0001521064$

amplifies the lowest mode present in the series. Therefore, unless the first mode has been computed to high accuracy, it will be necessary to sweep after each application of Stodola's procedure leading, for the second mode, from $\bar{y}_2^q$ to y_2^q.

Determination of Modes Higher than the Second

From the preceding development it is clear that, when determining the third mode, the first and second modes are swept from the deflection curve by the operation

$$y_3^1 = \bar{y}_3^1 - \frac{\int_0^l \bar{y}_3^1 Y_1 \, dm}{\int_0^l (Y_1)^2 \, dm} Y_1 - \frac{\int_0^l \bar{y}_3^1 Y_2 \, dm}{\int_0^l (Y_2)^2 \, dm} Y_2 \quad (7)$$

In the general case, the swept function of the nth mode after the $(q-1)$st Stodola iteration is given by

$$y_n^q = \bar{y}_n^q - \sum_{i=1}^{n} \frac{\int_0^l \bar{y}_n^q Y_i \, dm}{\int_0^l (Y_i)^2 \, dm} Y_i \quad (8)$$

Practical Application

The parameters required for calculating vibration modes of a system are the mass and elastic characteristics along the span. After these are known it is convenient to divide the length into ten or more equal increments, called sections. Stations are located in the center of each section. When calculating bending vi-

TABLE 8
Third Mode—First Sweeping Operation

Station	① Y_1*	② Y_2*	③ $y_3{}^1$†	④ w	⑤ $w(Y_1)^2$ ④ × ①²	⑥ $w(Y_2)^2$ ④ × ②²	⑦ $wY_1y_3{}^1$ ④ × ① × ③	⑧ $wY_2y_3{}^1$ ④ × ② × ③	⑨ $a_1{}^1Y_1$ (−0.17754) × ①	⑩ $a_2{}^1Y_2$ (−0.16183) × ②	⑪ ③ − ⑨ − ⑩	⑫ ⑪/1.33937 $y_3{}^1$ (normal)
10	1.00000	1.00000	1.00000	0.00200	0.0020000	0.0020000	0.0020000	0.0020000	−0.17754	−0.16183	1.33937	1.00000
9	0.84216	0.61068	0.26200	0.02350	0.0166672	0.0087639	0.0051852	0.0037600	−0.14952	−0.09883	0.51035	0.38104
8	0.68642	0.24790	−0.27500	0.03850	0.0181400	0.0023660	−0.0072674	−0.0026246	−0.12187	−0.04012	−0.11301	−0.08438
7	0.53962	−0.02804	−0.47500	0.05500	0.0160154	0.0000432	−0.0140975	−0.0007325	−0.09580	0.00454	−0.38374	−0.28651
6	0.40737	−0.19132	−0.31200	0.06900	0.0114508	0.0025256	−0.0087700	0.0041187	−0.07232	0.03096	−0.27064	−0.20272
5	0.29303	−0.25147	−0.02000	0.08430	0.0072384	0.0053309	−0.0004940	0.0004240	−0.05202	0.04070	−0.00868	−0.00648
4	0.19724	−0.23894	0.22600	0.09900	0.0038515	0.0056521	0.0044131	−0.0053460	−0.03502	0.03867	0.22235	0.16601
3	0.12080	−0.18261	0.27500	0.11500	0.0016782	0.0038348	0.0038203	−0.0057750	−0.02145	0.02955	0.26690	0.19927
2	0.06341	−0.11025	0.16000	0.12620	0.0005074	0.0015340	0.0012803	−0.0022262	−0.01126	0.01784	0.15342	0.11455
1	0.02238	−0.04340	0.05000	0.13420	0.0000672	0.0002528	0.0001502	−0.0002912	−0.00397	0.00702	0.04695	0.03505
0	0	0	0	0.13420	0	0	0	0	0	0	0	0
	4.17243	0.81255	0.89100		0.0776161	0.0323033	0.0137798	0.0052278	0.74077	0.13150	1.76327	1.31648

$a_1{}^1 = \Sigma wY_1y_3{}^1/\Sigma w(Y_1)^2 = -0.0137798/0.0776161 = -0.177538$
$a_2{}^1 = \Sigma wY_2y_3{}^1/\Sigma w(Y_2)^2 = -0.0052278/0.0323033 = -0.161835$

* Obtained from preceding calculations.
† Reasonable estimate of third mode.

TABLE 9
Third Mode—First Stodola Iteration

Station	① I Table 2 Column ①	② w Table 2 Column ②	③ $y_3{}^1$ Table 8 Column ⑫	④ $wyy_3{}^1$ ② × ③	⑤ S ↓Σ④	⑥ M ↓Σ⑤	⑦ M/I ⑥/①	⑧ $\frac{1}{3.15}\frac{dy}{dx}$ ↑Σ⑦	⑨ $y_3{}^2/9.922$ ↑Σ⑧	⑩ $\left(\frac{y_3{}^2}{9.922}\right)_{norm.}$ ⑨/29.91263	⑪ $I\left(\frac{d^2y}{dx^2}\right)^2$ ⑥ × ⑦	⑫ $(y_3{}^2)^2/98.456$ ⑨²	⑬ $w(y_3{}^2)^2/98.456$ ② × ⑫
10	0.00010	0.00200	1.00000	0.002000					29.91263	1.00000		894.7654	1.78953
					0.002000			18.49157					
9	0.00050	0.02350	0.38104	0.008954		0.002000	4.00000		11.42106	0.38181	0.008000	130.4406	3.06535
					0.010954			14.49157					
8	0.00140	0.03850	−0.08438	−0.003249		0.012954	9.25286		−3.07051	−0.10265	0.119862	9.4280	0.36298
					0.007705			5.23871					
7	0.00260	0.05500	−0.28651	−0.015758		0.020659	7.94577		−8.30922	−0.27778	0.164152	69.0431	3.79737
					−0.008053			−2.70706					
6	0.00440	0.06900	−0.20207	−0.013943		0.012606	2.86500		−5.60216	−0.18728	0.036116	31.3842	2.16551
					−0.021996			−5.57206					
5	0.00725	0.08430	−0.00648	−0.000546		−0.009390	−1.29517		−0.03010	−0.00101	0.012162	0.0009	0.00008
					−0.022542			−4.27689					
4	0.01050	0.09900	0.16601	0.016435		−0.031932	−3.04114		4.24679	0.14197	0.097110	18.0352	1.78548
					−0.006107			−1.23575					
3	0.01480	0.11500	0.19927	0.022916		−0.038039	−2.57020		5.48254	0.18329	0.097768	30.0582	3.45669
					0.016809			1.33445					
2	0.02250	0.12620	0.11455	0.014456		−0.021230	−0.94356		4.14809	0.13867	0.020032	17.2067	2.17149
					0.031265			2.27801					
1	0.02460	0.13420	0.03505	0.004704		0.010035	0.40793		1.87008	0.06252	0.004094	3.4972	0.46932
					0.035969			1.87008					
0	0.02460	0.13420	0	0		0.046004	1.87008		0	0	0.086031	0	0
											0.645327		19.06380

$$\omega = \frac{60}{2\pi}\sqrt{\frac{gE\int_0^l I(d^2y/dx^2)^2dx}{\int_0^l wy^2\,dx}} \text{ cycles per min., where } g = 386.4 \text{ in./sec.}^2 \text{ and } E = 10.3 \times 10^6 \text{ lbs. per sq.in. (here).}$$

$$\omega_3{}^2 = \frac{60}{6.2832}\sqrt{\frac{386.4 \times 10.3 \times 10^6 \times 0.645327}{19.06380 \times 98.456}} = 11{,}170 \text{ cycles per min.}$$

brations, the mass and elastic parameters of each station are paired. When calculating torsional vibrations, the mass moment of inertia at each station is paired with the torsional elasticity parameter at the end of the section in which the station is located. When these recommendations are followed, the length increment is a constant all along the span and may be taken outside the summation sign—i.e.,

$$\int f(x)\,dx \cong \sum f(x)\,\Delta x = \Delta x \sum f(x)$$

In performing the computations it has been found convenient to carry out Stodola iterations and sweeping operations on separate tables (see Tables 8 and 9). Although this requires working back and forth between two tables, it has the advantage of greater simplicity because each table contains repetitions of the same process. For the Stodola iterations a tabular method is preferred to the graphical one, originally devised by Stodola.[4] The method presented here is due to Burgess[7] except that, because of a simplification, the number of operations has been reduced by one (see Table 9).

In practice it has been found convenient to "normalize" the deflection curves after each Stodola iteration and after each sweeping operation. Although this leads to two additional operations that are not essential, it is preferred because errors are more quickly discovered. The term "normalizing condition" is conventionally defined by $\int_0^l Y_n\,dm = M$. However, recently it has come into practice to refer to a mode as normalized if a reference amplitude (say the tip ampli-

tude of a cantilever beam) is equal to unity.[6] In this paper, the term "normalizing" is used in the latter sense—i.e., a mode is normalized by dividing the amplitudes at all stations by the reference amplitude.

In calculating frequencies from the deflection curves, Raleigh's principle of equating maximum kinetic and strain energies is applied. This can be shown to be identical to the weighted average method used by Boukidis and Ruggiero.[1]

Numerical Example

For a numerical example, the first four bending vibration modes of a cantilever beam have been computed by the method presented here. In all modes a reasonable deflection curve has been assumed and three Stodola iterations have been carried out. In all modes higher than the fundamental, the first Stodola iteration was preceded by a complete sweeping of all modes lower than the one to be calculated, and each Stodola iteration was again followed by a complete sweeping procedure. In addition to these computations, certain partial sweeping operations have been carried out for the fourth mode; these are compared with results from the complete procedure. For each mode the results of each Stodola iteration have been used to compute frequencies identified by superscripts. Therefore, for the nth mode three frequencies have been calculated, identified as ω_n^2, ω_n^3, and ω_n^4. The last is, of course, the most accurate value, and the others may be compared with the last to estimate the degree of accuracy obtainable with an abbreviated procedure.

In addition to the frequencies, the deflection curves have also been compared. In the comparison of the deflection curves the principle of least squares has been applied.

Let $\Delta y_n = Y_n - y_n^q$ be the deviation of the computed values from the correct values. If the problem at hand were one of comparing observed values of a phenomenon with computed values, the Gaussian law of errors would give the probability of obtaining the observed values, as[8]

$$P = (h/\sqrt{\pi})^m e^{-h^2\Sigma(\Delta y_n)^2}$$

which is a maximum when $\sum (\Delta y_n)^2$ is a minimum. Therefore $\sum(Y_n - y_n^q)^2$ may be considered to furnish an evaluation of the accuracy of the computed deflection curves. In computing this quantity, the final computed mode has been defined as the pure mode—i.e.,

$$Y_n \equiv y_n^4$$

and the quantities to be compared with one another are

$$\sum(y_n^4 - y_n^1)^2$$
$$\sum(y_n^4 - y_n^2)^2$$
$$\sum(y_n^4 - y_n^3)^2$$

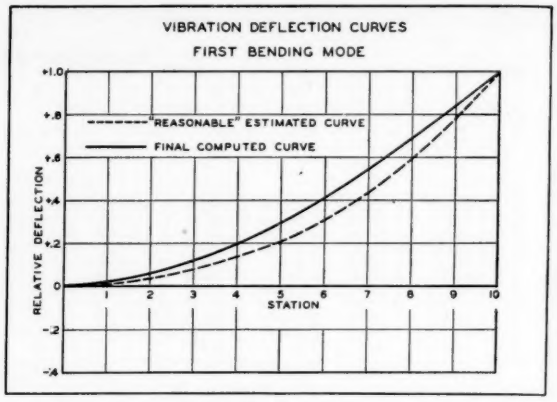

Fig. 1.

The results of this investigation are contained in Tables 2 to 7. In addition, the first sweeping operation and Stodola iteration, used to calculate the third mode, are shown in detail in Tables 8 and 9 in order to illustrate the procedure.

The fourth mode has also been calculated by the following abbreviated procedure:

(a) Assume a reasonable deflection curve $\bar{y}_4^1$.
(b) Sweep out the first, second, and third modes leading to y_4^1.
(c) Apply the Stodola procedure leading to $\bar{y}_4^2$.
(d) Sweep out the first mode only leading to y_4^{2*}.
(e) Apply the Stodola procedure leading to $\bar{y}_4^{3*}$.
(f) Sweep out the first and second modes only leading to y_4^{3*}.
(g) Apply the Stodola procedure leading to $\bar{y}_4^{4*}$.
(h) Sweep out the first mode only leading to y_4^{4*}.

This shortened procedure leads to excellent results for both the frequency and deflection curve, as shown in Table 7.

Figs. 1, 2, 3, and 4 show the assumed and final deflection curves for the first for bending modes.

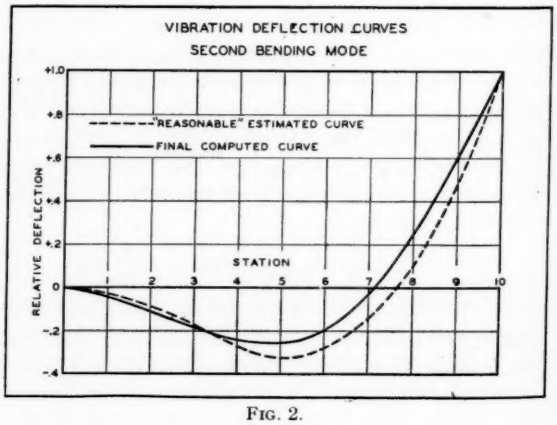

Fig. 2.

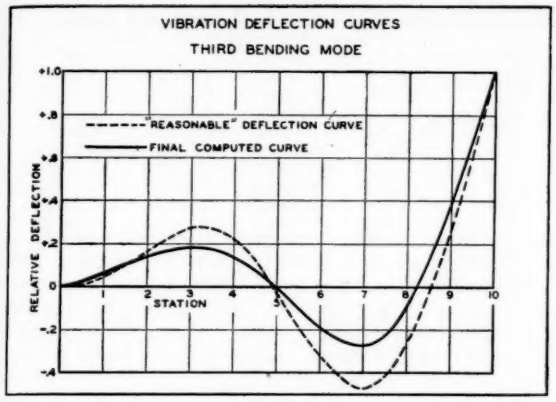

FIG. 3.

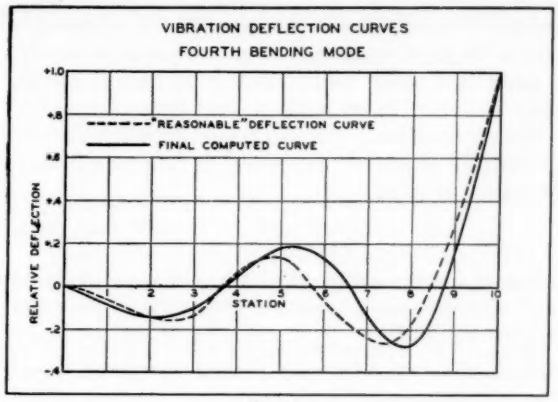

FIG. 4.

Appendix I

Boukidis and Ruggiero[1] have presented a method of determining higher modes of vibration which is, in some respects, similar to the present one. From the standpoint of mathematical elegance their method is superior to the one contained in this paper, because all modes are calculated from a single assumed curve and because the tedious Stodola process is applied to the first mode only. In actual application, however, the method of reference 1 seems to have certain defects that render the method presented here preferable when modes higher than the second have to be calculated.

It is shown in reference 1 that*

$$\bar{y}_2{}^q = \bar{y}_1{}^q - (\omega_1)^2 \bar{y}_1{}^{q+1} \tag{I-1}$$

In the section on Stodola's method of this paper, it was shown that the first term on the right-hand side of Eq. (I-1) is

$$y_1{}^q = \frac{1}{(\omega_1)^{2q}}\left[Y_1 + \left(\frac{\omega_1}{\omega_2}\right)^{2q} a_2 Y_2 + \left(\frac{\omega_1}{\omega_3}\right)^{2q} a_3 Y_3 + \dots \right] \tag{I-2}$$

The second term on the right-hand side of Eq. (I-1) is

$$y_1{}^{q+1} = \frac{1}{(\omega_1)^{2q}}\left[Y_1 + \left(\frac{\omega_1}{\omega_2}\right)^{2q+2} a_2 Y_2 + \left(\frac{\omega_1}{\omega_3}\right)^{2q+2} a_3 Y_3 + \dots \right] \tag{I-3}$$

Neglecting terms of an order higher than the second, the quantity of Eq. (I-1) is evidently

$$y_2{}^q = \frac{1}{(\omega_1)^{2q}}\left\{ \left(\frac{\omega_1}{\omega_2}\right)^{2q}\left[1 - \left(\frac{\omega_1}{\omega_2}\right)^2 \right] a_2 Y_2 \right\} \tag{I-4}$$

Comparing Eq. (I-4) with either of Eqs. (I-2) or (I-3), it appears that $y_2{}^q$ is the difference between two quantities that tend toward one another for large values of q (a large number of iterations). For proof we need only realize that in Eq. (I-4)

$$\lim_{q \to \infty} (\omega_1/\omega_2)^{2q} = 0 \tag{I-5}$$

or, comparing the difference of Eq. (I-1) with either one of the subtrahends

$$\lim_{q \to \infty} [\text{Eq. (I-2)} - \text{Eq. (I-3)}]/\text{Eq. (I-2)} = 0 \tag{I-6}$$

This fact explains the recommendation in reference 1 that as many places should be retained in the calculations as the calculating machine can handle.

It will now be shown that the method of reference 1 requires a relatively large number of iterations (large q) for dependable results.

Since the second mode is calculated from the second term of the series of a function that is made to resemble the first mode as closely as can be estimated,[1] the coefficient of the second term (or the presence of the second mode in the function) will be small. Furthermore, no control can be exercised over the magnitude of the coefficients of the various terms. Therefore, the coefficient of the mth term in the assumed curve may easily be larger than that of the nth term (where $n > m$).

The method presented by Boukidis and Ruggiero[1] has been used to calculate the second and third modes of the beam treated in the numerical example. To carry out these calculations, ten significant figures and, occasionally, 13 places were retained in the computations. This was necessary because retaining five significant figures as used in the method presented in this paper resulted in only a single significant figure for the third mode.

The deflection curves, calculated by means of reference 1, are identified by stars. The results are given in Table 10, and the average error is compared with that resulting from abbreviated calculations by means of the method presented in this paper. It is seen that the method of reference 1 gives acceptable results for the second mode (comparable to two to three Stodola and two to three sweeping operations), whereas results

* For reasons of simplicity, the bars will be omitted hereafter.

for the third mode are poor. In fact, the average error resulting from application of the method of reference 1 gives in the third mode an average error approximately 50 times that which would result from using the estimated and swept curve of the present method but with no Stodola iterations. For this reason, fourth mode calculations by means of the method of reference 1 have not been attempted.

TABLE 10

Comparison Between Present Method and That of Reference 1

Station	y_2^4	y_2^*	y_3^4	y_3^*
10	1.00000	1.00000	1.00000	1.00000
9	0.61068	0.60918	0.38107	0.31362
8	0.24790	0.24570	−0.10263	−0.12084
7	−0.02804	−0.02947	−0.27327	−0.22531
6	−0.19132	−0.19117	−0.18404	−0.12592
5	−0.25147	−0.24991	−0.00296	0.00377
4	−0.23894	−0.23668	0.13717	0.11828
3	−0.18261	−0.18047	0.18157	0.14297
2	−0.11025	−0.10879	0.14119	0.09722
1	−0.04340	−0.04278	0.06536	0.03833
0	0	0	0	0

$\Sigma(y_2^4 - y_2^*)^2 = 0.0000237942$ $\quad \Sigma(y_3^4 - y_3^*)^2 = 0.151152694$

$\Sigma(y_2^4 - y_2^3)^2 = 0.0000082542$ $\quad \Sigma(y_3^4 - y_3^3)^2 = 0.000001113$

$\Sigma(y_2^4 - y_2^2)^2 = 0.0003188165$ $\quad \Sigma(y_3^4 - y_3^1)^2 = 0.003619254$

y_2^* and y_3^* were found by means of the method of reference 1.

REFERENCES

[1] Boukidis, N. A., and Ruggiero, R., *An Iterative Method for Determining Dynamic Deflections and Frequencies*, Journal of the Aeronautical Sciences, Vol. II, No. 4, October, 1944.

[2] Prohl, M. A., *A General Method for Calculating Critical Speeds of Flexible Rotor*, Journal of Applied Mechanics, Vol. 12, No. 3, September, 1945.

[3] Myklestad, N. O., *A New Method of Calculating Natural Modes of Uncoupled Bending Vibrations of Airplane Wings and Other Types of Beams*, Journal of the Aeronautical Sciences, Vol. II, No. 2, April, 1944.

[4] Stodola, A., *Steam and Gas Turbines*, Vol. I, p. 449; Peter Smith, New York, 1945.

[5] Den Hartog, J. P., *Mechanical Vibrations;* McGraw-Hill Book Company, Inc., New York, 1940.

[6] Myklestad, N. O., *Vibration Analysis*, 1st. Ed., p. 140; McGraw-Hill Book Company, Inc., New York, 1944.

[7] Burgess, C. P., *The Frequencies of Cantilever Wings in Beam and Torsional Vibrations*, N.A.C.A. T.N. No. 746, 1940.

[8] Sokolnikoff, I. S., and Sokolnikoff, E. S., *Higher Mathematics for Engineers and Physicists*, 2nd Ed., p. 537; McGraw-Hill Book Company, Inc., New York, 1941.

[9] Biezeno, C. B., and Grammel, R., *Technische Dynamic*, Chap. X, p. 16; Julius Springer, Berlin, 1939.

The Effect of Radius of Curvature and Preliminary Artificial Eccentricities on Buckling Loads of Curved Thin Aluminum-Alloy Sheets for Monocoque Constructions

(*Continued from page 596*)

these special tests. On the contrary, it was found that the panels are not affected at all by these artificial eccentricities, and no sensitivity or weakness could be detected as a result of this sort of eccentricity.

RÉSUMÉ OF RESULTS

A series of tests on panels of various radii of curvature showed that these panels, which had been rolled to a smaller radius and tested with the usual radius of 24 in., had strikingly higher resistant qualities than panels of the usual shape. Between 8- and 14-in. radius, no buckling took place; the stress-strain diagram has a high elastic range and the collapse loads are distinctly superior to those of other panels with greater radii. These results have been confirmed by tests on panels made of pure aluminum.

Furthermore, it was possible to show that initial eccentricities of the panel, generally supposed to be the main cause of a low buckling load, are not at all serious if they remain localized in the sheets. Indentations with 10-mm. and 25-mm. steel balls did not affect the strength qualities of the panels against compression loads. Even holes produced by shooting 0.22-in. bullets through the panels did not decrease their normal buckling loads or their ultimate loads.

REFERENCES

[1] Welter, Georges, *Curved Aluminum-Alloy Sheets in Compression for Monocoque Constructions*, Journal of the Aeronautical Sciences, Vol. 12, No. 3, pp. 357–369, July, 1945.

[2] Welter, Georges, *Influence of Different Factors on Buckling Loads of Curved Thin Aluminum-Alloy Sheets for Monocoque Constructions*, Journal of the Aeronautical Sciences, Vol. 13 No. 4, pp. 204–213, April, 1946.

Vibrations of a Helicopter on the Ground

GABRIEL HORVAY*

McDonnell Aircraft Corporation

ABSTRACT

The present paper serves as an introduction to ground vibration analysis. Considerable insight may be gained of the phenomenon of ground vibrations, without actually going into the analysis of these somewhat complicated self-excited oscillations, by limiting one's attention to the much simpler problem—that of forced vibrations of the helicopter on the ground with the blade hinges locked. This preliminary study permits the determination of the natural modes of the helicopter, the ratios of the various amplitudes at resonance, and the magnitudes of the oscillations and of the blade unbalance forces at which shock-strut action sets in. The connection between the present study and ground vibration analysis is also taken up briefly, and a numerical example is given. Finally, the spring and damping constants of a tire-shock-strut combination are determined, and a discussion is given of the various constants of the shock absorber which play a role in ground vibrations.

INTRODUCTION

INSTABILITY CREATED by the interaction of a helicopter's rocking on the tires with the oscillations of the rotor blades about the lag hinges is known as ground vibration. In earlier construction of rotorcraft there were no lag hinges and no ground vibrations. However, rotor blades were subjected to large alternating chordwise bending moments, and breakages occurred.

To eliminate the large variations in the bending moments at the blade roots and to provide smoother performance, lag hinges came into use. The hinges provided much improvement, but the danger of ground instability also entered the picture. Many rotorcraft were destroyed on the ground because of the new kind of instability. The trouble was remedied by the introduction of lag motion dampers attached to the blades. The dampers eliminated ground vibrations, but they created fairly large bending moments at the blade roots, and the structural strength of the blades has again become a matter of serious concern. It is therefore important to know what is the least amount of blade damping that is adequate to prevent instability. Of course, this determination may be carried out experimentally and with safety for any given helicopter, as described by Deutsch in his recent paper.[1] The determination of the general effect of the various parameters of the helicopter—such as height of helicopter c.g., height of rotor, width of wheel base, eccentricity of lag hinge, coupling between lateral motion and rolling, etc.—upon the ground vibration characteristics is a study that requires a theoretical approach.

Coleman[2] was the first to compute the amount of blade damping required for a given helicopter on the basis of the following simplifying assumptions: (1) The rotor has three blades; (2a) H = height of helicopter c.g. above axle = 0; (2b) h = height of helicopter rotor above axle = 0; (3) flapping hinges are locked; (4) blades are rigid; (5a, b, c) pitching, rolling, yawing of the helicopter on the tires can be disregarded; (5d) vertical bouncing of the helicopter on the tires can be disregarded; (5e) gyroscopic effects can be disregarded; and (6) elasticity and damping exist only between the tires and ground and at the lag hinges.

Conditions 5a, b, d, and e really follow from conditions 2a and b. Since axle center, c.g., and rotor center coincide, no excitation of the pitching, rolling, and vertical modes takes place; therefore these modes may be omitted from consideration.

Coleman found the important result that, *when the product of blade damping and lateral landing gear damping exceeds a certain quantity, stability is obtained.*

The present paper is based on a study, recently undertaken at the McDonnell Aircraft Corporation under the sponsorship of the Bureau of Aeronautics, U.S. Navy, which aims at a more accurate determination of the required blade damping than was available heretofore. The restrictions 2, 3, and 5 of Coleman are discarded in that study, and assumption 6 is relaxed to include pylon bending modes.

Because of the extended length of the derivations, the above study cannot be presented within the scope of this paper. The most important result, the criterion for coupled lateral-rolling instability is given in the section "Comments on Ground Vibrations" without proof (proofs to the statements will be supplied in reference 3). Elsewhere the present investigation deals with the simplified problem where the lag and flapping hinges are locked, the forces of self-excitation are replaced by impressed forces, and the helicopter is considered as rigid except for the elasticity and the damping provided by the landing gears.†

DESCRIPTION OF THE HELICOPTER

In what follows it will be assumed that the helicopter is a twin-rotored side-by-side type (McDonnell-type)

Presented at the Rotating Wing Aircraft Session, Fourteenth Annual Meeting, I.A.S., New York, January 29–31, 1946.

* Research Engineer.

† The writer wishes to express his appreciation to his colleague, A. Gail, and to Lt. Comdr. L. Arnold, U.S.N.R., Bureau of Aeronautics, for helpful discussions.

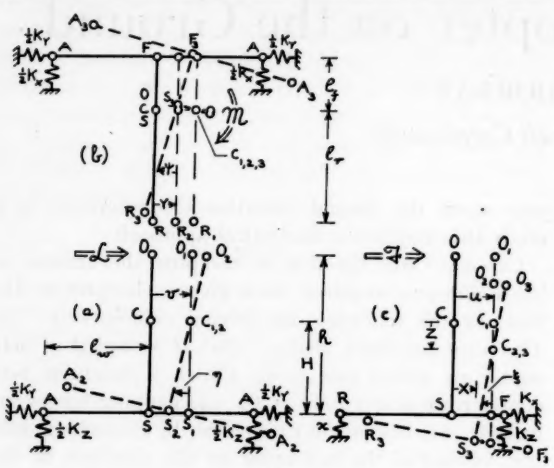

FIG. 1.

helicopter, with right rotor center at O_R, left rotor center at O_L at a distance $2L$ from O_R. L is the length of the pylon arm. The *rotor midpoint* (i.e., the midpoint of O_LO_R) at O is assumed to be directly above C, the c.g. of the helicopter.

For a single rotor helicopter O_R coincides with O, and there is no left rotor. Other changes necessary to adapt the present analysis to single rotor helicopters will be noted at the appropriate places.

Fig. 1a gives a schematic front view, Fig. 1b a schematic top view, and Fig. 1c a schematic side view of the helicopter. For the sake of simplicity, the rotor blades and the points O_R, O_L are omitted from the diagram, and only the rotor midpoint O is shown. A–A, of length $2l_w$, is the axle of the main landing gear, F its center. C is at height H, O at height h above the axle. The *vertical axis* OC pierces the horizontal plane through A–A at point S. F is at distance l_f forward of S, the rear axle R is at distance l_r aft of S. RSF can be called the *longitudinal axis*.

The center of gravity of the helicopter can be considered as the center of a coordinate system. Displacements with respect to C are denoted by u (forward), v (to starboard side), Z (downward).

The rigid body rotations of pitching ξ, rolling η, yawing ψ are defined as positive when O moves forward with respect to C (this is contrary to the usual definition), when O moves to the starboard with respect to C, and when RSF rotates clockwise about C as seen from above, respectively. It will be always assumed that the displacements u, v, Z and the rotations ξ, η, ψ are so small that their higher powers can be neglected.

Figs. 1a and 1b show the vertical axis OCS displaced sidewise by v into position $O_1C_1S_1$ and rotated by η into position $O_2C_2S_2$. The longitudinal axis RSF assumes the positions $R_1S_1F_1$ and $R_2S_2F_2$ in the course of these displacements. (Note that certain points, like S_1, O_2, etc., are indicated by small circles in Fig. 1b but are not labeled because of lack of space.) A yaw by angle ψ brings $R_2S_2F_2$ into the $R_3S_3F_3$ position. The axle A–A assumes at the same time the A_3–A_3 position.

Fig. 1c shows OCS moved forward by u into position $O_1C_1S_1$, downward by Z into position $O_2C_2S_2$, and rotated through angle ξ into position $O_3C_3S_3$.

Let W be the weight, $M = W/g$ the mass of the helicopter (blades included). Let I_ξ be the centroidal pitching moment of inertia, I_η the centroidal rolling moment of inertia, I_ψ the centroidal yawing moment of inertia of the helicopter. Let W', M', I_ξ', I_η', I_ψ' denote the above quantities when the helicopter is stripped of its blades. Naturally, in this case the moments of inertias must be referred to point C' (the c.g. of the helicopter when stripped of the blades), which is at height H' above the axle.

Let the rotor blades have the length R. This includes the lag hinge link length a. Let dm denote a mass element of the blade at distance r from the lag hinge. Then

$$m_B = \int_{a+r=0}^{R} dm, \quad m = \int_{r=0}^{R-a} dm \tag{1a}$$

are, respectively, the "total mass" and the "outboard mass" (i.e., the mass outboard of the lag hinge or, briefly, the "mass") of the rotor blade.

$$m_B B = \int_{a+r=0}^{R} (a + r)dm, \; m_B \rho_B^2 = \int_{a+r=0}^{R} (a + r)^2 dm \tag{1b}$$

$$mb = \int_{r=0}^{R-a} r dm, \; m\rho^2 = \int_{r=0}^{R-a} r^2 dm \tag{1c}$$

define the c.g. distance and the radius of gyration of the total blade with respect to the rotor center and of the outboard blade with respect to the lag hinge.

The important ratio (Coleman's Λ_1)

$$\epsilon = ab/\rho^2 \tag{2}$$

is to be noted. It may be called the *eccentricity parameter* of the lag hinge. ϵ plays a fundamental role in ground vibrations. Another numerical constant,

$$\delta = \mu b^2/2\rho^2 \tag{3a}$$

which can be called the *interference parameter*, likewise plays a fundamental role in ground vibrations. Here

$$\mu = 3m/M \tag{3b}$$

is the ratio of the outboard blade masses carried by a *single* rotor to the total helicopter mass (including the blades). (δ is Coleman's Λ_3 for single rotor helicopters and Coleman's $\Lambda_3/2$ for twin rotor helicopters.)

In place of the centroidal coordinate system u, v, Z it will be convenient to introduce a new coordinate system X, Y, Z, with origin at S, the intersection point of the vertical and longitudinal axes. The horizontal displacements in the two coordinate systems are related by

$$\left.\begin{aligned} X &= u - H\xi \\ Y &= v - H\eta \end{aligned}\right\} \tag{4}$$

while the vertical displacement Z is the same with respect to both systems. The pitching, rolling, and yawing moments of inertia of the helicopter with respect to S are

$$I_p = I_\xi + H^2M,\ I_r = I_\eta + H^2M,\ I_\psi \tag{5}$$

The numerical constants

$$\mu_\eta = 3m_B\rho_B{}^2/I_r,\ \mu_\xi = 3m_B\rho_B{}^2/I_p \tag{6}$$

(the *gyroscopic coupling parameters* of rolling and pitching) are of importance in the theory of the single rotor helicopter.

Let K_X, K_Y, K_Z denote the elasticities of the main landing gear in the X, Y and Z directions. K_Z is a combination of shock absorber elasticity K_s (which acts vertically) and vertical tire elasticity K_t. K_X and K_Y represent the longitudinal and lateral tire elasticities. Capital letters always refer to a pair of tires, or struts, or their combinations; the lower case letters k_X, k_Y, k_Z, k_t, k_s will be used to denote the constants of a single tire or strut, or a single tire-strut combination. Let the damping constants C_X, C_Y, C_Z C_t, C_s, c_X, c_Y, c_Z, c_t, c_s be defined similarly. The tail wheel exerts restraint only in the vertical direction. κ is the spring constant, γ the damping constant of the combined rear tire and strut.

Notations

Numbers in parentheses refer to the equations in which the quantities are introduced. Symbols introduced earlier are not repeated.

$\mathfrak{L}$, $\mathfrak{F}$ = lateral, longitudinal exciting force, Eq. (8)
$\mathfrak{M}$ = exciting moment for yawing
ω = rotor frequency, Eq. (9)
Ω = vibration frequency, Eq. (16)
D = d/dt, Eq. (11)
$D(\nu_j)$ = quantity defined in Eq. (29c)
D = (with various subscripts) displacement of shock absorber piston
d = as in d/dt
d = quantity defined in Eq. (38c)
d = depth of the center of oscillations, Eq. (44)
t = time
t = coefficient of coupling between lateral motion and rolling, Eq. (18b)
r = height ratio, Eq. (18a)
ν_X, ν_Y, ν_ξ, ν_η, ν_ψ = natural frequencies of the pure modes X, Y, ξ, η, ψ, Eqs. (12) and (14b) (the rotational modes are referred to S as center)
λ_X, λ_Y, etc. = extinction coefficients of the pure modes X, Y, etc., Eq. (12)
ν_Z, ν_t, ν_s, λ_Z, λ_t, λ_s = quantities defined in Eq. (14)
q = vertical frequency ratio, Eq. (22)
α = (lateral) frequency ratio, Eq. (22)
$\lambda_Y\%$ = percentage critical of the pure Y mode, Eq. (15)
E_X, E_Y, E_ξ, E_η = quantities defined in Eq. (11)
v_1, v_2 = quantities defined in Eq. (19)
$\Delta \equiv v_1 + iv_2$ = frequency determinant of the lateral-rolling motion, Eq. (19)
$\Delta_{\text{und.}}$ = frequency determinant of the undamped system, Eq. (20)
ν_1, ν_2 = natural frequencies of the coupled lateral-rolling mode, Eq. (21)
ω_1, ω_2 = critical rotor frequencies, Eq. (26)
λ_1, λ_2 = extinction coefficients of the ν_1, ν_2 modes, Eq. (38)
l_Y, l_η, u_Y, u_η = coefficients in Eq. (23)
e_1, e_2, e_3, e_4, Λ_1, Λ_2 = coefficients in Eq. (37)
c_b = damping constant of the blade damper
λ_b = blade extinction coefficient, Eq. (27)
ν_b = blade natural frequency, Eq. (32)
$\mathfrak{D}(\omega, \Omega) = 0$ = frequency equation of ground vibrations, Eq. (25)
λ_a = apparent extinction coefficient of landing gear, Eqs. (28) and (29)
L_Y, L_η, U_Y, U_η = coefficients in Eq. (29)
$\nu_{\eta-}$, $\nu_{\eta+}$ = gyroscopic splitting of the ν_η mode, Eqs. (35) and (36)
ν_{1-}, ν_{1+}, ν_{2-}, ν_{2+} = gyroscopic splitting of the ν_1, ν_2 modes
$Y_{\text{stat.}}$, $H\eta_{\text{stat.}}$ = static deflections, Eq. (41)
V = vertical force, Eq. (45)
$V_1 = V/2$, $W_1 = W/2$ = quantities used in the section on "Constants of the Shock Absorber"
V^*, Y^*, $H\eta^*$, $\mathfrak{L}^*$ = limiting values at which shock-strut action sets in, Eqs. (46) and (47)
f = coefficient of packing friction of shock absorber, Eq. (61c)
A = piston area, Eq. (53)
P = period, Eq. (60)
v = (with various subscripts) air volume in strut
p = (with various subscripts) air pressure in strut

Tire Modes of the Helicopter

Rotor Stationary

A lateral displacement v of the helicopter c.g. and a roll by angle η about the c.g. produce certain tire reactions. A lateral landing gear spring force $K_Y(v - H\eta)$ opposes the sidewise displacement $v - H\eta$ of the axle A–A. The roll η of A–A is supported by the moment $HK_Y(v - H\eta)$ of the lateral spring force and is opposed by the moment $l_wK_Zl_w\eta$ of the vertical spring force. If $\mathfrak{L}$ denotes the lateral exciting force which acts at rotor height, then

$$\left.\begin{aligned} v:&\ M\ddot{v} + K_Y(v - H\eta) = \mathfrak{L} \\ \eta:&\ I_\eta\ddot{\eta} - HK_Y(v - H\eta) + K_Zl_w{}^2\eta = (h - H)\mathfrak{L} \end{aligned}\right\} \tag{7}$$

are the equations of motion of the system. By Eqs. (4) and (5) the equations can also be written in the form

$$\left.\begin{aligned} Y:&\ M\ddot{Y} + K_YY + MH\ddot{\eta} = \mathfrak{L} \\ \eta:&\ HM\ddot{Y} + I_r\ddot{\eta} + K_Zl_w{}^2\eta = h\mathfrak{L} \end{aligned}\right\} \tag{8a}$$

Selection of the centroidal coordinate system u, v, Z implies static coupling between lateral motion and roll. Selection of the coordinate system X, Y, Z with origin at S replaces the static coupling by dynamic coupling. This is a distinct advantage in the present study because it permits separation of the lateral and vertical spring effects of the landing gears.

A forward displacement u of the helicopter c.g. and a pitching by angle ξ about the c.g. produces the fore-and-aft tire reaction $K_X(u - H\xi)$ which opposes the

forward motion, the moment $HK_X(u - H\xi)$ of the fore-and-aft tire reaction which aids, and the moment $l_f K_Z l_f \xi + l_r \kappa l_r \xi$ of the vertical landing gear reaction which opposes the pitching ξ. If $\mathfrak{F}$ denotes the longitudinal exciting force that acts at rotor height, then

$$\left.\begin{aligned} X:&\quad M\ddot{X} + K_X X + MH\ddot{\xi} = \mathfrak{F} \\ \xi:&\quad HM\ddot{X} + I_p\ddot{\xi} + (K_Z l_f^2 + \kappa l_r^2)\xi = h\mathfrak{F} \end{aligned}\right\} \quad (8b)$$

are the longitudinal-pitching equations of motion of the helicopter referred to the S-coordinate system.

For simultaneous excitation by the forces $\mathfrak{L}$ and $\mathfrak{F}$ the equations of motion, Eqs. (8a) and (8b), hold simultaneously, and there is no intercoupling between the lateral and the forward motions.

Rotor Revolving, Blade Hinges Locked

Consider now a single three-bladed rotor with center at O, revolving at angular speed ω in a clockwise sense (sense of $\mathfrak{M}$, Fig. 1). The centrifugal forces of the three blades cancel out. The Coriolis forces

$$+2\omega(a + r)dm\dot{\eta} \cos \omega t; \quad -2\omega(a + r)dm\dot{\xi} \sin \omega t \quad (9a)$$

which act on the blade element dm at the azimuth ωt as measured from the downwind position, the first pointing down, the second up, create a pitching moment

$$2\omega(a + r)^2 dm \cos \omega t(-\dot{\eta} \cos \omega t + \dot{\xi} \sin \omega t) \quad (9b)$$

and a rolling moment

$$2\omega(a + r)^2 dm \sin \omega t(-\dot{\eta} \cos \omega t + \dot{\xi} \sin \omega t) \quad (9c)$$

Integrating over the blade, cf. Eq. (1b), and summing for the three blades, one obtains $-3m_B\rho_B{}^2\omega\dot{\eta}$ and $+3m_B\rho_B{}^2\omega\dot{\xi}$ for the two impressed gyroscopic moments.

Taking also landing gear damping into account, the *equations of motion of the single rotor helicopter on ground, with rotor revolving but blade hinges locked* now assume the form

$$X: \quad ME_X(D)X + MD^2H\xi = \mathfrak{F} \quad (10a)$$

$$\xi: \quad HMD^2X + I_p E_\xi(D)\xi + I_p\mu_\xi\omega D\eta = h\mathfrak{F} \quad (10b)$$

$$Y: \quad ME_Y(D)X + MD^2H\eta = \mathfrak{L} \quad (10c)$$

$$\eta: \quad HMD^2Y + I_r E_\eta(D)\eta - I_r\mu_\eta\omega D\xi = h\mathfrak{L} \quad (10d)$$

where μ_ξ, μ_η were given in Eq. (6)

$$\left.\begin{aligned} D &= d/dt \\ E_X(D) &= D^2 + \lambda_X D + \nu_X{}^2 \end{aligned}\right\} \quad (11)$$

and E_Y, E_ξ, E_η are obtained from E_X by changing the subscripts X to Y, ξ, and η.

The quantities

$$\left.\begin{aligned} \nu_X{}^2 &= K_X/M, \ \nu_Y{}^2 = K_Y/M \\ \nu_\xi{}^2 &= (K_Z l_f^2 + \kappa l_r^2)/I_p, \ \nu_\eta{}^2 = K_Z l_w^2/I_r \end{aligned}\right\} \quad (12a)$$

are the squared *natural frequencies* of the pure X, pure Y, and (keeping S fixed) pure ξ and pure η modes. (Note that the centroidal rolling frequency, keeping C fixed, is

$$\nu_{\eta,\,\text{centroid}} = \sqrt{(K_Z l_w^2 + K_Y H^2)/I_\eta} \quad (13)$$

It depends on both the Z and the Y elasticities of the landing gear.) Similarly,

$$\left.\begin{aligned} \lambda_X &= C_X/M, \ \lambda_Y = C_Y/M \\ \lambda_\xi &= (C_Z l_f^2 + \gamma l_r^2)/I_p, \ \lambda_\eta = C_Z l_w^2/I_r \end{aligned}\right\} \quad (12b)$$

are the *extinction coefficients* (or briefly, the "damping") of the above modes.

For twin rotor helicopters with two identical rotors the gyroscopic terms cancel out because of the reversal of the sign of ω for the second rotor. The equations of motion split into two groups: the modes of X, ξ and the modes of Y, η. Thus, *the equations of motion of the twin rotor helicopter on ground, with rotors revolving but blade hinges locked, are obtained from Eqs. (10) by omitting the gyroscopic coupling terms* and were given earlier, except for the damping terms, in Eqs. (8a) and (8b). For single rotor helicopters the gyroscopic interactions produce a coupling between ξ and η, and the modes X, ξ and Y, η are no longer independent.

When the lag hinges are unlocked, blade oscillations in the lag plane take place. These oscillations interact with the X, ξ, Y, η vibrations of the helicopter. It is found that the equations that govern the helicopter vibrations are still Eqs. (10). (Omit the μ_ξ, μ_η terms for twin rotor helicopters.) But $\mathfrak{L}$ must now be identified with the lateral and $\mathfrak{F}$ with the longitudinal whipping forces of the hinged blades. Evidently, the blade unbalance forces also create an unbalance yawing moment $\mathfrak{N}$ and thus excite yawing vibrations ψ of the helicopter. Less directly, vertical oscillations Z of the helicopter are also excited. It will be shown in reference 3 that the Z motion is usually unimportant, while the ψ motion is unimportant only when l_f and L are small.

Considerable simplifications and symmetry are achieved in the theory by restricting the degrees of freedom to the X, ξ, Y, η motions. This plan is followed in the present paper.

For the sake of completeness the following quantities, used in subsequent sections, are also defined at this place.

$$\nu_Z{}^2 = K_Z/M, \ \nu_s{}^2 = K_s/M, \ \nu_t{}^2 = K_t/M \quad (14a)$$

are the squared vertical natural frequencies of the helicopter on the front landing gears, on the front shock absorbers alone, and on the front tires alone. The extinction coefficients λ_Z, λ_s, λ_t are defined similarly.

$$\nu_\psi{}^2 = (K_X l_w^2 + K_Y l_f^2)/I_\psi \quad (14b)$$

is the squared yawing natural frequency of the heli-

copter when the point S (or C) is kept fixed. The extinction coefficient λ_ψ is defined similarly.

The notation

$$(1/100)\lambda_Y\% = \lambda_Y/2\nu_Y = C_Y\nu_Y/2K_Y = 0.06 \quad (15)$$

will be used to indicate that the Y mode has a 6 per cent critical damping.

Coupling Between Lateral Oscillations and Rolling

Natural Frequencies of the Twin Rotor Helicopter

Eqs. (10), with the gyroscopic interaction terms μ_ξ, μ_η omitted, govern the motion of the twin rotor helicopter. The X, ξ equations are of the same form as the Y, η equations. Thus, for an understanding of the response of the system it suffices to investigate the Y, η motion.

For a harmonic excitation

$$\mathfrak{L}(t) = \mathfrak{L}e^{i\Omega t} \quad (16a)$$

the responses are also harmonic

$$Y(t) = Ye^{i\Omega t},\ H\eta(t) = H\eta e^{i\Omega t} \quad (16b)$$

and Eqs. (10c) and (10d), with μ_η omitted, reduce to

$$Y: \quad (\nu_Y^2 - \Omega^2 + i\Omega\lambda_Y)Y - \Omega^2 H\eta = \mathfrak{L}/M \quad (17a)$$

$$H\eta: \quad -t\Omega^2 Y + (\nu_\eta^2 - \Omega^2 + i\Omega\lambda_\eta)H\eta = rt\mathfrak{L}/M \quad (17b)$$

Here

$$r = h/H \quad (18a)$$

is the *height ratio* of rotor and c.g. (referred to axle as base);

$$t = MH^2/I_x \quad (18b)$$

is the *coefficient of coupling* between lateral and rolling motion.

The system is in a natural mode if the determinantal equation of Eqs. (17) vanishes:

$$\Delta \equiv v_1 + iv_2 = 0 \quad (19a)$$

where

$$v_1 \equiv \Omega^4(1 - t) - \Omega^2(\nu_Y^2 + \nu_\eta^2 + \lambda_Y\lambda_\eta) + \nu_Y^2\nu_\eta^2 \quad (19b)$$

$$v_2 \equiv \Omega[\lambda_\eta(\nu_Y^2 - \Omega^2) + \lambda_Y(\nu_\eta^2 - \Omega^2)] \quad (19c)$$

The roots of the damped equation $\Delta = 0$ are given (accurately, to the extent that second order small terms in λ_Y and λ_η are negligible) by the roots ν_1 and ν of the undamped equation

$$\Delta_{\text{und.}} \equiv (\nu_Y^2 - \Omega^2)(\nu_\eta^2 - \Omega^2) - t\Omega^4 = (1 - t) \times (\Omega^2 - \nu_1^2)(\Omega^2 - \nu_2^2) = 0 \quad (20)$$

One obtains

$$\nu^2_{1,2} = \left[\frac{1 + \alpha^2 \pm \sqrt{(1 - \alpha^2)^2 + 4t\alpha^2}}{2(1 - t)}\right]\nu_Y^2 \quad (21)$$

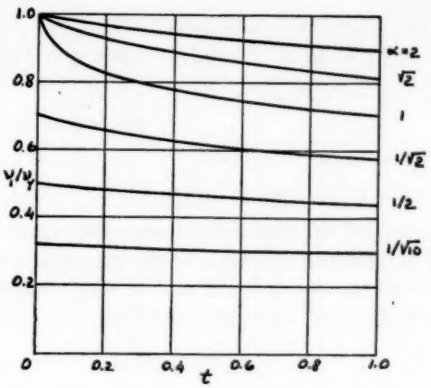

FIG. 2a.

where subscript 1 refers to the lower root, subscript 2 refers to the upper root, and

$$\alpha = \nu_\eta/\nu_Y \quad (22a)$$

is the lateral frequency ratio, or briefly, the *frequency ratio* of the system. α is related to the *vertical frequency ratio*

$$\nu_\eta/\nu_Z = q = l_w\sqrt{t}/H = \sqrt{\lambda_\eta/\lambda_Z} = \lambda_\eta\%/\lambda_Z\% \quad (22b)$$

by

$$\alpha = q\sqrt{K_Z/K_Y} \quad (22c)$$

The natural frequencies ν_1 and ν_2 are independent of the height ratio r. ν_1 and ν_2 are plotted in Fig. 2 for $\alpha = 2, \sqrt{2}, 1, \sqrt{1/2}, 1/2$, when t varies from 0 to 1. For very small coupling, $t \sim 0$, the frequencies

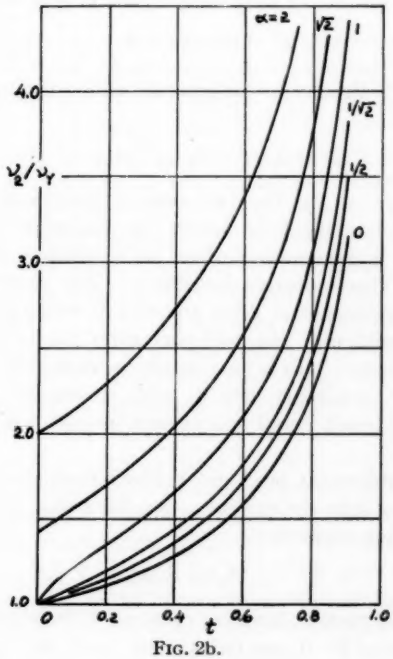

FIG. 2b.

$$\left.\begin{aligned} \nu_1^2 &= \{1 - [t\alpha^2/(1-\alpha^2)]\}\alpha^2\nu_Y^2, \\ \nu_2^2 &= \{1 + [t/(1-\alpha^2)]\}\nu_Y^2 \text{ (when } \alpha < 1) \\ \nu_1^2 &= \nu_Y^2/(1+\sqrt{t}),\ \nu_2^2 = \nu_Y^2/(1-\sqrt{t}) \\ &\qquad \text{(when } \alpha = 1) \\ \nu_1^2 &= \{1 - [t/(\alpha^2-1)]\}\nu_Y^2, \\ \nu_2^2 &= \{1 + [t\alpha^2/(\alpha^2-1)]\}\nu_Y \text{ (when } \alpha > 1) \end{aligned}\right\} \quad (23)$$

are essentially the uncoupled frequencies ν_Y and ν_η of lateral motion and rolling. As the coupling increases, ν_1 becomes somewhat lower and ν_2 much higher. In the limit of $t \to \infty$ (complete coupling)

$$\nu_2 \to \infty \quad (24a)$$

and

$$\nu_1 \to \alpha\nu_Y/\sqrt{1+\alpha^2} \quad (24b)$$

is the only natural frequency of the system.

Comments on Ground Vibrations

Without going into derivations or proofs, some comments about the application of the present theory to ground vibrations seems to be in order at this point.

Eqs. (10) govern the oscillations of the helicopter also in the case when the rotor blades are free to oscillate about the lag hinges. But the exciting forces $\mathfrak{F}$ and $\mathfrak{L}$, which represent the blade unbalance forces, are now created by the oscillations X, ξ, Y, η themselves. This fact can be expressed by a second set of equations between X, ξ, Y, η and $\mathfrak{F}, \mathfrak{L}$; the phenomenon is one of self-excitation. As a result, the frequency of vibration Ω, which is the same as the frequency of excitation by $\mathfrak{F}$ and $\mathfrak{L}$, cannot be arbitrary; Ω is a prescribed function of the rotor frequency ω. This functional relation assumes the form of a *frequency equation*

$$\mathfrak{D}(\omega, \Omega) = 0 \quad (25)$$

One finds that for rotor speeds near the so-called critical speeds

$$\omega_j = \nu_j/(1-\sqrt{\epsilon}) \quad (j = 1, 2) \quad (26)$$

where ν_1, ν_2 are the two natural frequencies of the coupled lateral-rolling motion, the oscillation frequency Ω of an undamped helicopter has a negative imaginary part. This indicates instability. The magnitude of the imaginary part gives the rate at which the oscillations build up; the real part gives the frequency of oscillations. This is very nearly ν_j, indicating that the gravest instability sets in with a frequency that is approximately equal to a natural frequency of the helicopter.

Instability can be eliminated by introducing sufficient damping into the system. One finds that if the blade extinction coefficient

$$\lambda_b = c_b/m\rho^2 \quad (27)$$

(c_b is the viscous damping constant of the blade damper in units of lb. ft. per rad. per sec.) and the "apparent" landing gear extinction coefficient λ_a have a sufficiently large product

$$\lambda_b\lambda_a \geqslant \delta\nu_Y^2(1-\sqrt{\epsilon})/\sqrt{\epsilon} \quad (28)$$

then stability is ensured. Here λ_a, *the apparent extinction coefficient of the landing gear, is a linear combination of* λ_Y *and* λ_η:

$$\lambda_a = L_Y\lambda_Y + L_\eta\lambda_\eta \text{ (in the lower mode } \nu_1) \quad (29a)$$

$$\lambda_a = U_Y\lambda_Y + U_\eta\lambda_\eta \text{ (in the upper mode } \nu_2) \quad (29b)$$

where

$$\left.\begin{aligned} L_Y &\equiv [\alpha^2(\nu_Y^2/\nu_1^2) - 1]/D(\nu_1) \\ L_\eta &\equiv [(\nu_Y^2/\nu_1^2) - 1]/D(\nu_1) \\ D(\nu_1) &\equiv \alpha^2 + tr^2 - (1 + tr^2 - 2tr)\nu_1^2/\nu_Y^2 \end{aligned}\right\} \quad (29c)$$

and U_Y, U_η, $D(\nu_2)$ are obtained from L_Y, L_η, $D(\nu_1)$ by replacing ν_1 by ν_2 in the above expressions. The eccentricity parameter ϵ and the interference parameter δ were defined earlier in Eqs. (2) and (3).

For $\alpha > 1$, $t = 0$ (rolling has a higher natural frequency than the lateral motion and is uncoupled) or for $\alpha = \infty$ ($K_Z = \infty$, *pure lateral mode*), Eq. (29a) reduces to $\lambda_a = \lambda_Y$, and (28) reduces to the well-known *stability criterion of Coleman*

$$\lambda_b\lambda_Y \geqslant \delta\nu_Y^2/(1-\sqrt{\epsilon})/\sqrt{\epsilon} \quad (30a)$$

which can also be written in the form

$$(c_b/m\rho^2)(C_Y/K_Y) \geqslant \delta(1-\sqrt{\epsilon})/\sqrt{\epsilon} \quad (30b)$$

(Note that Eq. (30) is a special case of Coleman's more general formula when k_b = blade centering spring stiff-

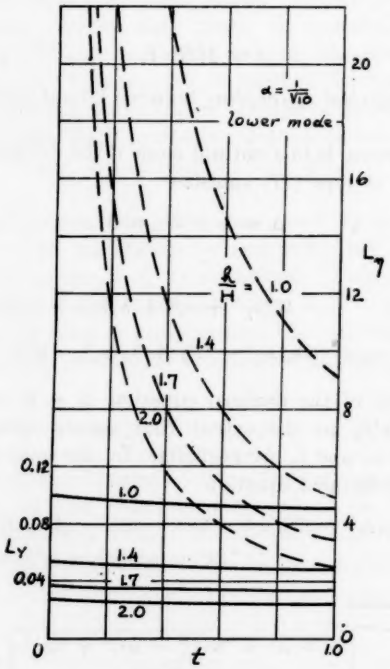

FIG. 3a.

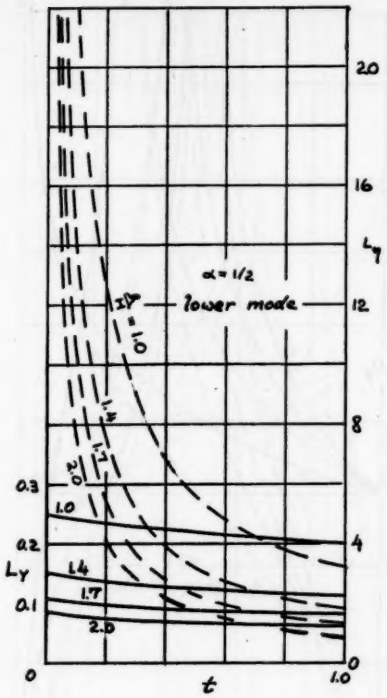

FIG. 3b.

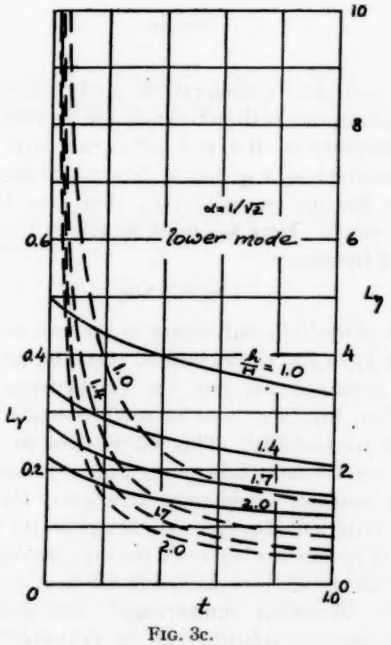

FIG. 3c.

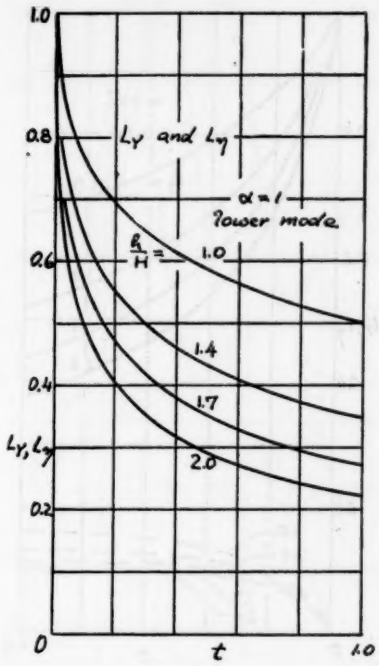

FIG. 3d.

ness = 0. The effect of blade centering springs is omitted in the present analysis for convenience. Blade flexibility can be taken into account in an approximate way by determining an effective lag hinge position as the intersection of the unflexed blade and a mean secant of the flexed blade. This increases the value of ϵ.)

For $\alpha = 0$ ($K_Y = \infty$, *pure rolling mode*), formulas (28) and (29) reduce to

$$\lambda_b\lambda_\eta \gtrless tr^2\delta\nu_\eta^2(1 - \sqrt{\epsilon})/\sqrt{\epsilon} \tag{31a}$$

which can also be written in the form

$$\left(\frac{c_b}{m\rho^2}\right)\left(\frac{C_Z}{K_Z}\right)\left(\frac{I_r}{Mh^2}\right) \gtrless \delta\frac{1 - \sqrt{\epsilon}}{\sqrt{\epsilon}} \tag{31b}$$

From (31) it is evident that *a large rolling moment of inertia I_r, as provided by twin rotor helicopters with long pylon arms, is advantageous in ground vibrations.* However it must be remembered that in such a case the excitation of the yawing mode ψ is no longer negligible. When the distance l_f of the c.g. behind the axle center is sufficiently short and the brakes are off ($K_X = 0$), then the yawing frequency ν_ψ is sufficiently low so that its effect on ground vibrations can be disregarded.

The curves of L_Y and L_η are plotted in Figs. 3a–3f vs. t and r for $\alpha = 1/\sqrt{10}$, $1/2$, $\sqrt{1/2}$, 1, $\sqrt{2}$, 2. The curves of U_Y and U_η are plotted in Figs. 4a–4d vs. t and r for $\alpha = 0$, $1/2$, 1, 2. It is found that a large value of the height ratio r is detrimental in the lower and usually favorable in the upper mode. Since, however, the lowest mode is almost always the most critical mode, large r is undesirable in ground vibrations. For a large frequency ratio α most of the excitation goes (at ν_1) into the slightly damped lateral mode ν_Y; for small α and small coupling t most of the excitation goes into the rolling mode ν_η, which is greatly damped by shock absorber action. Small α and small t are therefore desirable conditions in ground vibrations. They are best

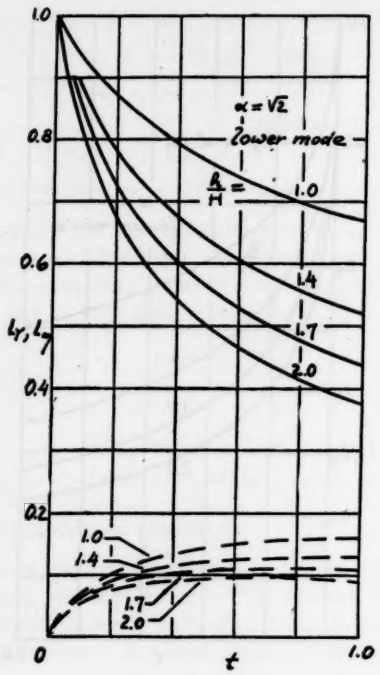

FIG. 3e.

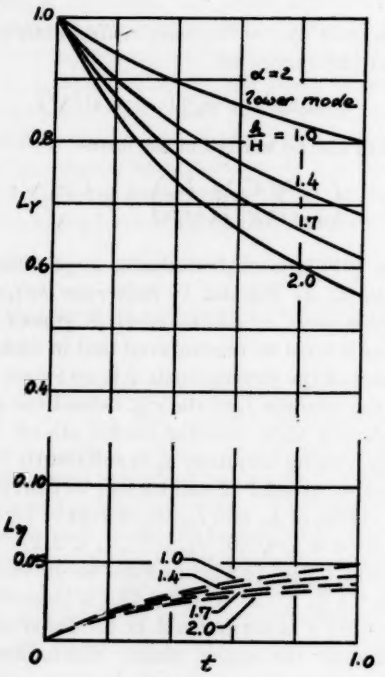

FIG. 3f.

achieved by twin rotor helicopters with long pylon arms. Naturally, the interference δ should be as small, the lag hinge eccentricity ϵ as large, and the natural frequency ν_1 as small as permitted by other design considerations.

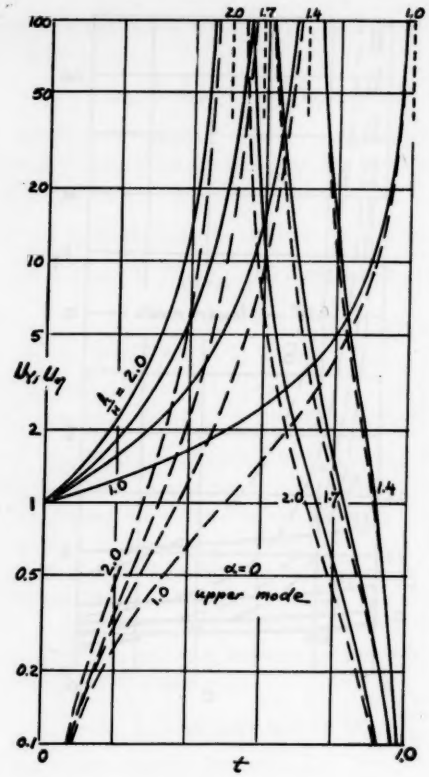

FIG. 4a.

The preceding considerations apply strictly to twin rotor helicopters with sufficiently low yawing frequency ν_ψ, sufficiently small δ, and sufficiently large ϵ, so that the required $\lambda_{Y\%}, \lambda_{\eta\%}, \lambda_{b\%}$, as determined from Eq. (28) do not become excessive (i.e., they stay below, say, 35 per cent). Here $\lambda_{b\%}$ must be referred to the blade natural frequency

$$\nu_b = \omega\sqrt{\epsilon} \tag{32}$$

and thus has different values in the two modes ν_1 and ν_2. If λ_Y, λ_η, λ_b are excessive, then the criterion, Eq. (28), breaks down, and the cumbersome frequency equation, Eq. (25), must be used to establish the conditions for stability. This will be done in reference 3. However, for most helicopters Eq. (28) is adequate.

For isotropic single rotor helicopters the same stability criterion, Eq. (28), applies provided the expressions of ν_η, ν_1, ν_2 are corrected for the *gyroscopic splitting*. This calculation is explained in the next section, and is usually somewhat cumbersome. For most purposes the gyroscopic splitting can be neglected; then Eq. (28) and Figs. 3 and 4 apply directly to the isotropic single rotor helicopter.

Natural Frequencies of the Isotropic Single Rotor Helicopter

The methods of the preceding sections apply immediately to the cases $K_z = \infty$ and $\nu_Y/\nu_X = 0$ or ∞ of

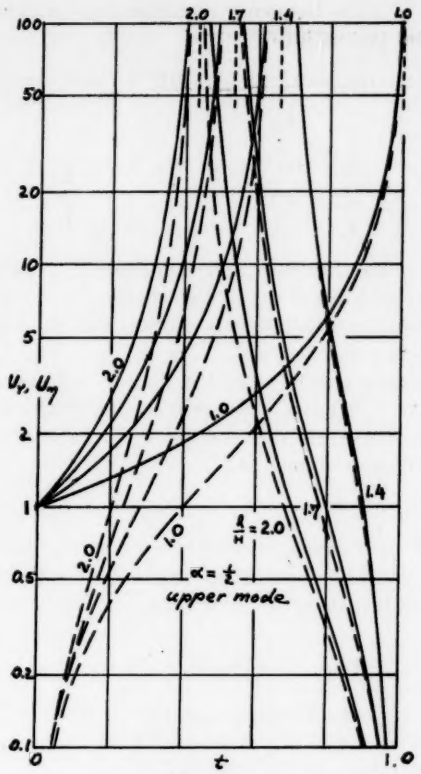

FIG. 4b.

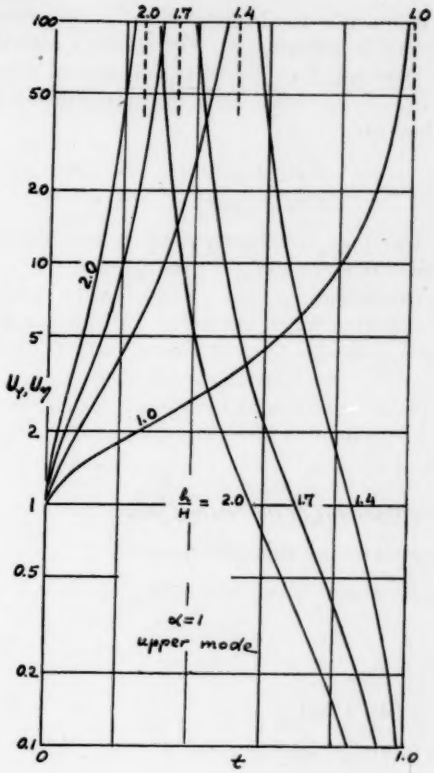

FIG. 4c.

the single rotor helicopter. In the present section the equally important special case of isotropic symmetry

$$\nu_X = \nu_Y,\ \nu_\xi = \nu_\eta,\ \lambda_X = \lambda_Y,\ \lambda_\xi = \lambda_\eta,\ \mu_\xi = \mu_\eta \tag{34a}$$

is considered. The equations of motion, Eqs. (10), now become

$$\left.\begin{aligned} X \pm iY\colon\ & [D^2 + \lambda_Y D + \nu_Y{}^2](X \pm iY) + \\ & D^2 H(\xi \pm i\eta) = (\mathfrak{F} \pm i\mathfrak{L})/M \\ H(\xi \pm i\eta)\colon\ & tD^2(X \pm iY) + [D^2 + \lambda_\eta D + \\ & \nu_\eta{}^2 \mp \mu_\eta \omega i D] H(\xi \pm i\eta) = tr(\mathfrak{F} \pm i\mathfrak{L})/M \end{aligned}\right\} \tag{34b}$$

and can be brought to the form of Eqs. (17), provided one writes

$$\left.\begin{aligned} \nu_{\eta+}{}^2 &= \nu_\eta{}^2 + \mu_\eta \omega\Omega \\ \nu_{\eta-}{}^2 &= \nu_\eta{}^2 - \mu_\eta \omega\Omega \end{aligned}\right\} \tag{35}$$

in place of $\nu_\eta{}^2$. Thus, because of gyroscopic interaction between rolling and pitching, ν_η splits into two frequencies, $\nu_{\eta-}$ and $\nu_{\eta+}$, which are quite close to each other since μ_η is small. Correspondingly, the natural frequencies ν_1 and ν_2, obtained from Eq. (20), also split into the two closely adjoining frequencies ν_{1-}, ν_{1+} and ν_{2-}, ν_{2+}, respectively. Unfortunately, $\nu_{\eta-}$ and $\nu_{\eta+}$ depend on both the rotor frequency ω and on the vibration frequency Ω. For a given rotor speed ω the frequency equation, Eq. (25), can be solved for Ω, and then the

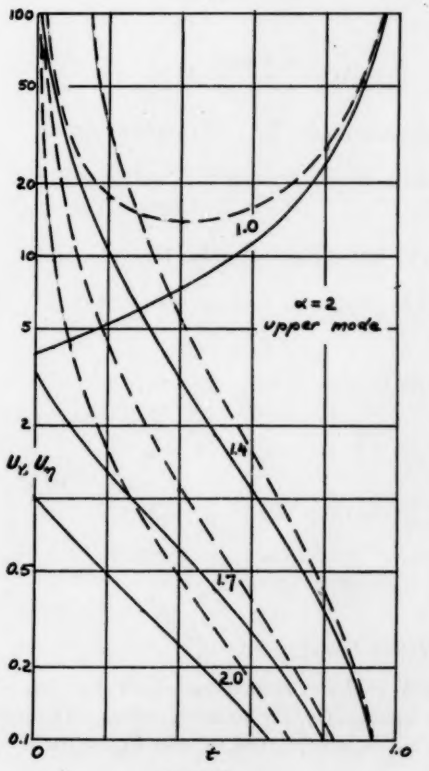

FIG. 4d.

values in Eq. (35) can be determined. This procedure is indicated in reference 3. For stability calculations by the criterion, Eq. (28), it is sufficient to know the values of $\nu_{\eta+}{}^2$, $\nu_{\eta-}{}^2$ assumed at the critical speeds ω_1 and ω_2. These are

$$\left.\begin{aligned}\nu_{\eta+}{}^2 &= \nu_\eta{}^2 + \mu_\eta\nu_1{}^2/(1-\sqrt{\epsilon})\\ \nu_{\eta-}{}^2 &= \nu_\eta{}^2 - \mu_\eta\nu_1{}^2/(1-\sqrt{\epsilon})\end{aligned}\right\} \tag{36}$$

at the speed ω_1. Replacing ν_1 by ν_2, one obtains the expressions of $\nu_{\eta+}{}^2$ and $\nu_{\eta-}{}^2$ at the speed ω_2.

The frequencies $\nu_{\eta+}$ and ν_{1+} can now be determined in the following way: Solve Eq. (20) for ν_1 using the approximation $\nu_{\eta+} = \nu_\eta$, and then, from Eq. (36), determine $\nu_{\eta+}$. Replaced into Eq. (20), this yields a value for ν_{1+}. One such iteration is usually sufficient since μ_η is small. The determination of the pairs $\{\nu_{\eta-}, \nu_{1-}\}$, $\{\nu_{\eta+}, \nu_{2+}\}$, and $\{\nu_{\eta-}, \nu_{2-}\}$ is similar.

Effective Damping of the Normal Modes

It is well known that the equation

$$\Omega^4 + e_1\Omega^3 + e_2\Omega^2 + e_3\Omega + e_4 = 0 \qquad (e_1{}^2 \sim e_3{}^2 \sim 0) \tag{37a}$$

factors into

$$(\Omega^2 - \Lambda_1\Omega - \nu_1{}^2)(\Omega^2 - \Lambda_2\Omega - \nu_2{}^2) = 0 \tag{37b}$$

where $\nu_1{}^2$ and $\nu_2{}^2$ are the roots of

$$\Omega^4 + e_2\Omega^2 + e_4 = 0 \tag{37c}$$

and

$$\Lambda_1 = \frac{e_3 + e_1\nu_1{}^2}{\nu_2{}^2 - \nu_1{}^2},\ \Lambda_2 = \frac{e_3 + e_1\nu_2{}^2}{\nu_1{}^2 - \nu^2} \tag{37d}$$

Correspondingly, Eq. (19a) factors into

$$\Delta = v_1 + iv_2 = (1-t)(\Omega^2 - i\lambda_1\Omega - \nu_1{}^2) \times (\Omega^2 - i\lambda_2\Omega - \nu_2{}^2) \tag{38a}$$

where $\nu_1{}^2$ and $\nu_2{}^2$ are given by Eq. (21), and

$$\lambda_1 = l_Y\lambda_Y + l_\eta\lambda_\eta,\ \lambda_2 = u_Y\lambda_Y + u_\eta\lambda_\eta \tag{38b}$$

with

$$\left.\begin{aligned} l_Y &= [(1-t)(\nu_2{}^2 - \nu_1{}^2) - 1 - \alpha^2 + 2(1-t)\alpha^2]/d\\ l_\eta &= [(1-t)(\nu_2{}^2 - \nu_1{}^2) - 1 - \alpha^2 + 2(1-t)]/d\\ u_Y &= [(1-t)(\nu_2{}^2 - \nu_1{}^2) + 1 + \alpha^2 - 2(1-t)\alpha^2]/d\\ u_\eta &= [(1-t)(\nu_2{}^2 - \nu_1{}^2) + 1 + \alpha^2 - 2(1-t)]/d\\ d &= 2(1-t)^2(\nu_2{}^2 - \nu_1{}^2)\end{aligned}\right\} \tag{38c}$$

λ_1 and λ_2 are the extinction coefficients of the free vibrations of the lower and upper modes ν_1 and ν_2. The coefficients l_Y, l_η, u_Y, u_η are plotted vs. t in Fig. 5 for $\alpha = {}^1/_2$, 1, and 2.

For $t = 1$ the frequency equation degenerates into a cubic and factors into

$$\Delta = -i(\lambda_\eta + \lambda_Y)(\Omega - i\lambda_2)(\Omega^2 - i\lambda_1\Omega - \nu_1{}^2) \tag{39a}$$

where

$$\left.\begin{aligned}\lambda_2 &= (\nu_Y{}^2 + \nu_\eta{}^2)/(\lambda_Y + \lambda_\eta)\\ \nu_1{}^2 &= \alpha^2\nu_Y{}^2/(1+\alpha^2)\\ \lambda_1 &= (\alpha^4\lambda_Y + \lambda_\eta)/(1+\alpha^2)^2\end{aligned}\right\} \tag{39b}$$

There is now only one oscillating mode, ν_1. This is associated with the extinction coefficient, λ_1. The other mode represents an aperiodic motion with the very high extinction coefficient, λ_2.

It is interesting to note that the coupled system $\alpha = t = 1$, $\lambda_Y = \lambda_\eta$ has a 50 per cent smaller effective damping than has either the mode ν_Y or the mode ν_η. From Eq. (39) one obtains

$$\lambda_1 = {}^1/_4\lambda_Y + {}^1/_4\lambda_\eta = {}^1/_2\lambda_Y \tag{40a}$$

Part of the decrease is compensated by the decrease in frequency; the percentage critical in mode ν_1 is 29 per cent less than the percentage critical for either λ_Y or ν_η:

$$\lambda_1/2\nu_1 = \lambda_Y/\sqrt{8}\nu_Y = \lambda_\eta/\sqrt{8}\nu_\eta \tag{40b}$$

The effective damping constants λ_1, λ_2 of the present section are not to be confused with the apparent damping constant λ_a of Eq. (29).

Resonance Magnification. Amplitude Ratio. Center of Oscillations

From Eqs. (17a) and (17b) it follows that, at any forced frequency Ω,

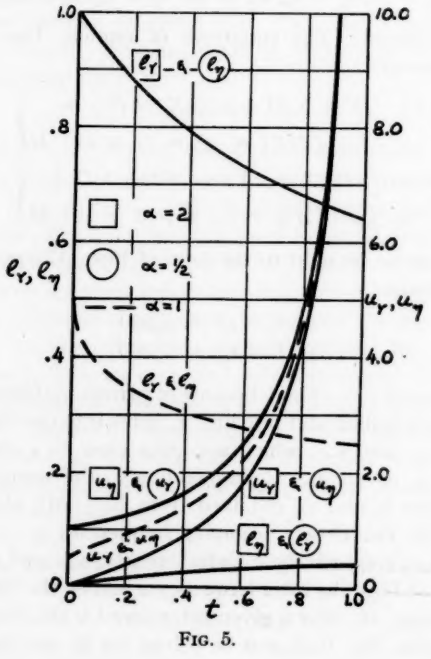

FIG. 5.

$$Y(\Omega) = \left\{ \frac{[\nu_\eta^2 - (1 - tr)\Omega^2 + i\Omega\lambda_\eta]}{\nu_1 + i\nu_2} \right\} \frac{\mathfrak{L}}{M} = \left\{ \quad \right\} \nu_Y^2 Y_{\text{stat.}} \quad (41a)$$

is the vibration amplitude of the c.g. displacement due to lateral motion, and

$$H\eta(\Omega) = \left\{ \frac{\nu_Y^2 - [1 - (1/r)]\Omega^2 + i\Omega\lambda_Y}{\nu_1 + i\nu_2} \right\} tr \frac{\mathfrak{L}}{M} = \left\{ \quad \right\} \nu_\eta^2 H\eta_{\text{stat.}} \quad (41b)$$

is the amplitude of the c.g. displacement due to roll. Noting that $\lambda_Y^2 \sim \lambda_\eta^2 \sim 0$ and that $\nu_1 = 0$ at the resonance frequency ν_1,

$$Y(\nu_1)/Y_{\text{stat.}} \simeq \nu_Y^2[(tr - 1)\nu_1^2 + \nu_\eta^2]/i\nu_2(\nu_1) \quad \text{(resonance)} \quad (42a)$$

and a similar formula, Eq. (42b), holds for $H\eta(\nu_1)/H\eta_{\text{stat}}$. Evidently, a large height ratio r causes a large *resonance magnification* $Y(\nu_1)/Y_{\text{stat.}}$.

The resonance *amplitude ratio* $H\eta/Y$ is independent of r. Placing $\mathfrak{L} = 0$ in Eq. (17a),

$$H\eta/Y \simeq (\nu_Y^2/\nu_j^2) - 1 \quad \text{(resonance)} \quad (43)$$

The ratio $H\eta/Y$ is plotted vs. t for $\alpha = 2, \sqrt{2}, 1, \sqrt{1/2}, 1/2$ for the lower mode ν_1 in Fig. 6a and for the upper mode ν_2 in Fig. 6b.

The *center of oscillations*, the intersection of $O_2C_2S_2$ with OCS, Fig. 1a, is at depth

$$d = Y/\eta = H/(H\eta/Y) \quad (44)$$

below the axle in the mode ν_1 when $H\eta/Y$ is positive, and is at height d above the axle in the mode ν_2 when $H\eta/Y$ is negative. It is desirable to have small Y and large $l_w\eta$ vibrations. The former limits the slightly damped lateral tire amplitude; the latter makes the highly damped vertical amplitude of shock absorbent tire combination more pronounced. The angle η itself must remain small because of static stability reasons.

Example. The Size of the Lateral Tire Amplitude, and the Magnitude of the Rotor Unbalance Force at Which Shock-Strut Action Sets in. Selection of Blade Dampers

Consider a twin rotor helicopter with the following data: $W = 6{,}950$ lbs., $I_\eta = 31{,}800$ slugs ft.^{2}, $H = 7$ ft., $H/l_w = 0.8$, $h/H = 1.6$; $\epsilon = 0.1$, $\delta = 0.01$; $K_t = 12{,}000$ lbs. per in., $K_Y = 6{,}000$ lbs. per in., $\lambda_{t\%} = 5$ per cent, $\lambda_{Y\%} = 5$ per cent (tires only).

The following derived constants are obtained immediately:

Tire Action Only

Mass $= M = W/g = 216$ slugs $= 18$ lbs. sec.^{2} per in.

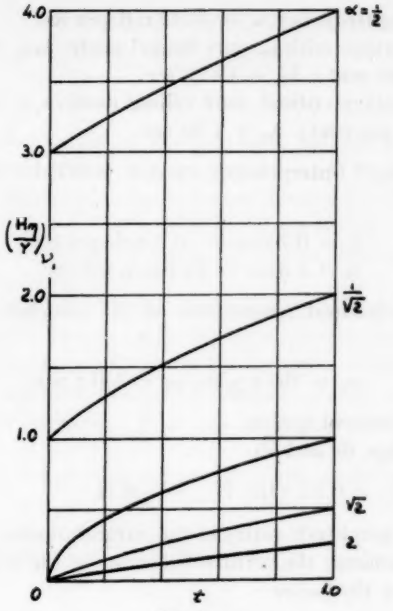

Fig. 6a.

Rolling moment of inertia, $I_\tau = 31{,}800 + 10{,}600 = 42{,}400$ slugs ft.^{2} (5)

Coefficient of coupling, $t = 10{,}600/42{,}400 = 25$ per cent (18b)

Vertical vibration frequency, $\nu_t = 25.8$ rad. per sec. (14a)

Lateral vibration frequency, $\nu_Y = 18.24$ rad. per sec. (12a)

Vertical frequency ratio, $q = 0.625$ (22b)

Lateral frequency ratio, $\alpha = 0.883$ (22c)

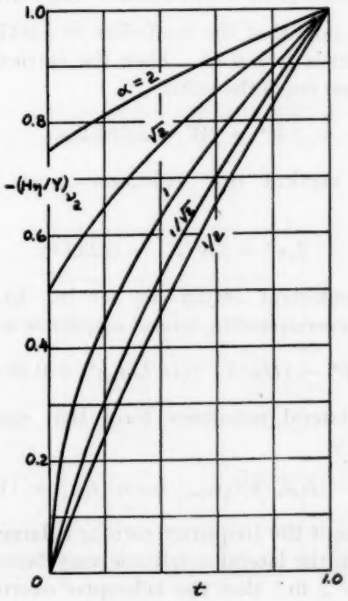

Fig. 6b.

Rolling frequency, $\nu_\eta = 16.12$ rad. per sec. (22a)

Percentage critical, pure lateral mode, $\lambda_{Y\%} =$ 5 per cent; $\lambda_Y = 1.824$/sec. (15)

Percentage critical, pure rolling mode, $\lambda_{\eta\%} =$ 3.1 per cent; $\lambda_\eta = 1.00$/sec. (22b)

By Fig. 2 (interpolating for $\alpha = 0.883$ at $t = 25$ per cent)

$$\nu_1 = 0.763\nu_Y = 13.9 \text{ rad. per sec.}$$
$$\nu_2 = 1.34\nu_Y = 24.4 \text{ rad. per sec.}$$

are the natural frequencies of the coupled system, and

$$\omega_1 = 194 \text{ r.p.m.}, \omega_2 = 340 \text{ r.p.m.} \quad (26)$$

are the critical speeds.

By Figs. 6a and 6b

$$(H\eta/Y)_{\nu_1} = 0.72, (H\eta/Y)_{\nu_2} = -0.44$$

are the amplitude ratios in the natural modes. At the first resonance the vertical deflection of the tire is magnified by the factor

$$l_w\eta(\nu_1)/l_w\eta_{\text{stat.}} = 19 \quad (42b)$$

The apparent extinction coefficient of the landing gear in the lower mode has the value

$$\lambda_a = 0.365 \times 1.824 + 0.775 \times 1.00 = 1.44/\text{sec.} \quad (29)$$

(This is somewhat worse than λ_Y.) One therefore finds that a blade damping of

$$c_b/m\rho^2 = 7.2/1.44 = 5.0/\text{sec.} \quad (27, 28)$$

is necessary to ensure stability in the absence of shock-strut action.

The Least Excitation Which Ensures Shock-Strut Action

Assume now that the coefficient of packing friction of the strut is $f = 0.40$. Then the vertical force per tire set must reach the value

$$V^* = fW = 2{,}780 \text{ lbs.} \quad (45)$$

and the vertical tire deflection must reach the value

$$l_w\eta^* = fW/K_t = 0.232 \text{ in.} \quad (46a)$$

before shock-strut action can set in. In the lower mode the corresponding lateral amplitude is

$$Y^* = (H\eta/Y)^{-1}(H/l_w)l_w\eta^* = 0.26 \text{ in.} \quad (46b)$$

and the lateral unbalance force that produces this deflection is

$$\mathfrak{L}^* = [(K_Z l_w/h)l_w\eta_{\text{stat.}}/l_w\eta(\nu_1)]l_w\eta^* = 116 \text{ lbs.} \quad (47)$$

(Note that if the frequency ratio α is large (say, $\alpha > \sqrt{2}$), then the lateral amplitude may become so large (say $Y > 2$ in.) that the helicopter overturns before shock-strut action sets in.)

The Required Blade Damping When the Shock Struts Operate

For further analysis the spring and damping constants of the shock struts must be specified. Assume these to be

$$K_s = 6{,}000 \text{ lbs. per in.}, \lambda_{s\%} = 60 \text{ per cent}$$

per pair, then for combined tire-shock-strut action

$\nu_Y = 18.24$ rad. per sec., $\alpha = 0.525$, $\nu_1 = 9.12$ rad. per sec.

$\lambda_{Y\%} = 5$ per cent, $\lambda_{\eta\%} = 19$ per cent

and therefore

$$\lambda_a = 0.14 \times 1.824 + 4.25 \times 3.64 = 15.7/\text{sec.}$$

is the apparent landing gear extinction coefficient. This yields

$$\lambda_b = 7.2/15.7 = 0.46 \text{ sec.}$$

for the extinction coefficient of the blade dampers. This is ten times smaller than the previously obtained value 5.0/sec. for the case of no shock-strut action.

Evidently an adequate knowledge of shock absorber characteristics is of primary importance in ground vibration analysis.

Comments on the Values of the Spring and Damping Constants of Helicopter Tires

R. E. Crowe and the writer have tested five pairs of high-pressure helicopter tires for spring and damping constants. The axle of the wheels supported a tray loaded with weights varying from 4,000 to 11,000 lbs. and measured the natural frequency and the decrement of the free oscillations. They found that the vertical spring constant K_t of the tires is about one or two times the static spring constant (as obtained from static deflection tests), the lateral spring constant K_Y is about one-third to one-half of K_t, and the fore-and-aft spring constant K_X (only one set of tires was tested for K_X) is about the same as K_t or somewhat higher. The tire damping constants C_X, C_Y, C_Z range from 4 to 7 per cent critical for the various tire sets. C_Y seems to be somewhat larger than C_Z. The spring constants increase with increasing tire pressure and decrease with increasing amplitude of vibration (the latter variation is pronounced). The damping constants decrease somewhat with increasing tire pressure. Highest K_t (desirable, it makes K_t/K_s large), K_t/K_Y (undesirable, it makes α large), and C_X, C_Y, C_Z (very desirable) were found for channel tread tires. The above numerical values refer to tires bouncing on steel. Using wood as foundation little change was noted, but on dirt K_t (and this alone) was invariably higher.

Combined Tire-Shock-Strut Action

When the vertical vibratory force $V \cos \Omega t$ acting on the landing gear is sufficiently large, then the condi-

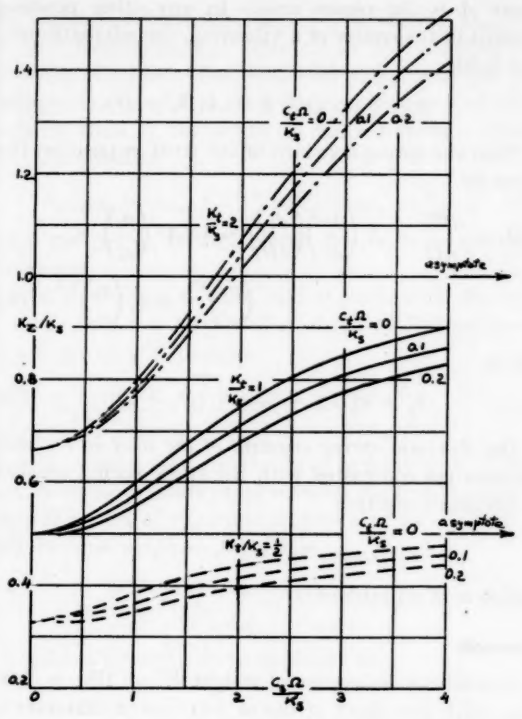

FIG. 7a.

tion $V > V^* = fW$ necessary for shock-strut action, Eqs. (45) and (61c), is satisfied, and the vertical spring and damping "constants" K_Z and C_Z of the landing gear are expressions in the strut constants K_s, C_s, in the tire constants K_t, C_t and in the frequency Ω. The purpose of this section is to establish these relations.

Roughly speaking, oil and air in the strut are subject to the same displacement; the same holds true for the spring action and the damping action of the tires. The two systems are excited by the same vertical force. Correspondingly, by the well-known electrical analogy method, it can be said that the strut impedance $K_s + i\Omega C_s$ is connected in parallel with the tire impedance $K_t + i\Omega C_t$. Jointly they yield a resultant landing gear impedance of

$$K_Z + i\Omega C_Z = [1/(K_t + i\Omega C_t) + 1/(K_s + i\Omega C_s)]^{-1} \quad (48)$$

Thus it is found that

$$K_Z = \frac{K_t K_s(K_t + K_s) + (K_s C_t^2 + K_t C_s^2)\Omega^2}{(K_t + K_s)^2 + (C_t + C_s)^2\Omega^2} \quad (49a)$$

$$C_Z = \frac{K_s^2 C_t + K_t^2 C_s + C_s C_t(C_s + C_t)\Omega^2}{(K_t + K_s)^2 + (C_t + C_s)^2\Omega^2} \quad (49b)$$

are the spring and damping constants of the landing gear.

If the struts jam, then $K_s = \infty$ and, therefore, $K_Z = K_t$, $C_Z = C_t$. For very weakly damped struts

$$K_t^2 \text{ and } K_s^2 >> C_s^2\Omega^2 >> C_t^2\Omega^2$$

are true. They lead to the familiar relations

$$K_Z \sim [(1/K_t) + (1/K_s)]^{-1} \quad (50a)$$

$$C_Z \sim C_s K_t^2/(K_t + K_s)^2 \quad (50b)$$

Thus, spring action of tire and very weakly damped strut is that of two springs K_t and K_s connected in tandem; damping action is that of damper C_s, reduced by the factor $K_t^2/(K_t + K_s)^2$. *In order to produce large strut damping it is necessary to have a large value for the ratio* K_t/K_s.

In Figs. 7a and 7b the ratios K_Z/K_s and $C_Z\Omega/2K_Z$ are plotted. The curves in Fig. 7a show that the landing gear spring constant varies between $[(1/K_t) + (1/K_s)]^{-1}$ for very small strut damping and K_t for very large strut damping. ($C_t\Omega$ can always be considered as small.)

For $C_t\Omega = 0$ the numerator $C_Z\Omega$ of the ratio $C_Z\Omega/2K_Z$ reaches a peak

$$\{C_Z\Omega\}_{max.} = {}^1/_2(K_t/K_s)[(1/K_t) + (1/K_s)]^{-1} \quad (51a)$$

at

$$C_s\Omega = K_s + K_t \quad (51b)$$

and then sinks to $C_Z\Omega = 0$ as $C_s\Omega \to \infty$. For $C_t\Omega =$ small $\neq 0$, the curve $C_Z\Omega$ is similar, except that now $C_Z\Omega \to C_t\Omega$ as $C_s\Omega \to \infty$.

For $\Omega = \nu_Z$ the ratio $C_Z\Omega/2K_Z$ represents the fraction of critical damping that is available in the vertical mode. $C_Z\Omega/2K_Z$ reaches its greatest values in the range $C_s\Omega/K_s = 1$ to 3. For conventional landing gears this rarely exceeds 35 per cent. Fig. 7b clearly indicates the importance of having a large K_t/K_s ratio, or else, of having a very large value for the vertical tire damping. If $C_s\Omega$ becomes excessive, then the shock struts lock and the available landing gear damping is that of the tires alone (asymptotes, Fig. 7b).

Example

Determine the combined tire-strut spring constant K_Z and damping constant C_Z of the helicopter of the

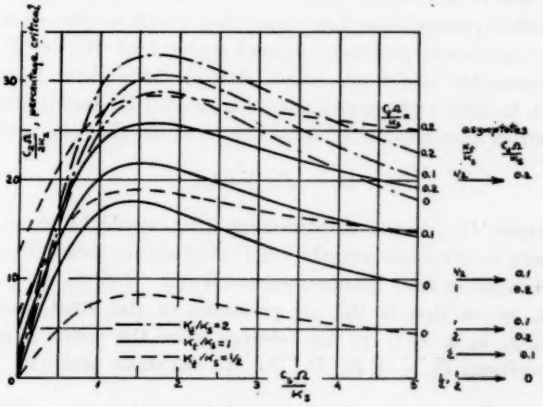

FIG. 7b.

previous section, at the lower natural frequency ν_1. Given: K_s = 6,000 lbs. per in., $\lambda_{s\%}$ = 60 per cent. (Note that ν_s = 18.2 rad. per sec., and $C_s\nu_s/K_s$ = 1.2.)

As first approximation take $\Omega = 0$. Then from Fig. 7a, $K_Z = 0.666K_s$ = 4,000 lbs. per in. Therefore α = 0.51, and by Fig. 2a, by interpolation, $\nu_1 = 0.49\nu_Y$ = 8.95 rad. per sec. (first approximation).

In second approximation take $\Omega = \nu_{1,\,\text{Approx.}}$. Then

$$C_s\Omega/K_s = 2(\lambda_{s\%}/100)(\nu_1/\nu_s) = 1.2 \times 0.49 = 0.59 \quad (52a)$$

$$C_t\Omega/K_s = 2(\lambda_{t\%}/100)(K_t/K_s)(\nu_1/\nu_t) = 0.10 \times 2 \times 8.95/25.8 = 0.07 \quad (52b)$$

From Fig. 7a the corresponding vertical spring constant is $K_Z = 0.71K_s$ = 4,240 lbs. per in. Therefore ν_Z = 15.32 rad. per sec., ν_η = 9.59 rad. per sec., α = 0.525, and, by Fig. 2a, $\nu_1 = 0.50\nu_Y$ = 9.12 rad. per sec. (second approximation). From Fig. 7b one now finds, for the curve K_t/K_s = 2, $C_t\nu_1/K_s$ = 0.07, at abscissa $C_s\nu_1/K_s$ = 1.2 × 0.50 = 0.60 that $C_Z\nu_1/2K_Z \sim$ 18 per cent (referred to the ν_1 mode). Consequently,

$$\lambda_{\eta\%} = 100\,(C_Z\nu_1/2K_Z)(\nu_\eta/\nu_1) = 18 \times 9.59/9.12 = 19 \text{ per cent} \quad (52c)$$

is the percentage critical of the tire strut combination in the rolling mode, using the K_Z and the C_Z values of the ν_1 mode. This is the quantity that enters λ_a of Eq. (28) (see the example of the preceding section).

Constants of the Shock Absorber

The shock absorber serves a dual role in ground vibrations. It acts both as a spring and as a damper. Thus, both the spring constant and the damping constant of the shock absorber are of great interest. There is, in addition, a third constant, no less important than the other two, which must be considered. This is the coefficient of packing friction. Evidently, shock absorber action can start only when packing friction has already been overcome.

Air-Spring Action

Let D_s denote the *static displacement* of the shock absorber piston from fully extended position ($D_0 = 0$) to the static position assumed under load W_1, let D_t denote the *total displacement* (stroke) of the piston from D_0 to fully compressed position, and let D_v denote the *virtual displacement of the piston*—i.e., the displacement

$$D_v = D_t + D_{\text{res.}}$$

where $D_{\text{res.}}$ is the displacement that would be necessary to eliminate also the small residual air pocket that remains in fully compressed condition. Let p_0, p_s, p_t, $p_v = \infty$ denote the air pressures of the strut, and v_0, v_s, v_t, $v_v = 0$ the air volumes when the piston is in positions $D_0 = 0$, D_s, D_t, D_v. In the static position

$$p_s = W_1/A,\ v = A(D_v - D_s) \quad (53)$$

where A is the piston area. In any other position, reached in the course of a vibration, the adiabatic relation holds

$$p = p_s(v_s/v)^{1.4},\ v = A(D_v - D) \quad (54)$$

Then the spring constant of the strut in position D is given by

$$k(D) = \frac{dW_1}{dD} = A\left(\frac{dp}{dv}\right)\left(\frac{dv}{dD}\right) = 1.4A^2\left(\frac{p_s}{v_s}\right) \times \left(\frac{v_s}{v}\right)^{2.4} = k_s\left(\frac{v_s}{v}\right)^{2.4} \quad (55)$$

where

$$k_s = k(D_s) = 1.4W_1/(D_v - D_s) \quad (56)$$

is the *dynamic spring constant of the strut in the static position* (as contrasted with the static spring constant in the static position

$$k_{s,\,\text{stat.}} = W_1/(D_v - D_s) \quad (57)$$

which is of no interest).

Example

Consider a helicopter of weight $W = 2W_1$ = 7,000 lbs., with two shock struts of 3-in. piston diameter (A = 7.07 sq.in.), 12-in. stroke (D_t = 12 in.), 1-in. taxiing stroke (D_s = 11 in.), and a residual airpocket of 2.65 cu.in. (D_v = 12.375 in.). Then

$$k_s = 1.4 \times 3{,}500/1.375 = 3{,}560 \text{ lbs. per in.},$$
$$p_s = 3{,}500/7.07 = 495 \text{ lbs. per sq.in.}$$

and

$$p_0 = p_sv_s/v_0 = 495 \times 1.375/12.375 = 55 \text{ lbs. per sq.in.} \quad (58)$$

Here p_0 is the air pressure in the completely extended position of the strut.

The stiffness of the air spring is k_s for vibrations of small amplitudes. When the amplitudes are large, then the motion becomes asymmetric about the position D_s, because of the nonlinearity of the air spring. If the strut is just bottomed ($D_{max.} = D_t$ = 12 in.) in the course of a vibration about D_s, then the other extreme position is not $D_{min.}$ = 10 in., but rather $D_{min.}$ = 8.5 in. This can be seen from Sussholz's[4] Fig. 3b or Fig. 4. To a downward amplitude of 1 in. = $D_t - D_s$ = 0.73 ($D_v - D_s$) from position D_s there corresponds a rebounce to an upward amplitude of 1.85 ($D_v - D_s$) = 2.5 in. The increase in amplitude is associated with an increase in the period of vibrations. Instead of the value $\nu_s = \sqrt{W_1/k_s}$, which holds for infinitesimal oscillations, the frequency is now, by Sussholz's Fig. 5, 0.88 ν_s. Correspondingly, the *effective spring constant* of the air spring has the value

$$k_{\text{eff.}} = 0.88^2 \times k_s = 2{,}750 \text{ lbs. per in.}$$

for oscillations between $D_{min.} = 8.5$ in. and $D_{max.} = 12$ in. Evidently, $k_{eff.}$ *decreases as the amplitude of vibration increases*. The reason for this is that the piston spends a good deal more time in the region of small stiffness than in the region of large stiffness. (Note that the quantity

$$k_{\text{average}} = {}_{D_{min.}}\int^{D_{max.}} kdD/(D_{max.} - D_{min.}) \quad (59)$$

5,950 lbs. per in. in the present case, is of no physical significance.)

It is interesting to note that *if the load on the strut is cut in half, then the period of vibrations P is increased by a factor of* $\sqrt{2}$, because

$$\frac{P_n^2}{P_0^2} = \frac{{}^1/_2 W_1/k_{sn}}{W_1/k_{s0}} = \frac{{}^1/_2 p_{s0}/v_{s0}}{p_{sn}/v_{sn}} = \frac{1}{2}\left(\frac{p_{s0}^2}{p_{sn}^2}\right) = 2 \quad (60a)$$

Here the subscripts n and 0 refer to new and old. Likewise, *if the air pressure in the extended position is doubled, then the period of vibrations is increased by a factor of* $\sqrt{2}$, because again

$$\frac{P_n^2}{P_0^2} = \frac{W_1/k_{sn}}{W_1/k_{s0}} = \frac{p_{s0}/v_{s0}}{p_{s0}/v_{sn}} = 2 \quad (60b)$$

These facts are not always appreciated.

Damper Action

A well-designed shock absorber should be approximately critically damped. This means that for vibrations at the natural frequency $\nu_s = \sqrt{k_s g/W_1}$ of the shock strut the damping force should be about twice the spring force, $c_s \nu_s/k_s \sim 2$. Since the spring constant is a rapidly increasing function of the piston displacement D, the damping constant must be an equally rapidly increasing function of D in order to produce uniform damping throughout the stroke. A suitable choice of the taper of the metering pin permits an approximation to these conditions.

The damping constant of a shock strut can be determined, for instance, from an oscillogram that shows the relative displacement of the piston and the wheel axle in the course of a drop test. This, however, yields only a certain average for c_s because the motion is nonlinear. For small oscillations about the position D, c_s is a constant and can be calculated from the properties of the liquid, the pressure, the speed of flow, and the nature of the orifice.

Packing Friction

Shock absorber action does not set in until packing friction has been overcome. If a steady static force

$$V_1 = f_1 W_1 \quad (61a)$$

is just sufficient to overcome packing friction, then an alternating force $V_1 \cos \Omega t$ is evidently insufficient. An alternating force $V_1' \cos \Omega t$ where $V_1' > V_1$, exceeds V_1 only in part of the cycle. The higher the frequency of vibrations, the greater must be the ratio

$$V_1'/V_1 = 1 + f_2 \quad (61b)$$

before strut action can set in. A further increase of the force, from V_1' to V_1^*, may be necessary to ensure an approximately sinusoidal response. Denoting the factor of increase by $1 + f_3$,

$$V_1^* = (1 + f_3)(1 + f_2) f_1 W_1 \equiv f W_1 \quad (61c)$$

The factor f can be called the *dynamic coefficient of packing friction*. Although no estimates for f are available, it is believed that at frequencies of about 4 cycles per sec., the value

$$f \sim 0.4 \quad (62)$$

used earlier in the text is not unreasonable. An experimental determination of the coefficient f_1 has been carried out by MacLean.[5] He found that under favorable conditions $f \simeq 0.05$ to 0.07.

References

[1] Deutsch, M. L., *Ground Vibrations of Helicopters*, Journal of the Aeronautic Sciences, Vol. 5, p. 223, 1946.

[2] Coleman, R. P., *Theory of Self-Excited Mechanical Oscillations of Hinged Rotor Blades*, N.A.C.A., A.R.R. No. 3G29, 1943.

[3] Horvay, G., *Stability of Helicopters on the Ground;* in preparation.

[4] Sussholz, B., *Forced and Free Motion of a Mass on an Air-spring*, Journal of Applied Mechanics, Vol. 11, p. A-101, 1944.

[5] MacLean, J. A., *Investigation of Friction and Natural Frequency of Vibration of Shock Struts and Tires*, Bendix Report No. 666, 1945.

SUGGESTIONS FOR CONTRIBUTORS TO THE PUBLICATIONS *of the* INSTITUTE *of the* AERONAUTICAL SCIENCES

The Institute of the Aeronautical Sciences invites both members and nonmembers from any country to submit papers for publication in the JOURNAL OF THE AERONAUTICAL SCIENCES and the AERONAUTICAL ENGINEERING REVIEW. The Institute, following the practice of other societies, does not pay for contributions.

The following directions for the preparation of papers, if followed by authors, will save correspondence, avoid the return of papers for changes, minimize the work of preparation for the printer, and save the expense due to the charges made for "author's corrections."

MANUSCRIPTS: Papers must be written in English, in original typewriting on one side only of white paper sheets, consecutively numbered and be double or triple spaced with wide margins. Manuscripts should be prepared with great care so that they will be typographically accurate. Paragraphing should be given special attention. Papers should be written in the third person, reference to the writer being made as "the author." Avoid the use of the words "I," "we," and "you." Blueprint copies of papers are unacceptable as it is impossible to mark directions to the printer on them. Correcting, changing, or adding to papers after they are in type is costly. It is, therefore, imperative that papers submitted be in final form. Typographical errors may be corrected on proofs, but if authors wish to add material, they may do so at their own expense. In mailing, drawings may be rolled, but manuscripts should be sent flat. Send by first class mail (register, if you wish, for your own protection) to the Editorial Office, Institute of the Aeronautical Sciences, 2 East 64th Street, New York 21, N. Y. All manuscripts will be examined by the Editorial Committee and by the Editor. Authors will be advised as promptly as possible whether the paper is acceptable for publication.

TITLES: The title of the paper should be brief. The name and initials of the author should be written as he prefers. The use of the full name of an author is advocated because of the frequent duplication of initials and surnames which sometimes makes it difficult to establish the identity of the author. This is particularly important for large annual indexing and abstracting services. All titles and degrees or honors are omitted. The name of the organization with which the author is associated should be placed after his name on a separate line. The date on which the paper is received will be inserted by the Editor.

SUMMARIES OR ABSTRACTS: An abstract to be printed at the beginning should accompany each article. It should be adequate as an *index* and as a *summary*. It should contain a statement of major conclusions reached, since summaries in many cases constitute the only source of information used in compiling scientific reference indexes. Abstracts printed in other journals, especially foreign, in most cases, consist of summaries from printed papers. The summary should explain as adequately as possible the major conclusions to a nonspecialist in the subject. The summary should contain from 100 to 300 words, depending on the length of the paper.

SUBHEADINGS: Subheadings should be inserted by the author at frequent intervals. The work of editorial preparation will be simplified by the author providing many subheadings. Because of the breaking of columns and the insertion of illustrations, some of the subheadings may have to be omitted.

SHORTENING OF PAPERS: Some papers, at the end, fill in only a portion of a page. This leaves much wasted blank space as succeeding articles are started at the top of a page. Authors should indicate by notation on the left-hand side of the page what matter may be omitted when "runovers" occur. This request is important as the Journal cannot afford in the future, as it has in its earlier issues, to have blank half pages or more at the end of papers.

MATTER USUALLY DELETED: Acknowledgments of assistance in preparation of paper, except by collaborators. Photographs or illustrations of little technical interest and not showing advances in general practice. Too detailed tabular matter (general results of such tables may be included in the text). Lengthy descriptions of materials or processes or of preliminary experiments or theories that preceded final results; salient features only are of interest.

REFERENCES AND FOOTNOTES: References should appear as footnotes only, numbered consecutively, grouped together at the end of the manuscript. The arrangement should be as follows: (for books)—[1] Durand, W. F., *Aerodynamic Theory*, 1st Ed., Vol. 1, p. 23; Julius Springer, Berlin, 1934. (For magazines)—

[1] Englund, C. R., Crawford, A. B., and Mumford, W. W., *Some Results of a Study of Ultra-Short-Wave Transmission Phenomenon*, Proc. I. R. E., Vol. 20, No. 12, pp. 481 and 482, March, 1933. Please give author, title, edition, volume, page, publisher, and date of publication as indicated. Omission of one required fact causes much extra editorial work and possible inaccuracies. All references should be grouped at the end of the article.

ILLUSTRATIONS: Illustrations should accompany manuscripts and each should always be referred to in the text, preferably by number. Drawings or graphs should not be larger than 12 × 16 inches, and must be made with jet black India Ink on white paper or tracing cloth, the latter being preferred. *Do not use typewriter for lettering.* The smallest lettering on 8 × 10 inch figures should be no less than 1/4 inch high. Cross-section paper (white with black lines) may be used, but should not have more than 4 lines per inch. If finer ruled paper is used, the major division lines should be drawn in with black ink, omitting the finer divisions. In the case of finely ruled paper, only blue-lined paper can be accepted. *Tracing paper and blueprints* are not acceptable. Lettering and all markings must be large enough to be readable after reduction. Mail rolled or flat, never fold. Drawings that cannot be reproduced (including pencil drawings) will be returned to the author for redrawing, thus delaying publication of the paper. Photographs should be distinct and show clear black and white contrasts. They must be on glossy white paper. Avoid round and oval photographs.

CAPTIONS AND LEGENDS: Legends or captions must accompany each drawing or photograph submitted. If written on the drawing or photograph, they should be placed below and well outside the part to be reproduced. It is better to place them on separate sheets of paper pasted to the back of the drawings or photographs. Each table should have a caption such as Table 1, Table 2, Table 3, etc. Captions should be complete in themselves so as to make the data intelligible to the reader without reference to the text. A duplicate list of captions for figures should be included as the last page of the manuscript. Use "Fig. 1" (not Figure 1), Figs. 3 and 4, etc., in both the text and the numbering of illustrations. In the text, "Eq. (1)," or "Eqs. (1) and (2)" are preferable to "Equation (1)." In captions and legends, except for "Fig." and "Eq.," and in table headings, write all words in full; do not abbreviate. Avoid placing explanatory written matter in the drawings; it should be in the text.

MATHEMATICAL WORK: Only the simplest formulas should be typewritten; all others should be carefully written in pen and ink, the writing to be large enough so that ample room is provided to mark mathematical matter for the printer. A considerable space for marking should be allowed above and below all equations. All complicated equations should be repeated on separate sheets with plenty of space left for marking. The solidus should be used for simple fractions appearing within the text. Make all expressions clear to the typesetter. Greek letters used in formulas should be clearly designated by name on the margin of the manuscript. All symbols should be clearly written and carefully checked. The difference between capital and lower-case letters should be clearly distinguished and care taken to avoid confusion between zero (0) and the letter (o), between the numeral (one) and the letter (ell) and the prime (′), between alpha and a, kappa and k, u and mu, v and nu; n and eta. All subscripts and exponents should be clearly marked and dots and bars over letters or mathematical expressions should be avoided. Avoid complicated exponents and subscripts. When it is necessary to repeat a complicated expression, it should be represented by some convenient symbol.

NOMENCLATURE AND ABBREVIATIONS: The National Advisory Committee for Aeronautics Nomenclature should be used jn preference to any others. Standard abbreviations should be used, and it should be noted that most abbreviations are lower case such as m.p.h., b.m.e.p., i.hp., b.hp., hp.,...etc.

INSTITUTE of the AERONAUTICAL SCIENCES

President
ARTHUR E. RAYMOND

Vice-Presidents
P. R. BASSETT
J. H. KINDELBERGER
JOHN C. LESLIE
BURDETTE S. WRIGHT

Director
S. PAUL JOHNSTON

Executive Vice-President
BENNETT H. HORCHLER

Past-Presidents
J. C. HUNSAKER
CHARLES L. LAWRANCE
DONALD W. DOUGLAS
GLENN L. MARTIN
CLARK B. MILLIKAN
T. P. WRIGHT
GEORGE W. LEWIS
JAMES H. DOOLITTLE
FRANK W. CALDWELL
HALL L. HIBBARD
HUGH L. DRYDEN
R. H. FLEET
CHARLES H. COLVIN

Assistant to the President
GEORGE R. FORMAN

Secretary
ROBERT R. DEXTER

Treasurer
C. S. JONES

Controller
JOSEPH J. MAITAN

COUNCIL

LESTER D. GARDNER, *Chairman*

E. E. ALDRIN
PETER ALTMAN
REX B. BEISEL
LAWRENCE D. BELL
GEORGE W. BRADY
W. A. M. BURDEN
CHARLES H. COLVIN
JAMES H. DOOLITTLE
WILLIAM K. EBEL
SHERMAN M. FAIRCHILD
DONALD W. FINLAY
CHARLES FROESCH
LEROY R. GRUMMAN
R. PAUL HARRINGTON
W. WALLACE KELLETT
OTTO E. KIRCHNER
JEROME LEDERER
ROBERT J. MINSHALL
EARL D. OSBORN
ELMER A. SPERRY, JR.
ERNEST G. STOUT
FRED E. WEICK

ADVISORY COMMITTEE

W. M. ALLEN
WALTER BEECH
ERNEST R. BREECH
RALPH S. DAMON
DONALD W. DOUGLAS
R. H. FLEET
JACK FRYE
ROBERT E. GROSS
R. M. HAZEN
H. MANSFIELD HORNER
J. C. HUNSAKER
CROIL HUNTER
TH. VON KÁRMÁN
I. M. LADDON
P. W. LITCHFIELD
F. W. MAGIN
ALFRED MARCHEV
GLENN L. MARTIN
THOMAS A. MORGAN
R. C. MUIR
JOHN K. NORTHROP
W. A. PATTERSON
E. T. PRICE
F. W. REICHELDERFER
LAURANCE S. ROCKEFELLER
FRED H. ROHR
T. CLAUDE RYAN
GUY W. VAUGHAN
EDWARD P. WARNER

HONORARY MEMBERS

JOHN C. ADAMS
GRIFFITH BREWER
W. A. M. BURDEN
E. U. CONDON
L. C. CRAIGIE
IRA C. EAKER
HARRY F. GUGGENHEIM
HENRY G. HOUGHTON
GEORGE C. KENNEY
CURTIS E. LE MAY
GEORGE B. PEGRAM
E. M. POWERS
J. LAURENCE PRITCHARD
ARTHUR W. RADFORD
F. W. REICHELDERFER
L. B. RICHARDSON
H. B. SALLADA
CARL SPAATZ
L. C. STEVENS
NATHAN F. TWINING

HONORARY FELLOWS

H. H. ARNOLD
DONALD W. DOUGLAS
HUGH L. DRYDEN
W. F. DURAND
SIR RICHARD FAIREY
SIR ROY FEDDEN
J. C. HUNSAKER
SIR MELVILL JONES
GEORGE W. LEWIS
GLENN L. MARTIN
GEORGE J. MEAD
SIR FREDERICK HANDLEY PAGE
D. R. PYE
IGOR I. SIKORSKY
G. I. TAYLOR
TH. VON KÁRMÁN
EDWARD P. WARNER
ORVILLE WRIGHT
T. P. WRIGHT

BENEFACTORS

E. E. ALDRIN
HART O. BERG (Deceased)
W. A. M. BURDEN
E. L. CORD
DONALD W. DOUGLAS
SHERMAN M. FAIRCHILD
SIR RICHARD FAIREY
R. H. FLEET
FLORENCE GUGGENHEIM (Deceased)
C. D. HANSCOM
JOHN P. V. HEINMULLER
ALEXANDER KLEMIN
PAUL KOLLSMAN
BELLA C. LANDAUER
WILLIAM LANDAUER
GROVER LOENING
EDMUND C. LYNCH (Deceased)
F. W. MAGIN
GLENN L. MARTIN
GEORGE J. MEAD
S. A. REED (Deceased)
LAURANCE S. ROCKEFELLER
EDWARD P. WARNER

AMERICAN FELLOWS

JOHN D. ACKERMAN
E. E. ALDRIN
HARRY G. ARMSTRONG
KARL ARNSTEIN
J. L. ATWOOD
PAUL S. BAKER
RALPH S. BARNABY
P. R. BASSETT
WELLWOOD E. BEALL
REX B. BEISEL
G. M. BELLANCA
DON R. BERLIN
HENRY A. BERLINER
WILLIAM BOLLAY
B. C. BOULTON
GEORGE W. BRADY
LYMAN J. BRIGGS
W. G. BROMBACHER
CHARLES P. BURGESS
FRANK W. CALDWELL
KENNETH CAMPBELL
CHARLES H. CHATFIELD
ALLAN CHILTON
V. E. CLARK
FRANKLIN R. COLLBOHM
CHARLES H. COLVIN
KARL T. COMPTON
JOHN W. CROWLEY, JR.
RALPH S. DAMON
LUIS DE FLOREZ
SMITH J. DE FRANCE
J. P. DEN HARTOG
WALTER S. DIEHL
JAMES H. DOOLITTLE
C. S. DRAPER
IVAN H. DRIGGS
WILLIAM K. EBEL
C. L. EGTVEDT
FREDERIC FLADER
CHARLES FROESCH
JACK FRYE
GARLAND FULTON
LESTER D. GARDNER
RICHARD C. GAZLEY
MICHAEL E. GLUHAREFF
MELVIN N. GOUGH
LEROY R. GRUMMAN
HAROLD R. HARRIS
R. M. HAZEN
ALBERT F. HEGENBERGER
EDWARD H. HEINEMANN
S. D. HERON
HALL L. HIBBARD
L. S. HOBBS
PAUL E. HOVGAARD
WILLIAM HOVGAARD
ROBERT INSLEY
EASTMAN N. JACOBS
CLARENCE L. JOHNSON
ALEXANDER KARTVELI
PAUL H. KEMMER
J. H. KINDELBERGER
OTTO E. KIRCHNER
ARTHUR L. KLEIN
ALEXANDER KLEMIN
W. B. KLEMPERER
PAUL KOLLSMAN
OTTO C. KOPPEN
B. V. KORVIN-KROUKOVSKY
S. M. KRAUS
I. M. LADDON
E. S. LAND
CHARLES L. LAWRANCE
JOHN G. LEE
JOHN C. LESLIE
CHARLES A. LINDBERGH
WILLIAM LITTLEWOOD
GROVER LOENING
W. RANDOLPH LOVELACE, II
EUGENE E. LUNDQUIST
R. D. MACCART
JOHN R. MARKHAM
ERLE MARTIN
WM. H. MCAVOY
C. J. MCCARTHY
CLARK B. MILLIKAN
ROBERT J. MINSHALL
JOSEPH S. NEWELL
ALFRED S. NILES
JOHN K. NORTHROP
ARTHUR NUTT
SHATSWELL OBER
ROBERT E. OSBORN
W. BAILEY OSWALD
GEORGE A. PAGE, JR.
F. W. PAWLOWSKI
F. W. PENNOYER, JR.
A. A. PRIESTER
ARTHUR E. RAYMOND
F. W. REICHELDERFER
ELLIOTT G. REID
H. J. E. REID
H. C. RICHARDSON
LEONARD E. ROOT
C. E. ROSENDAHL
WILLIAM T. SCHWENDLER
JAMES M. SHOEMAKER
MAC SHORT
IGOR ALEXIS SIKORSKY
SELDEN B. SPANGLER
ELMER A. SPERRY, JR.
JOHN STACK
WILLIAM B. STOUT
HARRY A. SUTTON
C. FAYETTE TAYLOR
EDWARD S. TAYLOR
PHILIP B. TAYLOR
TH. THEODORSEN
T. E. TILLINGHAST
S. TIMOSHENKO
L. B. TUCKERMAN
RALPH H. UPSON
J. G. VINCENT
RICHARD VON MISES
FRANK L. WATTENDORF
P. V. H. WEEMS
FRED E. WEICK
R. D. WEYERBACHER
JOHN B. WHEATLEY
ANDREW V. WILLGOOS
DONALD H. WOOD
ROBERT J. WOODS
JOHN E. YOUNGER
ALBERT F. ZAHM
STEPHEN J. ZAND

An Appreciation

TO CORPORATE MEMBERS OF THE INSTITUTE OF THE AERONAUTICAL SCIENCES

Listed below are the leading aeronautical and industrial companies that make possible the publication of the *Journal of the Aeronautical Sciences*.

They enable the Institute to publish scientific and technical papers in the *Journal* and to devote its pages exclusively to editorial material.

Dues from individual members which would normally be used to publish this scientific and engineering monthly are thus released for additional services to the profession and industry.

The *Aeronautical Engineering Review* and the *Aeronautical Engineering Catalog*, together with the *Journal*, provide a comprehensive technical information service for the benefit of the aircraft and related industries.

ACADEMY OF AERONAUTICS, INC.
CASEY JONES SCHOOL OF AERONAUTICS
AERO INSURANCE UNDERWRITERS
AEROJET ENGINEERING CORPORATION
AERONCA AIRCRAFT CORPORATION
AEROQUIP CORPORATION
AGAWAM AIRCRAFT PRODUCTS, INC.
AIRBORNE INSTRUMENTS LABORATORY, INC.
AIRCHOX COMPANY DIVISION, JOYCE AVIATION, INC.
AIRCRAFT RADIO CORPORATION
AIREON MANUFACTURING CORPORATION
AIRESEARCH MANUFACTURING COMPANY
AIRESEARCH MANUFACTURING COMPANY OF ARIZONA, INC.
AIREX MANUFACTURING COMPANY, INC.
ALLIS-CHALMERS MANUFACTURING COMPANY
ALLISON DIVISION, GENERAL MOTORS CORPORATION
ALUMINUM COMPANY OF AMERICA
AMERICAN AIRLINES SYSTEM
AMERICAN OVERSEAS AIRLINES, INC.
AMERICAN BOSCH CORPORATION
AMERICAN PHENOLIC CORPORATION
ASSOCIATED AVIATION UNDERWRITERS
ASSOCIATED FOUNDRIES & MANUFACTURERS, INC.
ATLAS SUPPLY COMPANY
BAKER STEEL & TUBE COMPANY
BEECH AIRCRAFT CORPORATION
BELL AIRCRAFT CORPORATION
BENDIX AVIATION CORPORATION
BENDIX PRODUCTS DIVISION
BENDIX RADIO CORPORATION
ECLIPSE-PIONEER DIVISION
EXPORT DIVISION
FRIEZ INSTRUMENT DIVISION
PACIFIC DIVISION
SCINTILLA MAGNETO COMPANY
THE BG CORPORATION
BOEING AIRCRAFT COMPANY
BOEING SCHOOL OF AERONAUTICS
BREEZE CORPORATIONS, INC.
ESSEX TOOL & DIE COMPANY
FEDERAL LABORATORIES, INC.
CAL-AERO TECHNICAL INSTITUTE, A DIVISION OF GRAND CENTRAL AIRPORT COMPANY
CARRIER CORPORATION
CESSNA AIRCRAFT COMPANY
CHANDLER-EVANS CORPORATION
CHASE NATIONAL BANK OF THE CITY OF NEW YORK
THE CLEVELAND GRAPHITE BRONZE COMPANY
THE CLEVELAND PNEUMATIC TOOL COMPANY
AUTOMOTIVE-AIRCRAFT DIVISION
CLIFFORD MANUFACTURING COMPANY
CONSOLIDATED VULTEE AIRCRAFT CORPORATION
NASHVILLE DIVISION
STINSON AIRCRAFT DIVISION
CONTINENTAL MOTORS CORPORATION
COX AND STEVENS AIRCRAFT CORPORATION
CULVER AIRCRAFT CORPORATION
CURTISS-WRIGHT CORPORATION
AIRPLANE DIVISION
DEVELOPMENT DIVISION
PROPELLER DIVISION
WRIGHT AERONAUTICAL CORPORATION
DOAK AIRCRAFT COMPANY, INC.
DOUGLAS AIRCRAFT COMPANY, INC.
EL SEGUNDO PLANT
LONG BEACH PLANT
THE DOW CHEMICAL COMPANY
DZUS FASTENER COMPANY, INC.
EASTERN AIR LINES, INC.
EATON MANUFACTURING COMPANY
THOMAS A. EDISON, INCORPORATED, INSTRUMENT DIVISION
EDO AIRCRAFT CORPORATION
THE ELECTRIC AUTO-LITE COMPANY
ELECTROL INCORPORATED
ENGINEERING AND RESEARCH CORPORATION
ETHYL CORPORATION
THE FAFNIR BEARING COMPANY
FAIRCHILD CAMERA & INSTRUMENT CORPORATION
FAIRCHILD AERIAL SURVEYS, INC.
FAIRCHILD ENGINE AND AIRPLANE CORPORATION
DURAMOLD DIVISION
FAIRCHILD AIRCRAFT DIVISION
RANGER AIRCRAFT ENGINES DIVISION
FEDERAL TELEPHONE AND RADIO CORPORATION
FLETCHER AVIATION CORPORATION
G & A AIRCRAFT, INC.
FIRESTONE AIRCRAFT COMPANY
GENERAL AVIATION EQUIPMENT COMPANY, INC.
GENERAL ELECTRIC COMPANY
GENERAL INSTRUMENT CORPORATION
GENERAL MOTORS CORPORATION
AC SPARK PLUG DIVISION
AEROPRODUCTS DIVISION
BUICK MOTOR DIVISION
CADILLAC MOTOR CAR DIVISION
CHEVROLET MOTOR DIVISION
DELCO PRODUCTS DIVISION
DELCO-REMY DIVISION
EASTERN AIRCRAFT DIVISION
FISHER BODY DIVISION
FRIGIDAIRE DIVISION
HARRISON RADIATOR DIVISION
RESEARCH LABORATORIES DIVISION
ROCHESTER PRODUCTS DIVISION
THE B. F. GOODRICH COMPANY
THE GOODYEAR TIRE & RUBBER COMPANY
THE GRAY MANUFACTURING COMPANY
GRUMMAN AIRCRAFT ENGINEERING CORPORATION
W & L. E. GURLEY
HANNA ENGINEERING WORKS
HASKELITE MANUFACTURING CORPORATION
HAWAIIAN AIRLINES LIMITED
THE HILLIARD CORPORATION
THE INTERNATIONAL NICKEL COMPANY
IRVING AIR CHUTE COMPANY, INC.
JACK & HEINTZ, INC.
JOHNS-MANVILLE SALES CORPORATION
KAISER FLEETWINGS, INC.
KELLETT AIRCRAFT CORPORATION
KENYON INSTRUMENT COMPANY, INC.
WALTER KIDDE & COMPANY, INC.
KOLLSMAN INSTRUMENT DIVISION, SQUARE D COMPANY
LANGLEY CORPORATION
LAVELLE AIRCRAFT CORPORATION
LEAR INCORPORATED
LIBERTY AIRCRAFT PRODUCTS CORPORATION
LINK AVIATION DEVICES, INC.
THE LIQUIDOMETER CORPORATION
LOCKHEED AIRCRAFT CORPORATION
LONGINES-WITTNAUER WATCH COMPANY, INC.
MAGNAFLUX CORPORATION
THE MARQUETTE METAL PRODUCTS COMPANY
THE GLENN L. MARTIN COMPANY
THE W. L. MAXSON CORPORATION
WARREN McARTHUR CORPORATION
McDONNELL AIRCRAFT CORPORATION
MENASCO MANUFACTURING COMPANY
MICROMATIC HONE CORPORATION
MINNEAPOLIS-HONEYWELL REGULATOR COMPANY
MOORE DROP FORGING COMPANY
NATIONAL CITY BANK OF NEW YORK
NATIONAL CREDIT OFFICE, INC.
THE NEW YORK AIR BRAKE COMPANY
NORMA-HOFFMANN BEARINGS CORPORATION
NORTH AMERICAN AVIATION, INC.
NORTH AMERICAN AVIATION, INC., OF TEXAS
NORTHROP AIRCRAFT, INC.
NORTHWEST AIRLINES, INC.
OWENS-CORNING FIBERGLAS CORPORATION
PAN AMERICAN WORLD AIRWAYS SYSTEM
THE PARKER APPLIANCE COMPANY
PENNSYLVANIA-CENTRAL AIRLINES CORPORATION
PESCO PRODUCTS COMPANY DIVISION, BORG-WARNER CORPORATION
PHILLIPS PETROLEUM COMPANY
PIONEER PARACHUTE COMPANY, INC.
PIPER AIRCRAFT CORPORATION
THE PURE OIL COMPANY
RADIOPLANE COMPANY
REPUBLIC AVIATION CORPORATION
J. P. RIDDLE COMPANY
A. V. ROE CANADA LIMITED
JOHN A. ROEBLING'S SONS COMPANY
ROHR AIRCRAFT CORPORATION
ROOSEVELT FIELD, INC.
THE RYAN AERONAUTICAL COMPANY
SCIAKY BROTHERS
SCOTT AVIATION CORPORATION
SHELL OIL COMPANY, INC.
SIMMONDS AEROCESSORIES, INC.
SKYDYNE, INC.
SOCONY-VACUUM OIL COMPANY
SOLAR AIRCRAFT COMPANY
SPERRY GYROSCOPE COMPANY, INC.
SQUARE D COMPANY
STANDARD OIL COMPANY OF CALIFORNIA
STANDARD OIL COMPANY (INDIANA)
STANDARD OIL COMPANY OF NEW JERSEY
SWEDLOW AEROPLASTICS CORPORATION
THE TEXAS COMPANY
THOMPSON PRODUCTS, INC
TINNERMAN PRODUCTS, INC.
TITEFLEX, INC.
TRANSCONTINENTAL & WESTERN AIR, INC.
UNION CARBIDE AND CARBON CORPORATION
BAKELITE CORPORATION
HAYNES STELLITE COMPANY
LINDE AIR PRODUCTS COMPANY
NATIONAL CARBON COMPANY
UNITED AIRCRAFT CORPORATION
CHANCE VOUGHT AIRCRAFT DIVISION
HAMILTON STANDARD PROPELLERS DIVISION
PRATT & WHITNEY AIRCRAFT DIVISION
PRATT & WHITNEY AIRCRAFT CORPORATION OF MISSOURI
SIKORSKY AIRCRAFT DIVISION
UNITED AIR LINES, INC.
UNITED STATES AVIATION UNDERWRITERS, INC.
UNITED STATES RUBBER COMPANY
DOMINION RUBBER COMPANY, LTD.
THE VARIETY AIRCRAFT CORPORATION
VICKERS, INC.
VIDAL CORPORATION
THE WACO AIRCRAFT COMPANY
WARNER AIRCRAFT CORPORATION
THE WEATHERHEAD COMPANY
WESTERN AIR LINES, INC.
WESTINGHOUSE ELECTRIC CORPORATION
WESTON ELECTRICAL INSTRUMENT CORPORATION
WYMAN-GORDON COMPANY
YOUNG RADIATOR COMPANY